Geology, geochemistry, geochronology, and economic potential of the Taftan volcanic complex, southeastern Iran

by

Seyed Amir Mohammad Razavi Khosroshahi

A thesis submitted in partial fulfillment of the requirements for the degree of

Master of Science

Department of Earth and Atmospheric Sciences
University of Alberta

Abstract

The late Miocene-Quaternary Taftan volcanic complex is located above the Makran subduction zone in Sistan and Baluchestan province of southeastern Iran. The earliest volcanic eruptions at Taftan started in the late Miocene (~8 Ma) by explosive eruption of andesitic to dacitic lava on the Cretaceous to Eocene volcanic and sedimentary paleosurface ~20 km to the northwest of the current edifice. Later Plio-Pleistocene volcanism consisted of voluminous andesitic and dacitic lavas and pyroclastic flows (~3.1-0.4 Ma).

The major and trace element compositions of the Taftan volcanic rocks show calc-alkaline to high-K calc-alkaline affinity with depletions of Nb, Ta, and Ti and relative enrichment of large-ion lithophile elements (LILE) and Th and U; these are typical signatures of subduction-related arc magmas. From the late Miocene to the late Pleistocene La/Yb and Sr/Y ratios of the Taftan volcanic rocks increase, which likely reflects fractional crystallization of pyroxene and amphibole.

Electron microprobe analysis of amphibole phenocrysts from the Taftan volcanic rocks show that amphibole chemistry changed from high-Al pargasite to low-Al magnesio-amphibole from the late Miocene to the Pleistocene. Detailed modelling of amphibole chemistry indicates that the host magmas were water saturated (>5 wt.% H_2O) and underwent partial crystallization at various depths between ~20 to ~5 km in the upper crust prior to eruption.

Temperature and oxidation state estimates obtained from magnetite-ilmenite mineral pairs from andesites and amphibole phenocrysts in andesites show that they crystallized at temperature from ~1000°C to ~800°C under moderately oxidizing conditions (ΔFMQ +1.7 ± 0.3).

The presence of small porphyry and epithermal prospects such as the Kharestan Cu porphyry (6.10 ± 0.40 Ma) and Siah jangal epithermal Au deposit in the late Miocene, and several argillic to advanced argillic fumarolic alteration zones in the Taftan Plio-Pleistocene volcanic rocks suggest the potential for additional porphyry and epithermal style mineralization within the volcanic edifice at depth.

In the name of God the merciful the compassionate

Acknowledgements

I would like to express my best gratitude to my supervisor Professor Jeremy P. Richards for his support, guidance, encouragement, and very constructive criticism. Jeremy was very patient with English writing and me. Without his priceless effort and help I would never be able to finish this degree and stand at this point.

I would like to thank Dr. Ali Sholeh and Dr. Mehraj Aghazadeh for their assistance during two field seasons in 2012 and 2013 and their constructive discussions during this project. Special thanks are owed to National Iranian Copper Co (NICICo) and Mr. Esfahanipour, Engineer Taghizadeh, Engineer Khorasani, and the rest of staff members for their financial, logistic, and accommodation support during this project. Special thanks are also due to IMIDRO Company and Engineers Asgharzadeh, Shirkhani, and Fattahi for financial and logistic support and providing access to their properties throughout this project.

I offer my gratitude to Dr. Andrew Locock for microprobe analysis, and Mark Labbe and Martin Von Dollen for their valuable support for samples preparation at the University of Alberta; Mr Shakourian for sample preparation at Zarazma Laboratory in Tehran, and my best friend Dr. Rui Wang for his assistance in thin sections microscopy.

Finally, I offer my purest love and thanks to my family and specially my parents, Abdollah and Zohreh for their endless love. Without their emotional support, encouragement, and patience I never could reach to this point. Thanks for being there.

Table of Contents

List of Tables

List of Figures

1. Introduction

The Taftan volcanic complex (TVC) is located ~45 km north-northeast of Khash City in Sistan and Baluchestan province in southeastern Iran (Fig. 1). The TVC consists of several craters, the highest of which is the semi-active saddle-shaped Narkuh-Matherkuh vent with an elevation of 4050 m above sea level (28°35'56.3" N, 61°07'55.1" E). The TVC has a diameter of ~40 km and covers an area of roughly ~1300 km^2. Since 1902 to 1993, several eruptions have been reported from the volcano (Siebert and Simkin, 2002), although Shakeri et al. (2008) suggest that these events may have been molten sulfur flows related fumarolic activity rather than actual volcanic eruptions.

McCall (1997) suggested that the TVC is one of a chain volcanic centers (including Bazman in the west and Kuh-i-Sultan in the east) developed on the northern border of the Makran Arc, which extends from southeast Iran to the Chagai Hill in western Pakistan, in response to subduction of Indian Ocean lithosphere (Fig. 2).

Several previous studies have investigated the petrology, geochemistry, and tectonic evolution of the Makran Arc (e.g., Berberian et al., 1981; Biabangard and Moradian, 2008; Perello et al., 2008; Saadat and Stern, 2011), and Pang et al. (2014) included analyses of volcanic rocks from Taftan. The purpose of this study is to understand the tectonomagmatic history and economic potential of the TVC by synthesizing new and existing geochronological, geochemical, and mineral chemistry data.

A brief introduction to geological and tectonic history of Iran including the Makran Arc is first provided. Detailed geological and petrographic descriptions of the TVC are then presented based on field mapping and sampling. X-ray fluorescence (XRF) and inductively coupled plasma mass spectrometry (ICP-MS) whole rock analyses of volcanic rocks and geochronological data from $^{40}Ar/^{39}Ar$ dating of biotite and hornblende phenocrysts are reported. Magmatic oxidation state, temperature and pressure (inferred depths of magma crystallization) are also reported from electron-probe microanalysis (EPMA) of magnetite-ilmenite mineral pair and amphibole phenocrysts. Finally, by combinig new geochemical and petrographic data and field observations, a detailed genetic model for the formation of the TVC, and the relationship between magmatic and ore-forming processes is proposed.

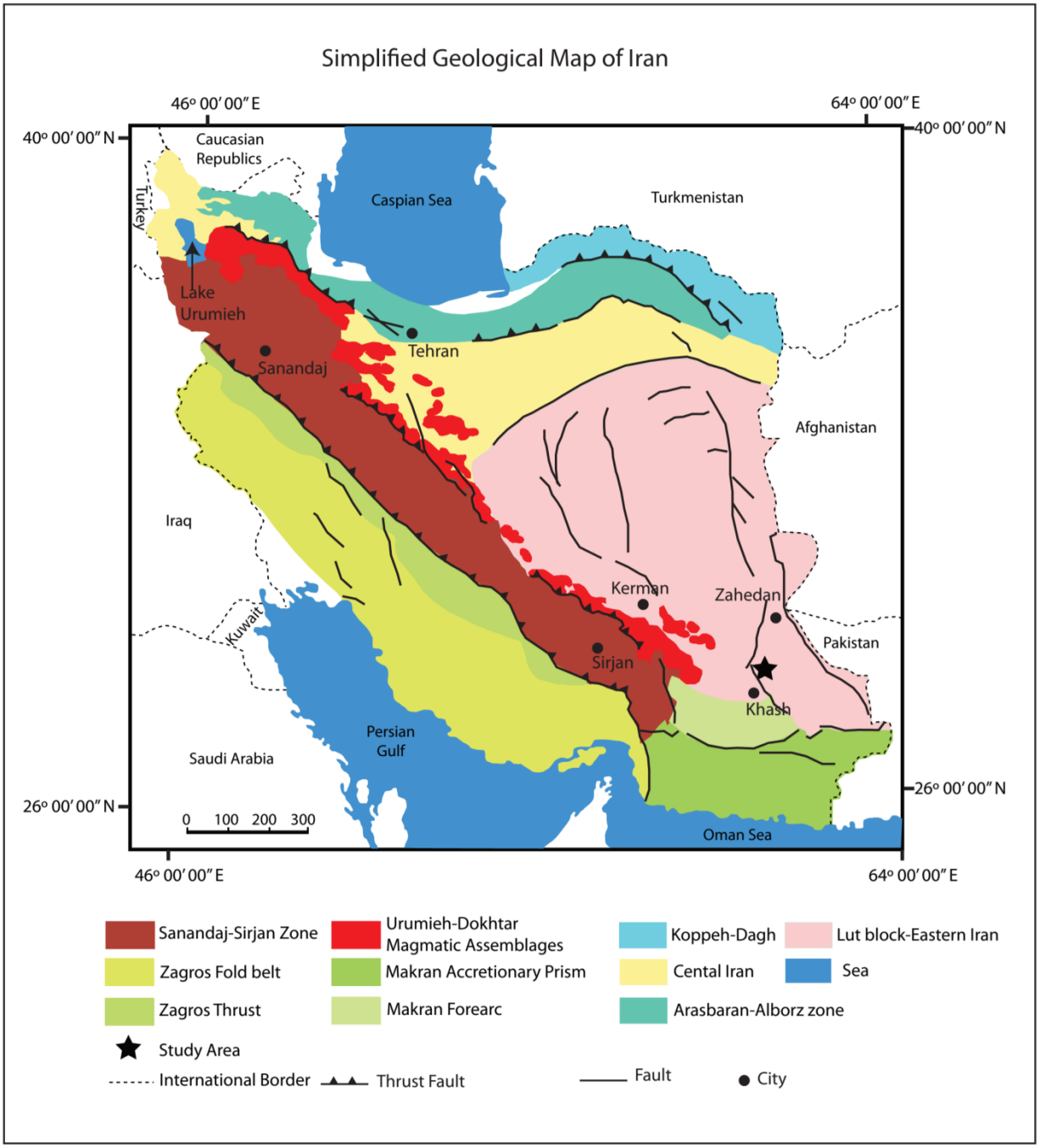

Fig. 1: Simplified geological map of Iran and different tectonic segments (modified from Nezafati, 2006).

Fig. 2: Tectonic setting of the Makran subduction zone and the location of the Neogene volcanic arc (hollow black circles). Background image from ETOPO1, http://noaa.gove/mgg/global/relief/ETOPO1/image/color_etopo1_ice_full.tif.gz.

2. Geological History of Iran

The Iranian plateau is located in the central part of the Tethyan orogenic belt, which formed by compressional deformation resulting from collision between the Afro-Arabian and Eurasian plates. The crystalline basement of central Iran formed in the Late Precambrian to Early Cambrian by metamorphism and anatexis of the Arabian–Nubian Shield (Hushmandzadeh, 1969; Stöcklin, 1974; Davoudzadeh et al., 1986).

Rifting of the Paleo-Tethys ocean began in the Late Ordovician (Stampfli, 2000). During this time, China and Indochina separated from Gondwana but the Iran Plateau was still attached to the northern margin of Gondwana (Hooper et al., 1994).

In the Early Permian, the Paleo-Tethys started oblique subduction toward the north and created several magmatic arcs along the southern margin of Eurasia, called the "Silk Road arc" (Natal'in and Şengör, 2005). Concurrently, in response to subduction of the Paleo-Tethys beneath Eurasia, the Neo-Tethys ocean was born between Gondwana and Cimmeria (Central Iran, Sanandaj-Sirjan, and Lut Block; Stampfli, 2000).The Neo-Tethys ocean basin was active during the Mesozoic (Glennie, 2000; Ghasemi and Talbot, 2006; Mazhari et al., 2009; Shafaii Moghadam et al., 2010b; Dilek et al., 2010).

By the Jurassic, the Neo-Tethys ocean reached its maximum extension and started subducting beneath Cimmeria in the north and Gondwana in the south. Simultaneously, the Paleo-Tethys ocean was consumed by collision between Cimmeria and Eurasia (Stampfli, 2000; Yeganehfar et al., 2013). During the Cretaceous, northward and southward subduction of the Neo-Tethys continued and calc-alkaline magmatism occurred across the Balkans, Turkey, Azerbaijan, and Iran.

Subduction of the Neo-Tethys Ocean continued northward beneath Central Iran from the Late Cretaceous to the Miocene, with a flare up during the Eocene to Miocene in the Urumieh-Dokhtar Magmatic Arc (Mohajjel, 2003; Omrani et al., 2008; Verdel et al., 2011).

There is no consensus on the exact time and location of Neo-Tethys closure and collision between the Afro-Arabia and Eurasia plates. A Late Cretaceous (Maastrichtian) collision is the oldest time suggested (Stöcklin, 1974; Berberian & King, 1981; Alavi, 1994; Mohajjel & Fergusson, 2000; Glennie, 2000), but many authors have proposed younger timings, such as: Eocene (Ghasemi & Talbot, 2006; Aghazadeh et al., 2011); Eocene–Oligocene (Horton et al., 2008); Oligocene (Yilmaz, 1993); Miocene (Sengör & Natal'in, 1996; Mohajjel et al., 2003; McQuarrie et al., 2003; Agard, 2005; Haschke et al., 2010); and Pliocene (Philip et al., 1989). This wide range of proposed ages may be due to the occurrence of multiple intermediate collisional events (closure of small back-arc ocean basins), and diachroneity along the belt, with collision perhaps starting in the Late Cretaceous, accelerating in the Eocene, and terminating in the late Miocene (Chiu et al., 2013; Richards, 2014). Here, we adopt a Miocene timing for final collision as suggested by the occurrence of post-collisional ultrapotassic volcanism along the length of the UMDA during the Miocene (see section 2.1.2).

Two locations for the main Neo-Tethyan suture zone have been suggested in the literature: the Main Zagros Thrust (e.g., Stöcklin, 1968; Agard et al., 2005, 2006; Paul et al., 2010; Shafaii Moghadam et al., 2010a) and between the Sanandaj-Sirjan and Urumieh-Dokhtar Magmatic Arcs (Alavi, 1994). As a result of these different proposed suture zone locations, Glennie (2000) suggested the existence of two different Neo-Tethyan ocean basins (Neo-Tethys I and Neo-Tethys II). Although the Neo-Tethys I ocean basin is recognized by many researchers (e.g., Stoneley, 1981; Alavi, 1994; Hooper et al., 1994; Mohajjel et al., 2003; Shahabpour, 2005), there is no consensus on the existence of the Neo-Tethys II ocean (e.g., Glennie, 2000; Ghasemi and Talbot, 2006; Azizi and Jahangiri, 2008; Aziz and Moinvaziri, 2009).

2.1. Zagros Orogenic Belt

The northwest–southeast-trending Zagros Orogenic Belt is a part of the Alpine-Himalayan Orogenic Belt, extending approximately two thousand kilometers across Iran. The Zagros Orogenic Belt is composed of two major NW–SE-trending parallel metamorphic-magmatic belts, the Sanandaj-Sirjan zone (SSZ) to the southwest, and the Urumieh-Dokhtar Magmatic Assemblages (UDMA) to the northeast (Fig. 1; Alavi, 1994).

2.1.1. Sanandaj-Sirjan Zone

The Sanandaj-Sirjan Zone is a narrow NW–SE-trending belt that lies between Sanandaj city in the northwest and Sirjan city in the southeast, to the immediate northeast of the parallel Zagros Fold and Thrust Belt (Fig. 1). This nearly 200 km-wide and 1500 km-long belt shows various lithologic units mainly consisting of metamorphosed and deformed rocks, plutonic-volcanic suites, and sedimentary units (Stöcklin, 1968; Berberian and King, 1981; Alavi, 1994; Mohajjel et al., 2003).

Eftekharnejad (1981) subdivided the SSZ into northern and southern segments. The northern segment is dominantly composed of Late Cretaceous deformed and metamorphosed rocks and is intruded by numerous felsic intrusive rocks (e.g., the Alvand, Borojerd, Arak, and Malayer felsic

complexes; Masoudi, 1997; Ghasemi and Talbot, 2006; Ghalamghash et al., 2009). The southern segment mainly consists of Middle to Late Triassic deformed and metamorphosed rocks.

Several authors have reported Precambrian to Early Cambrian (600–500 Ma) ages for the oldest intrusive and metamorphic units in the SSZ, which form the crystalline basement of this part of Iran (Sheikh Chupan granitoid, and Khoy metamorphic complex; e.g., Hassanzadeh et al., 2008; Azizi et al., 2011). Omrani et al. (2008, and references therein) proposed the Siah Kuh pluton as the oldest granitoid in the belt (~200 Ma). No ages younger than the Late Cretaceous have been reported from the belt (e.g., Ahmadi Khalaji et al., 2007).

In the southern part of the SSZ, magmatism started with ultramafic to mafic rocks, and includes a sequence from dunite to gabbro (the Sikhuran Complex in the east of Hajiabad; Ghasemi and Talbot, 2006). Subduction of the Neo-Tethys I beneath the southern margin of Eurasia began during the Jurassic, and magmatism changed to intermediate and felsic compositions (widespread I-type granitoids in the SSZ; Chiu et al., 2013). Berberian and Berberian (1981) noted that these igneous rocks underwent low- to intermediate grade metamorphism during the Late Jurassic to Early Cretaceous.

In the northern part of the SSZ, plutonic activity started with intrusion of Middle Jurassic granitoids (Ahmadi Khalaji, 2006) followed by Early Cretaceous to Paleocene felsic magmatism in the Borojed Complex, which intruded Triassic to Jurassic greenschist facies rocks (Ahmadi Khalaji et al, 2007). During the Late Cretaceous to Miocene, the magmatism shifted to the UDMA.

2.1.2. Urumieh – Dokhtar Magmatic Assemblages

The 1500 km-long, NW–SE-trending, Urumieh-Dokhtar Magmatic Assemblage (UDMA) lies ~100 km to the northeast of the SSZ (Fig. 1; Alavi, 2004; Verdel et al., 2011). The Neoproterozoic crystalline basement of central Iran (Central Iran Block) marks the northern border of UDMA (Jamali et al., 2010, and references therein). As a result of Neo-Tethyan oceanic crust subduction beneath Central Iran since the Late Cretaceous, a voluminous succession of calc-alkaline lava flows and related pyroclastic rocks with minor plutons was

emplaced along the UDMA, with thicknesses exceeding 3 km in some localities (Alavi, 1994).

Many authors have assumed that Tertiary magmatism along the UDMA is a continuation of Mesozoic magmatism in the SSZ as a result of a change in slab dip (e.g., Berberian and Berberian, 1981; Shahabpour, 2007; Omrani et al., 2008). In contrast, the presence of two separate subduction zones has been proposed by some authors because of the occurrence of ophiolitic fragments between these two belts (e.g., Ghasemi and Talbot, 2006; Azizi and Moinvaziri, 2009).

Magma types found in the UDMA range from calc-alkaline to potassic (shoshonitic), reflecting a transition from normal subduction to post-collisional tectonics (Hassanzadeh et al., 2002; Ghasemi and Talbot, 2006; Azizi and Moinvaziri, 2009, Ahmadian et al., 2009; Aghazadeh et al., 2010, 2011; Verdel et al., 2011). Some researchers have proposed an island arc affinity for this magmatism (e.g., Shahabpour, 2007; Ghorbani and Bezenjani 2011), whereas an Andean-like active continental margin setting is preferred by other authors (e.g., Verdel et al., 2011; Ayati et al., 2013; Yeganehfar et al., 2013).

Subduction-related magmatism ceased diachronously along the UDMA from northwest to southeast by collision between the Afro-Arabian plate and Central Iran during the Miocene, starting at ~22 Ma in the northwest and continuing to ~9–6 Ma in the southeast. This change is recorded by a change in the composition of erupted rocks in the UMDA from I-type calc-alkaline to adakite-like (Chiu et al., 2013). Late Miocene to Quaternary high-K calc-alkaline to ultrapotassic volcanic rocks were erupted widely but sparsely from NW Iran (e.g., high-K basalt in the Saray area) to SE Iran (e.g., alkali basalts in the Sistan suture zone), and are thought to reflect post-collisional tectonic processes following the diachronous collision (Pang et al., 2012; Chiu et al., 2013; Shafaii et al., 2013).

The main porphyry and epithermal deposits in the Zagros Orogenic Belt occur in the UDMA (Richards, 2003b, 2015; Aghazadeh et al., 2015). Shafiei et al. (2009) suggested that porphyry-related magmas are generated in three episodes: Eocene-Oligocene, mid-late Oligocene, and mid-late Miocene, related to late-stage subduction and collisional processes.

2.2. Makran Zone

Volcanism in SE Iran and SW Pakistan continued from the Neogene to the present day by consumption of oceanic lithosphere beneath the Makran and Chagai Arcs, respectively (Byrne and Sykes, 1992; Siddiqui et al., 2007). The present-day lateral transition (~57° E, east of Strait of Hormoz; Fig. 2) from continent-continent collision in the Zagros Orogenic Belt to subduction in the Makran zone is marked by a gravity contrast between the Zagros Orogen (negative anomaly) and the Makran Zone (positive anomaly; Ravaut et al., 1997).

The east–west-trending Makran Zone is a convergent margin, extending approximately 800 km from the Strait of Hormoz in Iran toward Karachi harbour in Pakistan (Fig. 2; Aubourg et al., 2004). To the east, the Makran Zone is separated from the Indian plate by the dextral strike slip Ornach Nal-Chaman fault (Kukowski et al., 2000; Fig. 2). The Ornach Nal-Chaman fault was first activated in the late Oligocene to early Miocene and continues to be active today (Wellman, 1966; Lawrence et al., 1992). The western border of the Makran Zone is marked by a nearly 30 km-wide zone of NNE–SSW-trending sinistral strike-slip faults, including the Zendan, Minab, and Palami faults (Fig. 2; Regard et al., 2004; Bayer et al., 2006).

Whitmarsh (1979) suggested that subduction beneath the Makran Zone has been active since the Mesozoic, whereas Mountain and Prell (1990) suggested a Cenozoic age for the onset of subduction. However, the majority of researchers consider that subduction below the Makran Zone has been active since the Late Cretaceous and continues to the present time (Farhoudi and Karig, 1977; McCall, 2002; Bayer et al., 2006; Musson, 2009).

Based on the interpretation of seismic data, Bayrne and Sykes (1992) suggested different thicknesses of accreted subaerial and submarine sediments in the eastern and western parts of the Makran Zone. They concluded that the angle of subduction in the eastern Makran is slightly less than in the western Makran due to subduction of different plates (oceanic lithosphere of the Afro-Arabia plate in the west, and the Ormara oceanic micro plate in the east).

Western Makran is quite aseismic compared to eastern Makran (Byrne and Sykes, 1992), and Bayer et al. (2006) suggested that this might be attributed to subduction of voluminous ‘unconsolidated and water-saturated’ sediments below the western part of the belt.

The convergence rate for the Makran zone has been calculated to be 40 mm/year based on

space geodesy models (DeMets et al., 1994). More recent GPS measurements indicate convergence rates of 25 mm/year and 30 mm/year across the western and eastern Makran, respectively (Ellouz-Zimmermann et al., 2007b; Grando and McClay, 2007). This convergence rate is relatively low comapred to other active subduction zones (e.g., the Japan-Kuril arc is converging at a rate of ~10 cm/year; Sdrolias and Muller, 2006). As a result of the extremely low seismicity and convergence rate along the Makran zone, especially the western segment, McCall (2002) suggested that subduction has almost ceased.

The Makran Zone is tectonically subdivided into northern and southern basins (Fig. 1; Arshadi and Förster, 1983; Shahabpour, 2010). The northern part is characterized as a forearc basin by the occurrence of several depressions where the large alluvial plains of Jaz Murian and Mashkhel are located (Fig. 2; Falcon, 1974). The southern part marks the base of the continental slope where shelf sediments including flysch to neritic and molassic sediments have been deposited, and is known as the Makran Accretionary Prism (Farhoudi and Karig, 1977; Arshadi and Förster, 1983; Fig. 2).

To the north of the Jaz Murian depression, Cenozoic volcanoplutonic rocks are mainly andesitic in composition and form the volcanic arc of the Makran subduction zone, which overlies Paleozoic metamorphosed sedimentary basement (Falcon, 1974; Farhoudi and Karig, 1977). The volcanic centers include Bazman and Taftan in Iran (located approximately 400 km inland from the coast), and Kuh-i-Sultan in the Chagai Arc of Pakistan (~600 km from the coast). The greater distance from the coast in the east is thought to be due to the fact that subduction in the eastern Makran is occurring at a shallower angle than in the west (Kakowski et al., 2000).

Pang et al. (2014) have summarized the tectonic and geochemical evolution of the western Makran volcanic arc based on major and trace elements, Sr-Nd isotopes, and U-Pb dating. They suggested that arc magmatism in the Makran likely started in the early Miocene (19.0 ± 0.2 Ma; Mirabad pluton) and continued to the late Pleistocene (0.84 ± 0.06 Ma; Taftan andesitic rocks). The Taftan volcanic rocks have $^{143}Nd/^{144}Nd$ and $^{87}Sr/^{86}Sr$ values, ranging from -4.4 to -3.0 (average = -3.4 ± 0.5) and from 0.704359 to 0.706760 (average = 0.70612 ± 0.00088) respectively (Pang et al., 2014). According to these result and trace element geochemistry, Pang et al. (2014) proposed that magmas in the Makran arc were derived from the mantle, and have evolved through a combination of crustal assimilation and fractional crystallization processes.

Several small porphyry Cu-Au deposits around Kuh-i-Sultan (Lake Resource NL, 2014) as well as giant Reko diq and Saindak Cu-Au porphyry deposits (Sillitoe and Khan, 1977; Sillitoe, 1979; Perello et al., 2008) have been reported in the eastern Makran. In contrast, known mineralization in the western Makran is limited to small deposits such as the Chahnali low-sulfidation epithermal Au deposit to the north of Bazman (Sholeh et al., in prep.), the Kharestan porphyry Cu deposit in the northwestern part of the Taftan Volcanic Complex (see the section 3.2.1), and some scattered alteration zones around the Taftan volcano (Richards, 2014).

3. Geology of the Taftan volcanic complex

3.1. Volcanic sequence

The current Taftan edifice (Figs. 3 and 4) formed during the Neogene to Quaternary, and overlies Late Cretaceous to Eocene volcanic and sedimentary rocks. The sedimentary units include flysch type deposits and fossiliferous limestones (mostly Nummulites and Alveolinides) of Eocene age. The underlying Late Cretaceous volcanic sequences consist of ultramafic to mafic units of colored mélange (ophiolite) of the Makran Acceretionary Prism.

Volcanism at Taftan began in the late Miocene (7.87 ± 0.07 Ma; see below) with eruptions of dacitic to andesitic lava flows, and pyroclastic materials, and deposition of lahars, centered on an area ~20 km NW of the current edifice (Fig. 5). Thick lahar deposits (up to ~50 m thick) fill paleo-valleys to the south of Kuh-i-Kharstan (Fig. 3).

In the Quaternary the locus of volcanism shifted east-southeastward toward the current Taftan volcano, with the eruption of lava flows and pyroclastic materials (Figs. 4 and 6). The extensive andesite lava flows retain much of their original morphology and texture. Pyroclastic deposits are mostly andesitic ignimbrite with andesitic and dacitic clasts from the previous eruptions, and pumice fragments, and cover large areas on the distal eastern and southeastern flanks of the Taftan volcano, extending up to 15 km from the vent. The ignimbrite successions reach a thickness of 20 m at the break of slope closest to the vent (Fig. 6). The southern wall of the Taftan crater was destroyed during the last andesitic eruption in the late Pleistocene (Fig. 7; Gazban, 2002).

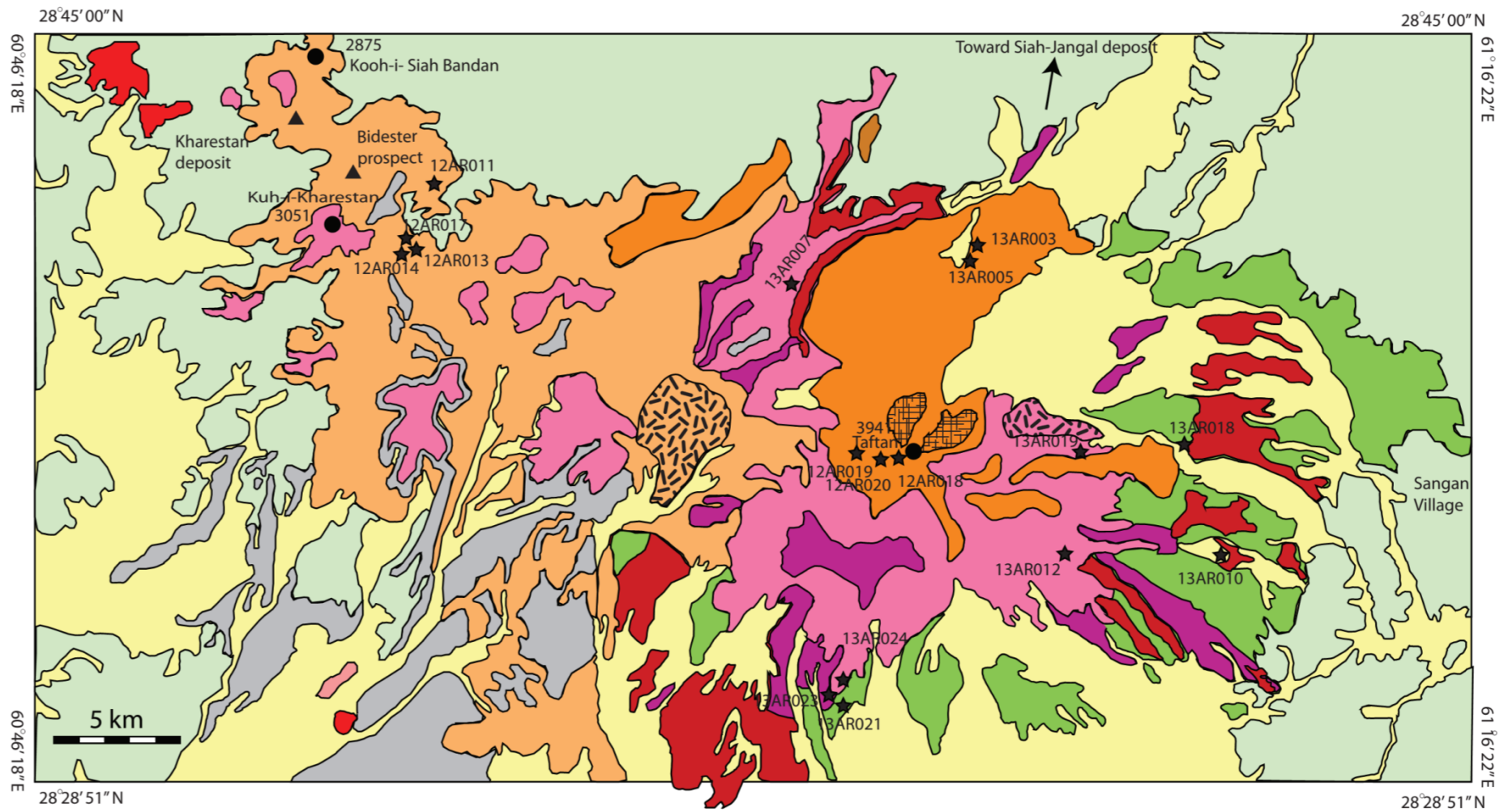
28°45′00″N
28°45′00″N
60°46′18″E
61°16′22″E
2875
Kooh-i- Siah Bandan
Toward Siah-Jangal deposit
Kharestan
deposit
Bidester
prospect
12AR011
Kuh-i-Kharestan
3051
12AR017
12AR014
12AR013
13AR007
13AR003
13AR005
3941
Jaftan
12AR019
12AR020
12AR018
13AR019
13AR018
Sangan
Village
13AR012
13AR010
13AR024
13AR023
13AR021
5 km
60°46′18″E
61°16′22″E
28°28′51″N
28°28′51″N

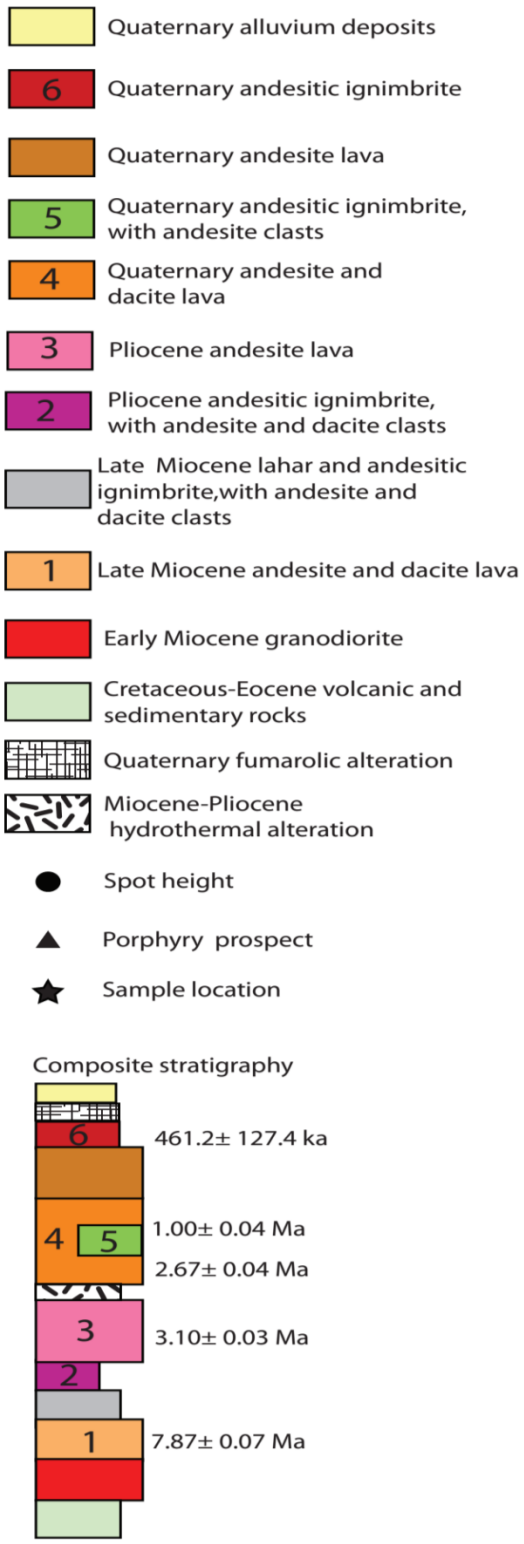

Fig. 3: Geological map of the Taftan volcanic complex, based on 1:100000 geologic map of GSI and field work.

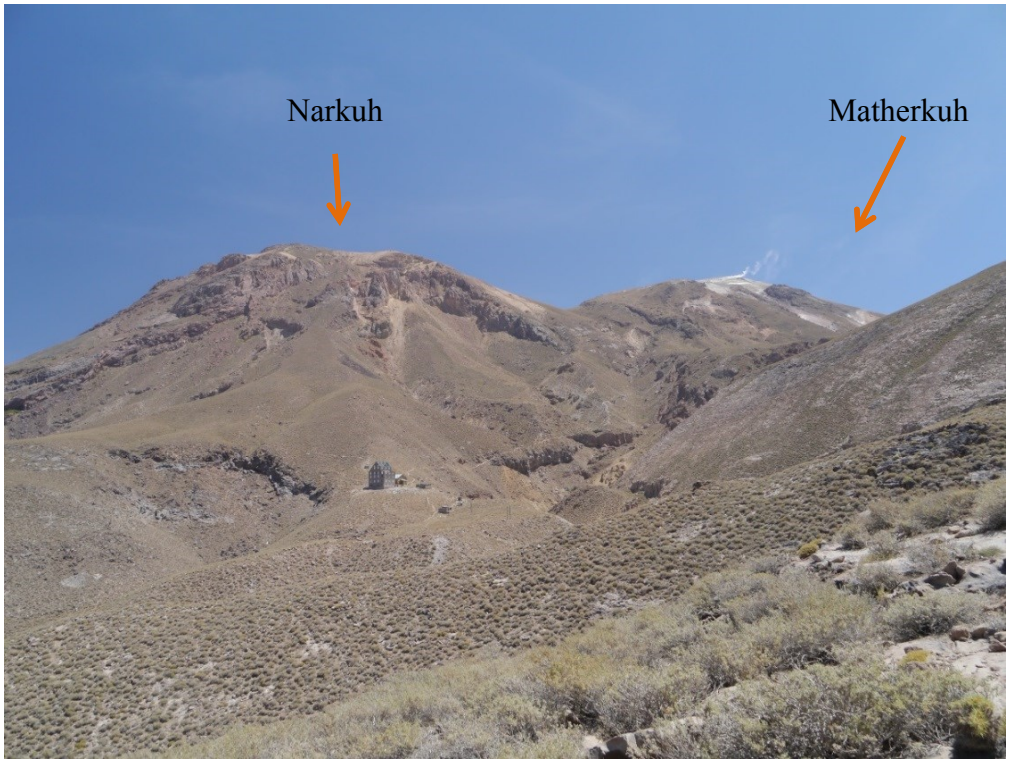

Fig. 4: The current Taftan craters include the saddle shaped Narkuh and Matherkuh vents, with fumarolic activity [Photograph taken at 41R 316577N, 316507E, looking northeast].

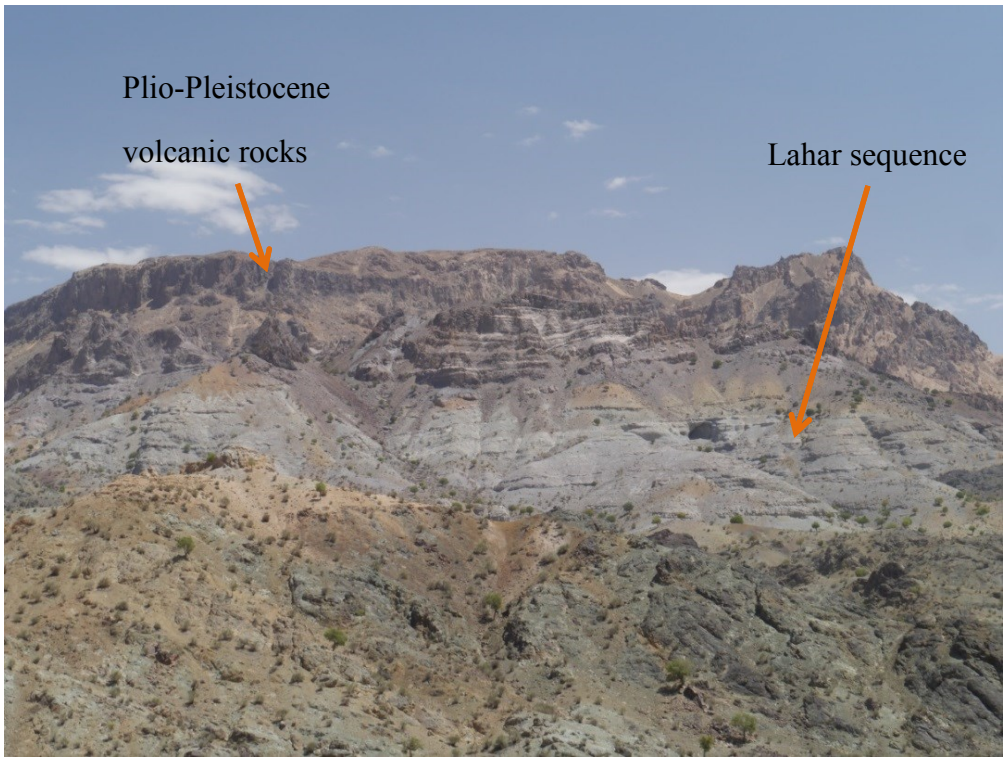

Fig. 5: Pliocene volcaniclastic deposits in valley section near Kuh-i-Kharestan: lahars and tuffs are covered by younger andesitic lava [Photograph taken at 41R 3168820N, 304525E, looking north].

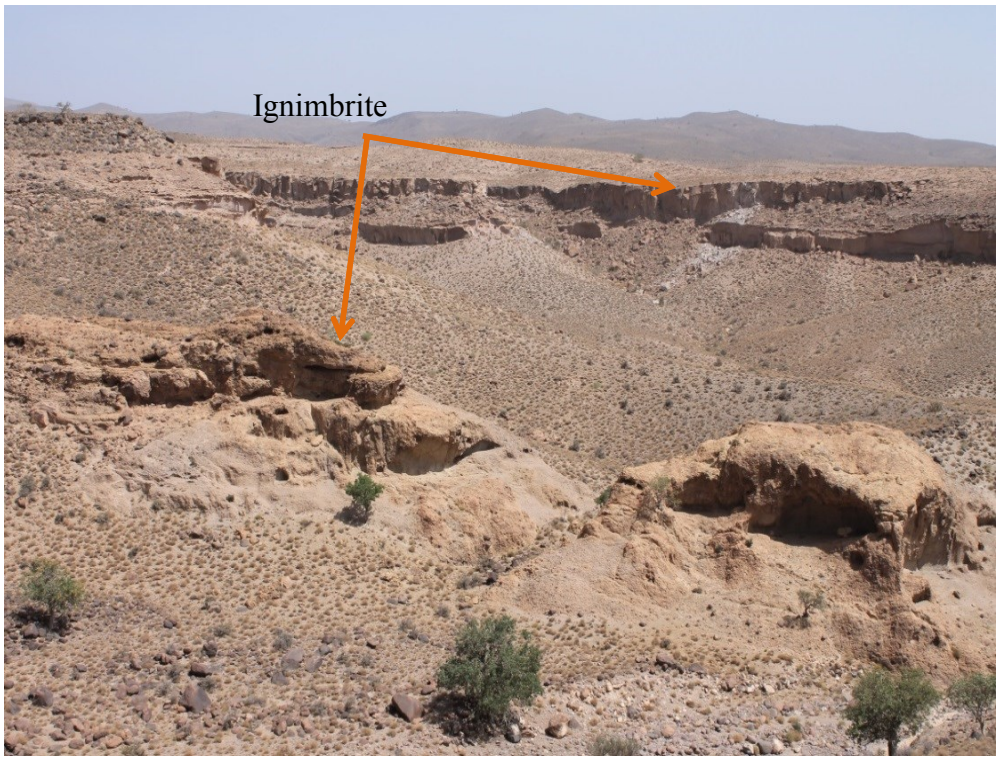

Fig. 6: Thick andesitic ignimbrite-filled valleys on the south and southeast flanks of the Taftan volcano at ~5 km west of Sangan village [Photograph taken at 41R 3166035N, 324823E, looking north-northeast].

Fig. 7: Collapsed crater of the Taftan volcano, overlooking fumarolic vents on summit of Matherkuh [Photograph taken at 41R 3165375N, 317594E, looking northwest].

3.2. Hydrothermal deposits and fumarolic alteration

In the late Miocene, extensive hydrothermal alteration occurred in the TVC. The alteration types are mostly phyllic, argillic, and advanced argillic, and are mostly related to porphyry and epithermal mineralization such as at the Kharestan Cu porphyry prospect in the northwest (Figs. 3 and 8), and the Siah Jangal epithermal Au deposit in the northeast (Figs. 3 and 9). Younger late Miocene–Pliocene argillic and Quaternary fumarolic alteration was also observed in several locations on the west, east, and southeast flanks of the Taftan volcano, but no mineralization related to these alteration zones has been reported to date (Fig. 10).

3.2.1. Kharestan Cu Porphyry prospect

The Kharestan porphyry deposit (6.1 ± 0.4 Ma alunite age in advanced argillic alteration; see below) is hosted by late Miocene andesitic volcanic and subvolcanic rocks, and Eocene flysch (Fig. 8a). It appears to be exposed at a relatively shallow level, with the majority of outcropping alteration consisting of silicified and argillized andesite with abundant disseminated pyrite. Advanced argillic alteration also occurs locally in strongly silicified zones as shown by presence of alunite (Fig. 8b). In two places, to the west and east of the main zone of argillic alteration, stockwork zones in phyllic alteration (overprinted by supergene argillic alteration) were observed (Figs. 8c, d).

Five boreholes have been drilled in the main region of phyllic/argillic alteration down to 500 m in the center of the Kharestan prospect (area of ~2×2 km). Copper grades at the surface are very low but gradually increase with the depth and reach up to ~0.15 % Cu in the potassic alteration zone. Due to the low grades of copper, a resource has not been estimated to date.

3.2.2. Siah Jangal epithermal Au deposit

The Siah Jangal epithermal Au deposit is related to likely mid-late Miocene dioritic to monzodioritic intrusions and is hosted by Mesozoic flysch (Fig. 9a). The main alteration zone

(1.5×5 km) consist of intense argillic alteration in the intrusive and metasedimentary rocks, with locally abundant Fe-oxide staining along fractures (Fig. 9b). Gold grades (up to 8 ppm) have been reported from seven trenches in zones of abundant Fe-oxide veins, which are likely an oxidation product of pyritic veinlets.

3.2.3. Other alteration zones

There are two major argillic and advanced argillic alteration zones on the west and east sides of the Taftan volcano (Fig. 3). These alteration zones are mainly developed in the late Miocene volcanic rocks.

The alteration zone on the west side of Taftan is quite extensive, covering an area of roughly 4×5km, and likely extends below the Quaternary volcanic rocks toward the SE (Fig. 10a).

The extent of the hydrothermal alteration zone on the east side of Taftan is estimated to be roughly 2×1 km, although it likely also extend further beneath younger Quaternary lavas and ignimbrite deposits (Fig. 10b).

There is no significant alteration in the Quaternary volcanic lava flows except near the summit of Taftan where sulfur-rich fumarolic activity has intensely altered the andesitic rocks to clay (Figs. 4 and 10c). Ghazban (2002) reported that these altered rocks mainly consist of alunite, kaolinite, and residual silica.

4. Sampling

Forty six samples of fresh volcanic and plutonic rocks were collected from surface outcrops during two field seasons in August 2012 and July 2013 from the Taftan Volcanic Complex. All surface weathering was removed by hammering in the field, and hand specimens were sent for polished section preparation to ZarAzma laboratory in Tehran. Full details of the samples and their locations are listed in Appendix A. Large (multi-kg) samples were collected in the field, but

much of this material was lost in shipping. Most analyses are therefore based on smaller (~1 kg) hand samples that were shipped separately.

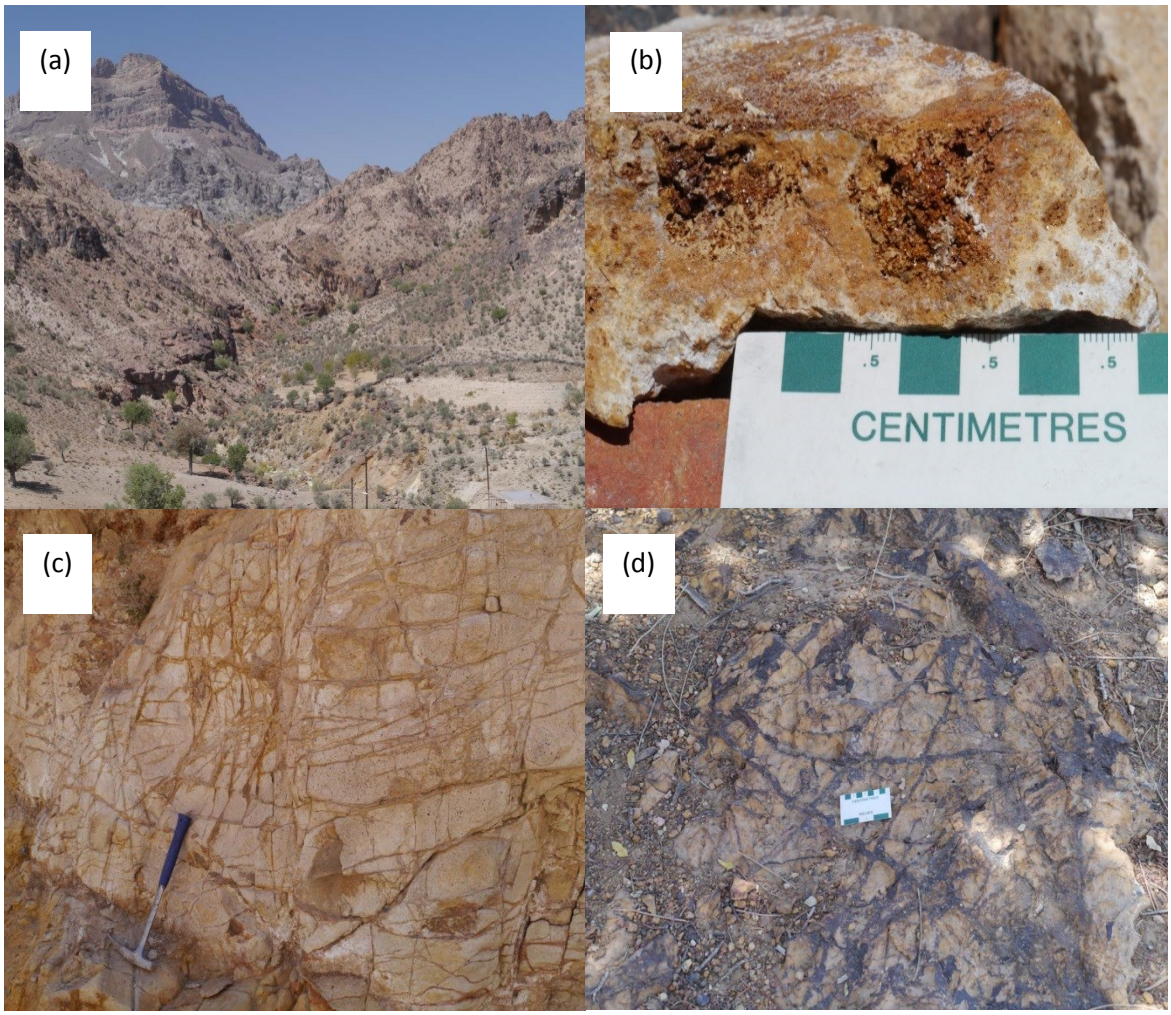

Fig. 8: Hydrothermal alteration in the Kharestan Cu porphyry prospect: (a) Phyllic, argillic, and advanced argillic alteration exposed in valley [Photograph taken from 41R 3177639N, 298578E, looking west]; (b) alunite and jarosite mineralization in strongly silicified samples related to advanced argillic alteration [Photograph taken from 41R 3176274N, 298440E]; (c) oxidized pyrite stockworks in phyllic alteration [Photograph taken from 41R 3177715N, 298277E]; (d) oxidized pyrite stockwork in phyllic alteration with argillic alteration overprint [Photograph taken from 41R 3177301N, 297612E].

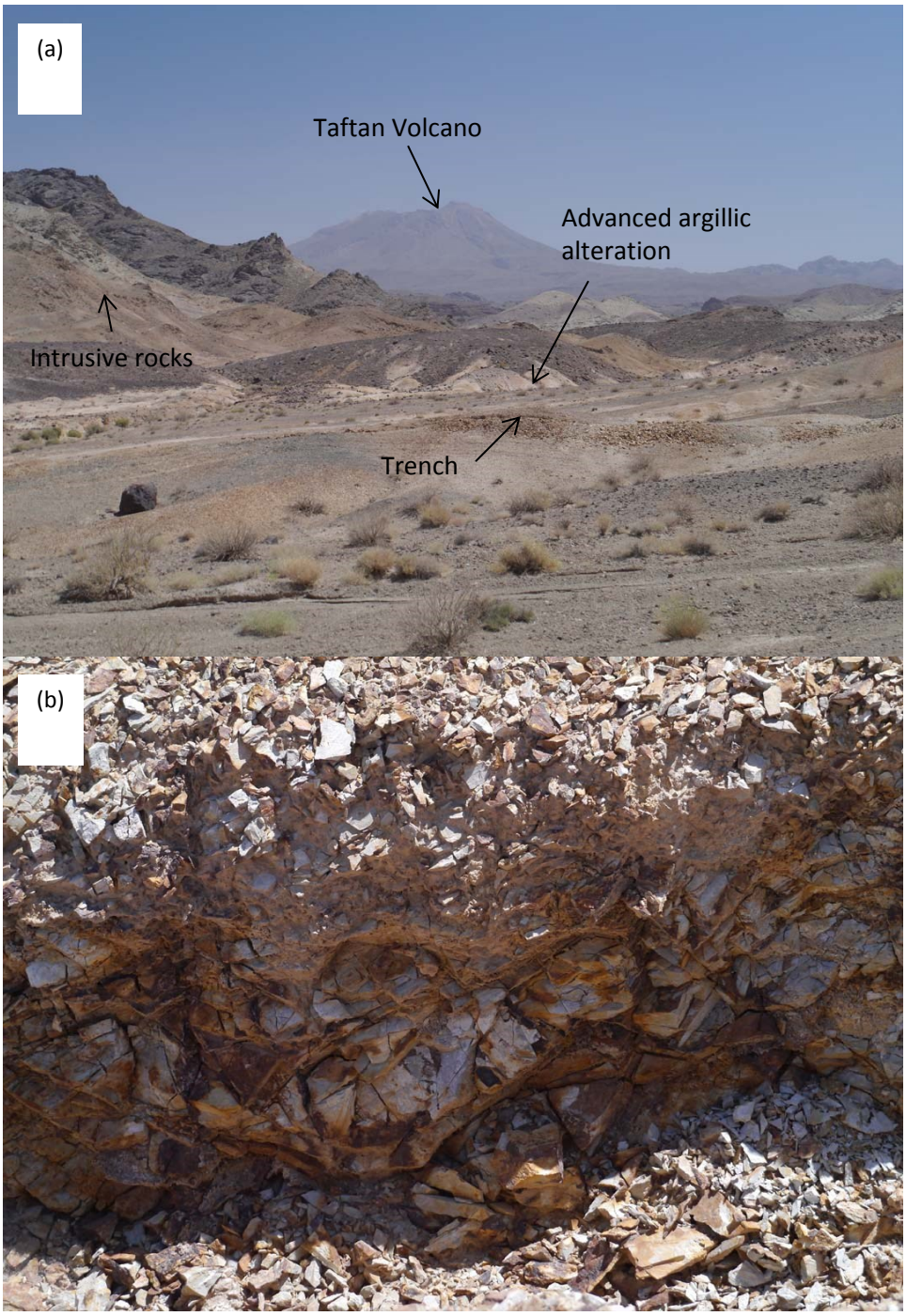

Fig. 9: Siah Jangal epithermal Au deposit (~20 km NE of the Taftan): (a) Argillic alteration in the late Miocene and older intrusive rocks, and location of a trench in high grade Au; (b) Closer view of trench in argillic alteration with high grade Au mineralization (up to 8 ppm) [Trench located at 41R 3184269N, 317362E, looking south].

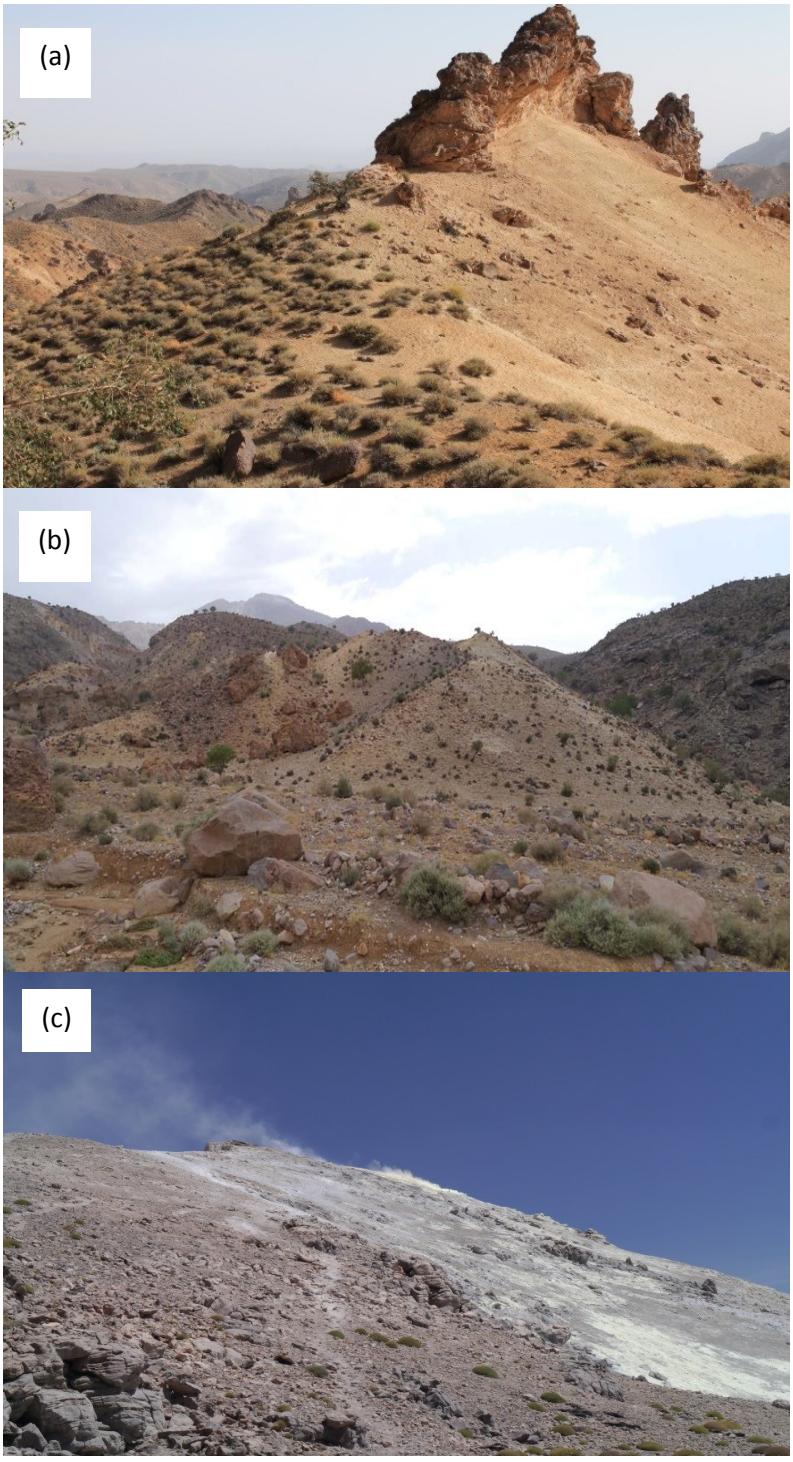

Fig. 10: Field photographs of hydrothermal alteration zones in the TVC: (a) extensive argillic to advanced argillic alteration ~10 km west of current Taftan volcano [Photograph taken at 41R 3169289N, 309904E, looking southwest]; (b) argillic and advanced argillic alteration on the east flank of Taftan, ~10 km west of Sangan village [41R 3165307N, 324608E, looking northwest]; (c) fumarolically altered andesite on top of the Taftan volcano [Photograph taken at 41R 3165150N, 317100E, looking northeast].

5. Analytical techniques

5.1. $^{40}Ar/^{39}Ar$ Geochronology

Biotite and amphibole from fresh rocks of the Taftan volcanic complex were prepared for $^{40}Ar/^{39}Ar$ dating at the University of Alberta. After detailed petrographic study, those samples that had fresh amphibole and biotite were crushed and sieved into >1mm, 1–0.5 mm, and <0.5 mm fractions. Heavy minerals in the 1–0.5 mm fraction were separated by density using bromoform liquid, and whole biotite and amphibole crystals or cleavage fragments were hand picked under a binocular microscope. One sample of alunite from the Kharestan porphyry prospect was also prepared.

Mineral aliquots were analyzed at the Nevada Isotope Geochronlogy Laboratory at the University of Nevada, Las Vegas. Details of analytical methods are listed in Appendix B.

5.2. Electron Microprobe Analysis

The compositions of amphibole, orthopyroxene, and clinopyroxene phenocrysts, and Fe-Ti oxide microphenocrysts in 16 polished thin sections of volcanic rocks from the Taftan volcanic complex were analyzed by wavelength dispersive spectrometry (WDS), using a JEOL 8900 electron probe micro-analyser at the University of Alberta, operating with a 15 nA beam current, 15 kV accelerating potential, and 1 μm beam diameter for all minerals. Natural minerals and oxides were used for calibration and standardization. The CITZAF method of Armstrong (1995) was used for data reduction, and detection limits were typically lower than 300 ppm for major elements and less than 1300 ppm for fluorine. Average relative standard deviations of major elements as determined by 4-8 replicate analyses of standards (augite and kaersutite) were better than <5 relative % for most major elements. Cr_2O_3 and MnO had relative standard deviations above 10 relative %.

Fe^{2+} and Fe^{3+} concentrations in amphibole analyses were estimated using the formula of Leake et al. (1997). Amphibole chemical compositions were recalculated using the Probe-AMPH

Excel spreadsheet (Tindle and Webb, 1994), and elemental site occupancies were calculated using the Excel spreadsheet of Locock (2014).

The ILMAT Excel spreadsheet (Lepage, 2003) was used to recalculate magnetite and ilmenite compositions and to estimate crystallization temperatures and oxidation states based on Fe-Ti oxide mineral pairs that were in textural equilibrium (as determined by petrographic and scanning electron microscope (SEM) imaging.

Magmatic temperatures and oxygen fugacities were also estimated using the amphibole geothermometer of Ridolfi et al. (2010), and pressures were estimated using the aluminum barometer of Schmit (1992). An average upper crust density of 2.7 g/cm^3 and lithostatic pressure gradient of 26.6 MPa/km were assumed for pressure-depth conversion. Magmatic water content was calculated from amphibole compositions using the solubility model of Moore et al. (1998).

5.3. Whole rock geochemistry

Twenty one samples for geochemical analysis were prepared in two stages. Samples collected in 2012 were prepared at ZarAzma laboratory (Tehran, Iran) by crushing and grinding in a steel mill, whereas samples collected in 2013 were shipped directly to Canada and were prepared by crushing (mostly by jaw crusher, but some samples were crushed by hammer) and grinding in a steel ring mill (SPEX 8500 Shatterbox®) at the University of Alberta. All powdered samples were sent to Activation Laboratories (Ancaster, Ontario, Canada) for analysis.

A combination of fusion inductively couple plasma mass spectrometer (FUS-ICP-MS) and instrumental neutron activation analysis (INAA) was used (Actlabs 4E-Research analytical package with ICP-MS). For each sample, a 0.2 gram split of milled powder was fused with a lithium metaborate/lithium tetraborate mixture, and was then digested in 5% HNO_3 followed by ICP-MS analysis. For INAA, one gram aliquots were irradiated at a thermal neutron flux of 7×10^{12} n cm^{-2} s^{-1} for a week prior to gamma ray analysis. Limits of detection for major elements were 0.01 wt.%, except MnO and TiO_2 that were 0.001 wt.%. Trace elements generally have detection limits less than 1 ppm. Accuracy for major elements, as determined by reproducibility of standards and duplicates, is typically within 5 relative % (< 3 relative % for SiO_2 and Al_2O_3),

and to within 10 relative % for minor and trace elements.

6. $^{40}Ar/^{39}Ar$ geochronological results

The results of $^{40}Ar/^{39}Ar$ analyses of 5 samples of volcanic rocks from the Taftan area and one alunite sample from the Kharestan porphyry-epithermal deposit are listed in Appendix C and illustrated in Fig. 11.The alunite plateau age was 6.10 ± 0.40 Ma, suggesting that alteration was related to late Miocene hydrothermal activity (Fig. 11a).

Four biotite samples yielded undisturbed age spectra, yielding plateau ages of the late Miocene (7.87 ± 0.07 Ma) to the late Pleistocene (1.00 ± 0.04 Ma; Figs. 11b–e).

One amphibole sample from a pumice fragment in an ignimbrite (sample 13AR017) did not yield a plateau age (Fig. 11f). Early steps yielded ages between 6.1 ± 1.2 Ma and 7.2 ± 2.2 Ma, whereas the later nine steps yielded an average gas age of 461.2 ± 127.4 ka (See Appendix C). The older apparent ages in early steps may be due to the presence of excess ^{40}Ar. Although no plateau age was achieved for this sample, the average gas age from the later steps suggests a Quaternary (late Pleistocene) age for this ignimbrite.

7. Petrography of volcanic rocks from the Taftan Volcanic Complex

Polished thin sections of all collected samples were studied using a petrographic microscope to determine mineralogy and texture, and are described below in terms of the six spatio-temporal groups mapped in Fig. 3.

7.1. Group 1: Late Miocene andesitic and dacitic lava flows

Voluminous andesite dacite lava flows form the oldest phase of Taftan volcanism, and cover the western part of the TVC. The lavas are fairly uniform in composition and texture but in some

localities show flow banding. A representative sample of andesite (Sample 12AR017) yielded plateau age of 7.87 ± 0.07 Ma.

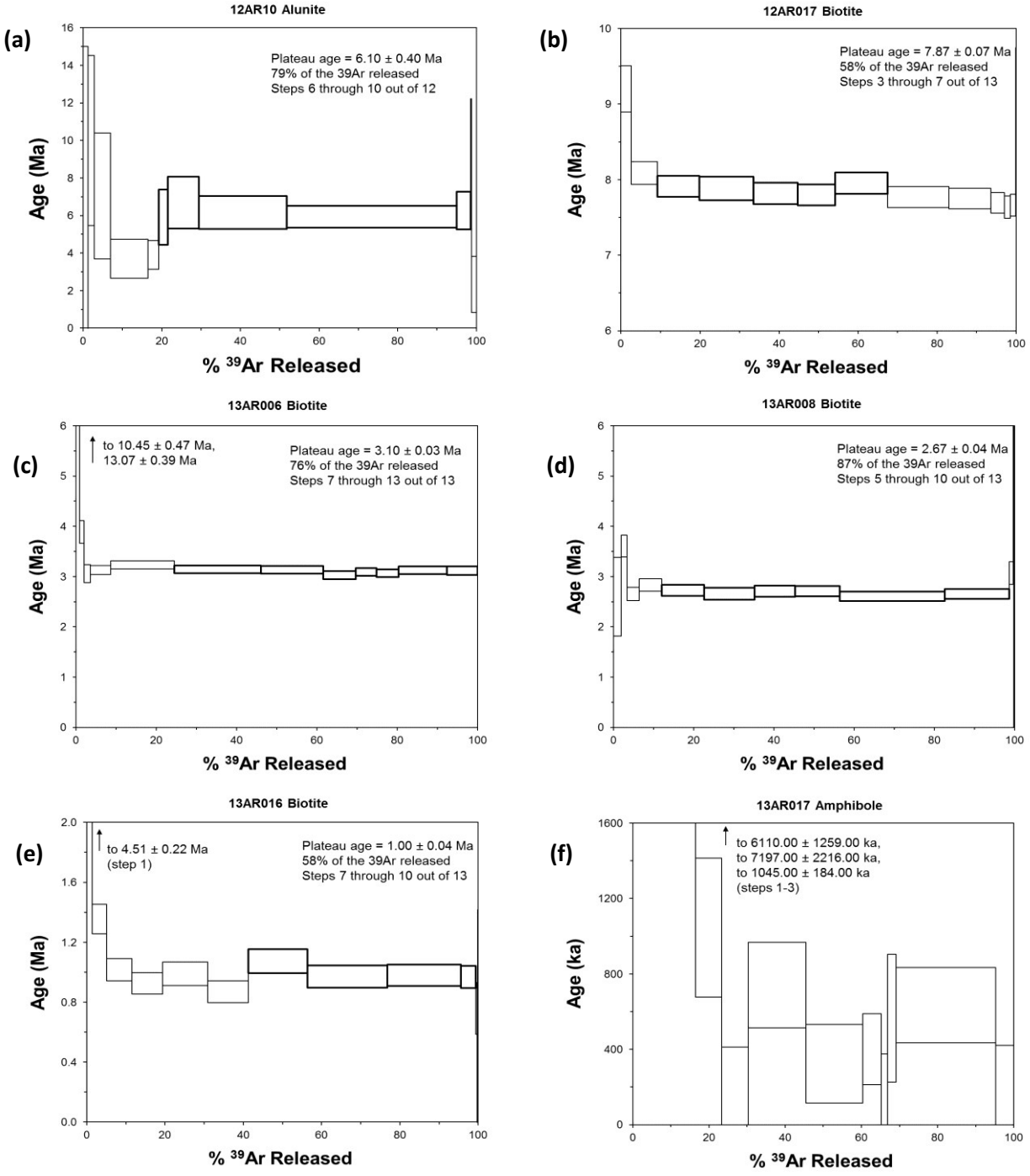

Fig. 11: $^{40}Ar/^{39}Ar$ apparent age spectra for (a) one hydrothermal alunite sample from the Kharestan porphyry deposit, and (b-e), four biotite samples and (f) one amphibole sample from volcanic rocks in the TVC.

Phenocryst assemblages consist of plagioclase, amphibole, and orthopyroxene, with lesser microphenocrysts of magnetite and ilmenite. Plagioclase crystals are mostly fresh. Some large plagioclase phenocrysts include melt inclusion (Fig. 12a). Amphibole commonly shows some degree of oxidation (opacitization). Some of the magnetite grains are also partially oxidized to hematite, which probably occurred during eruption (along with amphibole opacitization; see discussion below). The groundmass is typically partially devitrified (spherulitic), and includes fine grained plagioclase microcrystals (Fig. 12a).

7.2. Groups 2-5: Plio-Pleistocene andesite and dacite lava flows

Four map units of andesitic to dacitic lava flows and tuffs are recognized in the east of the TVC (Fig. 3). These units consist of late Pliocene andesitic lava flows (unit 2; sample 13AR006: 3.10 ± 0.03 Ma, and sample 13AR008: 2.67 ± 0.04 Ma), Pleistocene andesitic to dacitic lava flows (unit 3), and andesitic to dacitic clasts in the Quaternary andesitic ignimbrite units (units 4, 5; sample 13AR016: 1.00 ± 0.04 Ma). Around the current Taftan crater, the primary morphology of the lavas is well preserved. Flow banding is commonly present in the Quaternary andesite and dacite lavas on the northern side of the Taftan volcano (unit 3). Major phenocryst phases in andesites are amphibole, plagioclase, orthopyroxene, and clinopyroxene with minor magnetite and ilmenite. Dacite samples mostly contain amphibole, plagioclase, and orthopyroxene phenocryst, with lesser amounts of biotite, quartz, rutile, titanite, magnetite, and ilmenite. Most of the plagioclase microphenocrysts are fresh but some grains are spotted by sericite. Plagioclase shows oscillatory zoning and sieve textures (Fig. 12b). Resorption is abundantly observed in quartz phenocrysts (Fig. 12c). Ferromagnesian minerals (amphibole, biotite, and pyroxene) are mostly fresh, but some grains are partially to completely opacitized (Figs. 12c and d). Most biotite phenocrysts are euhedral to subhedral in shape.

The matrix is typically fine-grained to glassy, variably devitrified, and locally vesicular. Glassy groundmass is normally colorless in thin section, but in some samples light to dark brown glass occurs interstitially. Lath-shaped plagioclase and amphibole crystallites occur in the matrix.

Some enclaves are also observed in dacitic rocks on the east and southeast sides of the Taftan volcano. The enclaves mainly consist of clusters of amphibole (commonly opacitized; Fig. 12e), plagioclase, and minor orthopyroxene, suggesting derivation from earlier crystallized magma below the volcano.

7.3. Group 6: Quaternary ignimbrite

Poorly welded ignimbrites (sillars) are the youngest morphological features in the map area (unit 6, Fig. 3; sample 13AR017: 461.2 ± 127.4 ka). The ignimbrite deposits mainly occur on shallow slopes of the distal eastern and southeastern flanks of the Taftan volcano. They are mainly composed of andesitic tuff, yellowish white in color, with lithic fragments that include clasts of andesite, dacite, and pumice (up to few decimeters in diameter), and greenschist fragments from the underlying basement (Emami, 2000). The ignimbrite deposits reach thicknesses of ~20 m close to the foot of the volcano, and directly overlie Eocene flysch deposits. They are well exposed in the walls of gullies and valleys that have been cut into the relatively soft deposits (Fig. 6).

The glassy ignimbrite matrix contains phenocrysts of plagioclase, amphibole, pyroxene (orthopyroxene is dominant), and biotite, with microphenocrysts of magnetite and ilmenite. Plagioclase phenocrysts are subhedral and show oscillatory zoning. The ashy matrix is partially welded and vesicles are common. Flattened and stretched pumice clasts (fiamme) are also abundant, indicating some compaction and secondary mass flow of the ignimbrite after deposition (Cas and Wright, 1991; Fig. 12f).

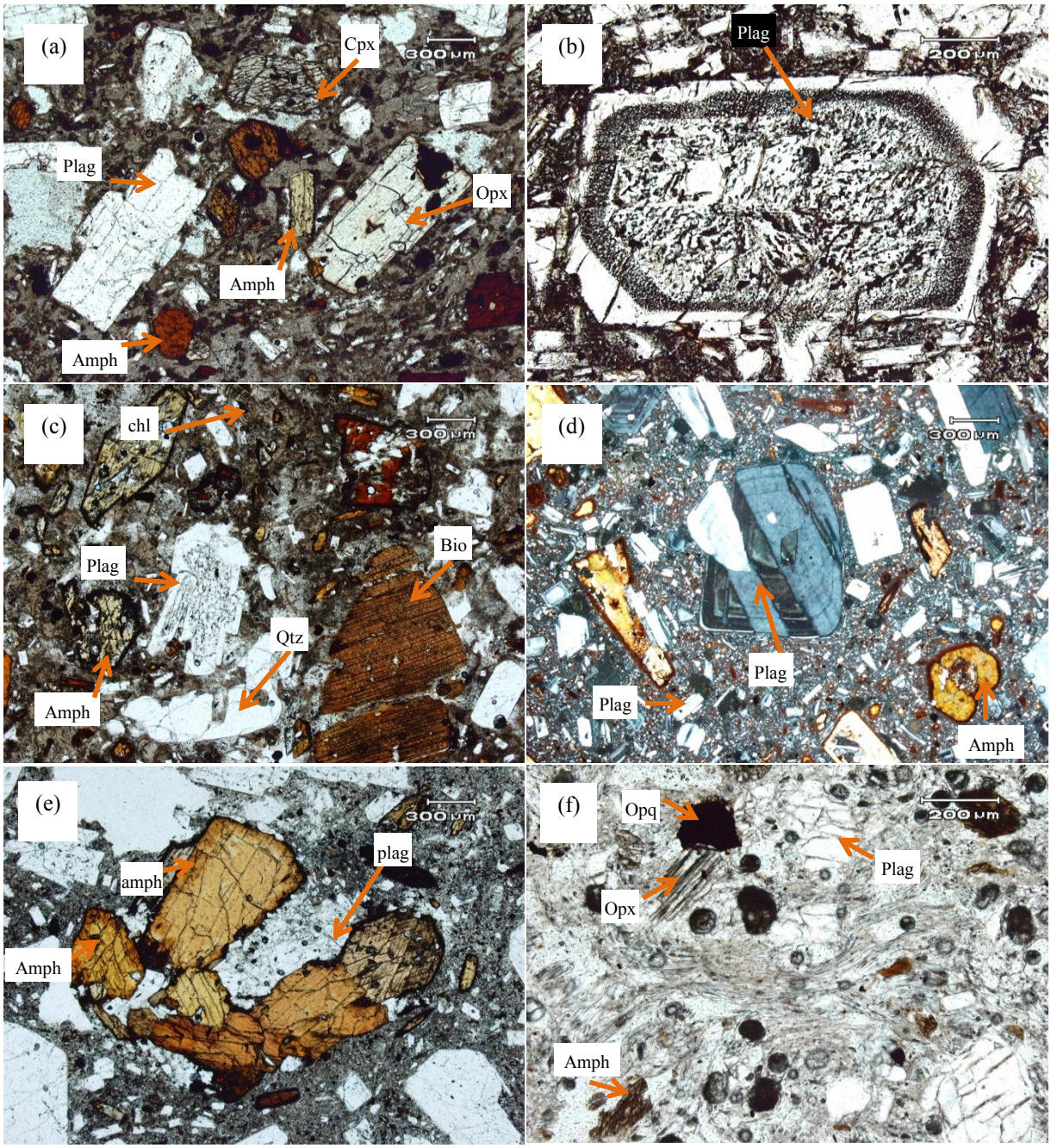

Fig. 12: Photomicrograph of volcanic rocks from the TVC: subhedral to euhedral plagioclase, amphibole (with partially oxidized rims), and pyroxene phenocrysts from the late Miocene andesite (sample 12AR017); (b) large sieve-textured plagioclase crystal from the Plio-Pleistocene dacite (sample 13AR007); (c) partially devitrified groundmass with fine-grained plagioclase and partially resorbed quartz grain (sample 13AR007); (d) subhedral to euhedral oscillatory zoned plagioclase, and amphibole phenocrysts with partially oxidized rims from the Plio-Pleistocene andesite (sample 13AR008); (e) a patch of amphibole-plagioclase enclave in the Plio-Pleistocene dacite host rock (sample 12AR020); (f) flattened pumice clasts (fiamme) in andesitic tuff (sample 13AR017). Abbreviations: Amph = amphibole, Bio = biotite, chl = chlorite, opq = opaque mineral, opx = orthopyroxene, cpx = clinopyroxene, plag = plagioclase, qtz = quartz.

8. Mineralogy of volcanic rocks from the Taftan Volcanic Complex

8.1. Pyroxenes

Orthopyroxene and clinopyroxene are abundant in all rock samples from andesite to dacite composition. Representative analyses of both types of pyroxene are listed in Table 1. Pyroxene phenocrysts mostly occur in glomeroporphyrytic clusters with plagioclase and rarely with olivine. Measured FeO_{total} was converted to FeO and Fe_2O_3 using Droop's formula (1987). Mg# (MgO/(FeO + MgO)) was then calculated for both clinopyroxene and orthopyroxene. The Mg# of clinopyroxene phenocrysts ranges from 79.3 to 65.5 (average 73.2 ± 7.0, n = 4), whereas for orthopyroxene phenocrysts it ranges from 71.9 to 65.3 (average = 67.6 ± 1.9, n = 9). A zoned orthopyroxene crystal in one andesite sample shows a more magnesian and titanium-rich rim than its core (e.g., compare analyses from sample 13AR003 in Table 1).

8.2. Magnetite and ilmenite

Representative analyses for magnetite and ilmenite are listed in Table 1. Magnetite is the most abundant opaque mineral phase in andesitic and dacitic rocks from the Taftan volcanic complex. Crystals are normally smaller than 200 μm and occur as either individual microphenocrysts in the groundmass or as inclusions within ferromagnesian silicate phases. Martitization locally occurs in some samples, and those samples were excluded from analysis. Magnetites from a late Miocene andesite sample (12AR013) contain 0.12 to 0.15 wt.% Cr_2O_3 (average = 0.13 ± 0.02 wt.%, n = 4), and 1.14 to 8.4 wt.% TiO_2 (average = 4.40 ± 2.46 wt.%, n = 4).

Magnetite phenocrysts from Plio-Pleistocene andesite samples (13AR003 and 13AR018) contain 0.06 to 0.12 wt.% Cr_2O_3 (average = 0.10 ± 0.03 wt.%, n = 6) and 7.8 to 10.9 wt.% TiO_2 (average = 9.43 ± 1.25 wt.%, n = 6).

Minor ilmenite also occurs in most rock samples as small (<100 μm) lath-shaped crystals in the groundmass, as exsolution lamellae in magnetite, or as equilibrium intergrowths with magnetite grains (Fig. 13). Compositions of ilmenites from the late Miocene andesite sample

vary from 40.7 to 45.8 wt.% TiO_2 (average = 44.3 ± 1.2 wt.%, n = 4) and 0.1 to 3.8 wt.% MgO (average = 1.8 ± 1.4 wt.%, n = 4), whereas ilmenites in the Plio-Pleistocene andesite samples contain 30.8 to 47.2 wt.% TiO_2 (average = 38.6 ± 6.6 wt.%, n = 6) and 1.4 to 4.6 wt.% MgO (average = 2.5 ± 1.3 wt.%, n = 6).

8.3. Amphiboles

Amphibole phenocrysts in the Taftan volcanic rocks typically occur as euhedral to subhedral crystals, with sizes from 0.2 mm up to 5 mm in length. However, crystals larger than 10 mm are also observed in some andesite samples (e.g., 12AR018 and 13AR013). Most amphibole phenocrysts in the Taftan volcanic rocks contain small plagioclase and apatite inclusions (Figs. 14a and b). Resorption textures are also visible in many of the amphibole grains (Fig. 14c), in which the edge of the amphibole grain is embayed. Many crystals also show oxidation reactions in which amphibole rims are replaced by "opacite" or Fe-Ti oxide (Figs. 14b and d). Oxidation of amphiboles in andesite samples is typically incomplete and opacitized rims were not observed to exceed a thickness of 100 μm, but in many dacite samples some of the amphibole phenocrysts are totally opacitized (Fig. 14e). This texture can be attributed either to oxidation or depressurization during magma ascent (Rutherford and Hill, 1993; Chambefort et al., 2013).

The compositions of amphibole phenocrysts from the Taftan volcanic complex were recalculated based on 23 oxygen atoms per formula unit (apfu), and are presented in Table 3. The 23 oxygen apfu has been calculated based on 24 anions (22O+2(OH,F,Cl)) which yields 46 negative charges and is equivalent to 23 oxygen apfu (Leake et al., 1997). All samples are Mg-rich calcic amphiboles and can be classified as aluminum-rich and aluminum-poor varieties (hereafter high-Al, and low-Al). They vary from alkali-rich (Na+K+2Ca > 0.5) pargasite to low-alkali (Na+K+2Ca < 0.5) magnesio-hornblende (Hawthorne et al., 2012; Fig. 15). Amphibole compositions gradually change from high-Al pargasite to low-Al magnesio-amphibole from the late Miocene to the Plio-Pleistocene lava flows (Fig. 15).

The low-Al amphiboles in dacite are mostly magnesio-hornblende with Mg# (MgO/(FeO + MgO)) from 0.74 to 0.82 (average = 0.78 ± 0.04, n = 26). In contrast, high-Al amphiboles in

dacite samples are pargasitic in composition and have Mg# (0.69 to 0.90; average = 0.81 ± 0.04, n = 12).

The low-Al amphiboles in andesitic rocks have similar compositions to those from dacite samples and range from pargasite to magnesio-hornblende with Mg# from 0.66 to 0.87 (average = 0.78 ± 0.07, n = 21). The high-Al amphiboles in andesite are characterized by dominantly paragasitic compositions with Mg# from 0.66 to 0.96 (average = 0.81 ± 0.08, n = 26).

Volatile contents (F, Cl, and OH*) in both low-Al and high-Al amphibole samples were also analyzed by EPMA and are listed in Table 2. The water contents (OH*) were calculated based on the formula of Leake et al. (1997) by assuming two OH sites filled by OH^- (2-F-Cl). The water content of the parent magmas was estimated from these OH* values, and indicates that the late Miocene magmas had water contents of 4.9 to 5.8 wt.% (average = 5.3 ± 0.8 wt.%, n = 7), whereas the late Plio-Pleistocene andesites had slightly higher water contents, ranging from 4.2 to 8.0 wt.% (average = 5.5 ± 0.7 wt.%, n = 48).

No amphiboles from late Miocene dacite samples were analyzed because they are mostly decomposed to opacite. However, amphiboles from late Plio-Pleistocene dacites indicated similar magmatic water contents, ranging from 3.6 to 7.2 wt.% (average = 5.3 ± 0.7 wt.%, n = 17).

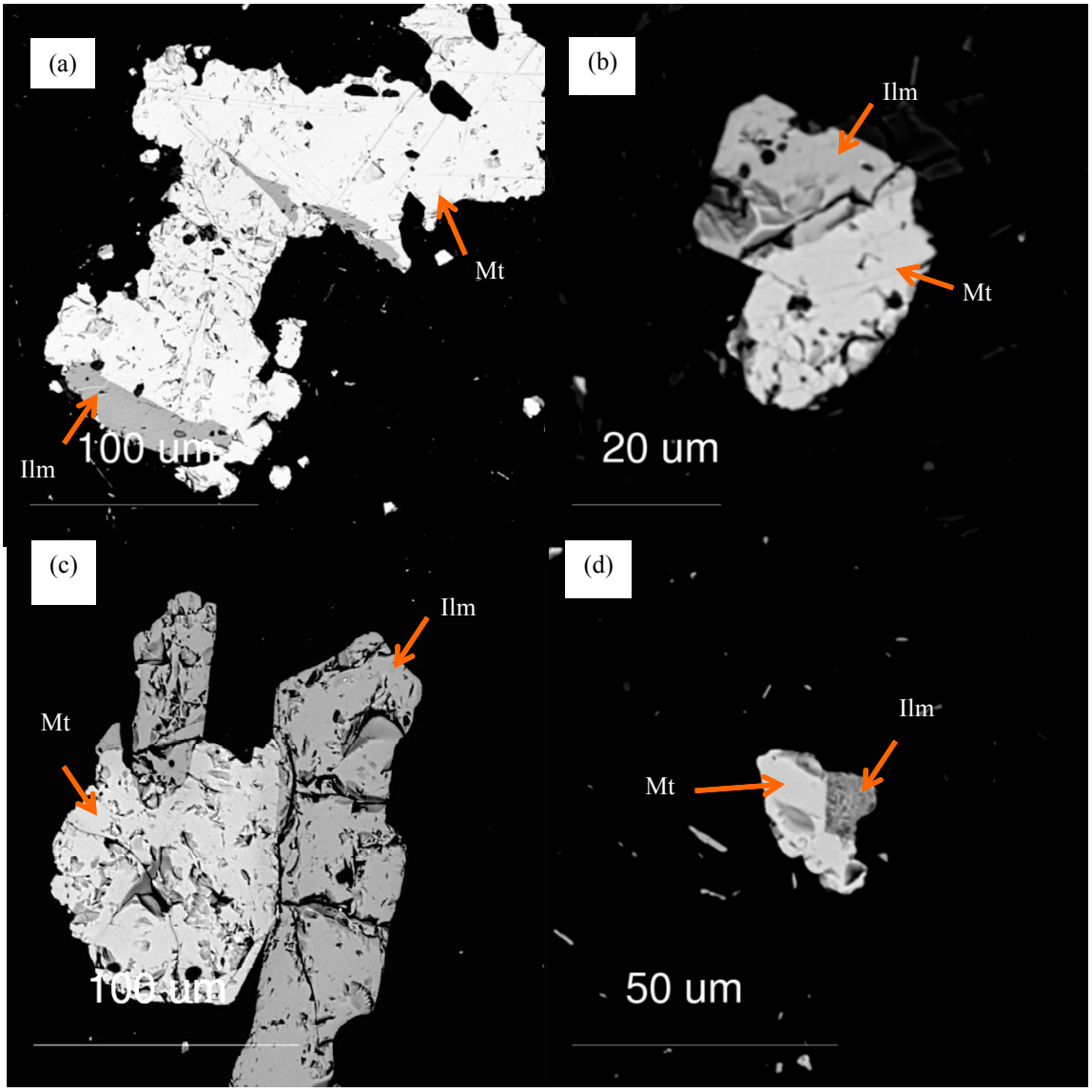

Fig. 13: Back scattered electron images (BSEI) of magnetite and ilmenite grains in volcanic rock samples from the TVC: (a) Sample 13AR003 from Plio-Pleistocene andesite with minor exsolution lamellae of ilmenite; (b-c) Sample 13AR006 from the late Pliocene andesite with magnetite and ilmenite intergrowths; (d) Sample 12AR013 of late Miocene andesite with magnetite and ilmenite intergrowths. Abbreviations: Ilm = ilmenite, Mt = magnetite.

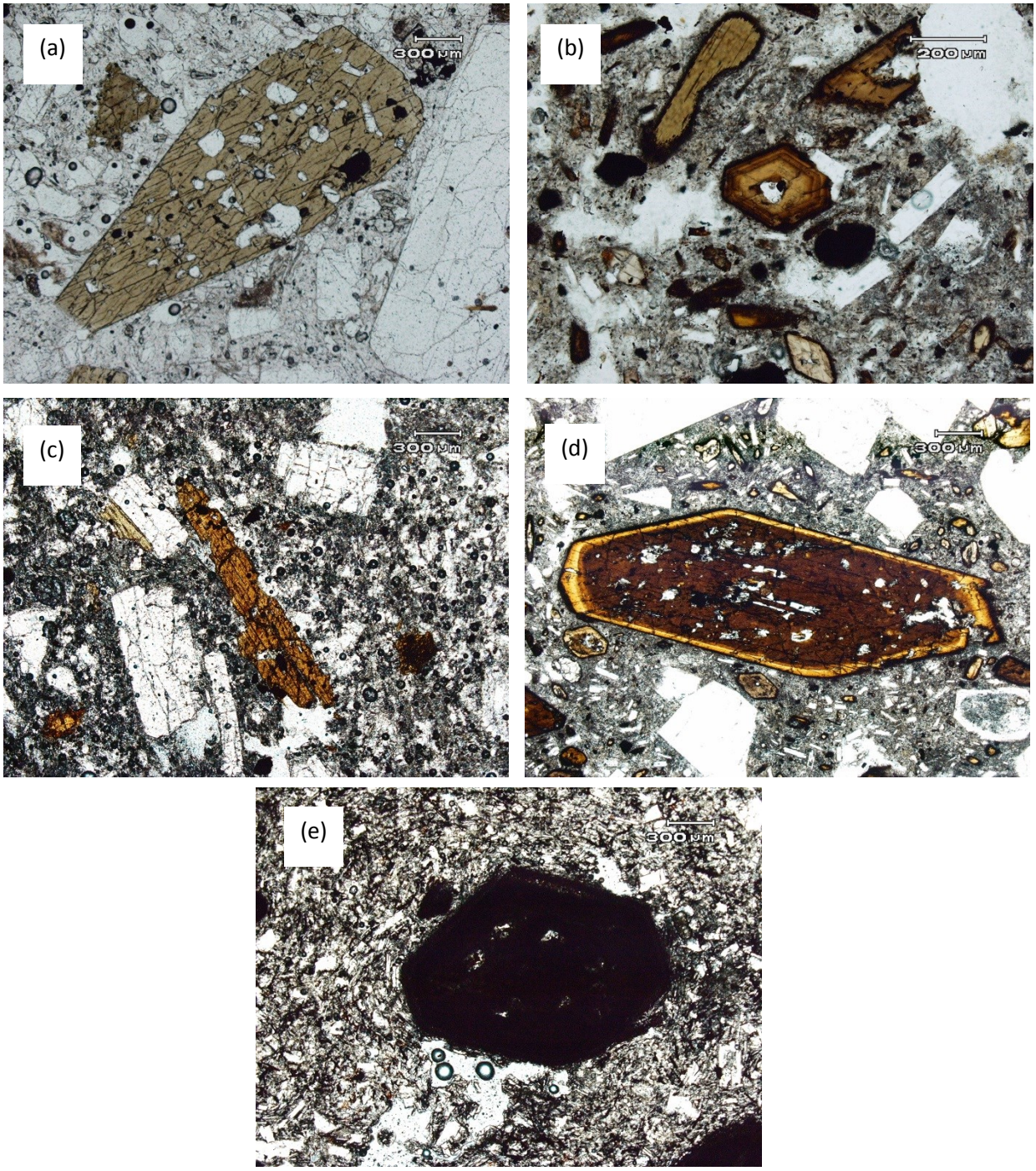

Fig. 14: Photomicrographs of amphiboles in volcanic rocks from the TVC: (a) Amphibole crystal containing plagioclase inclusions from Plio-Pleistocene andesite (13AR013); (b) Amphibole crystal partially decomposed to Fe-Ti oxide with reacted rim and embayment along the crystal edge from late Miocene andesite (12AR017); (c) Partially resorbed amphibole crystal from Plio-Pleistocene andesite (13AR005); (d) Thin opacitic rim (Fe-Ti oxides) along the crystal suface with multiple internal zoning in Plio-Pleistocene andesite (13AR016); (e) Completely decomposed amphibole (opacite) in Plio-Pleistocene dacite (13AR007).

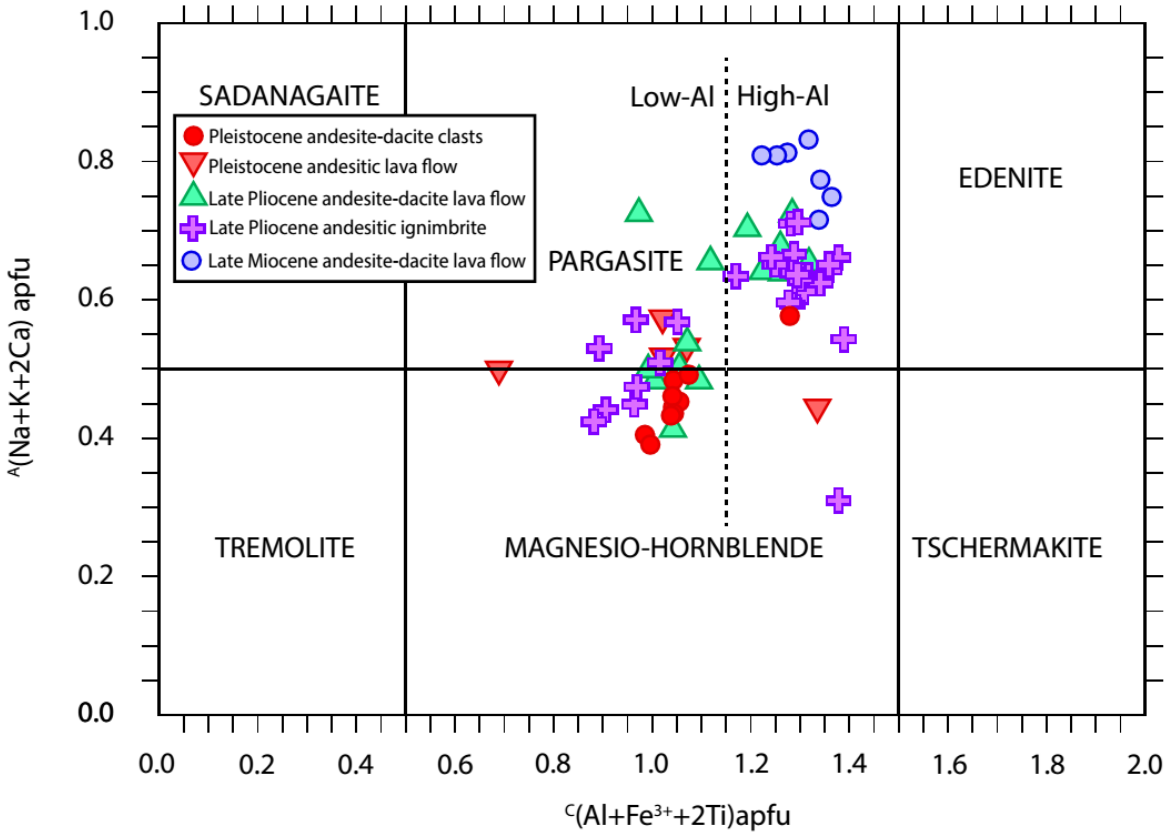

Fig. 15: Amphibole compositions from the TVC. The late Miocene samples are mostly high-Al pargasite whereas the Plio-Pleistocene amphiboles vary in composition from high-Al pargasite to low-Al magnesio-hornblende. A and C refer to A-site and C-site in amphibole crystallographic structure (See Leake et al., 1997).

9. Geochemistry of volcanic rocks

9.1. Whole–rock geochemistry

Whole-rock data for samples from the Taftan volcanic complex are listed in Table 3. For petrological classification purpose, major element compositions were normalized to 100% volatile free. Most samples had low loss-on-ignition (LOI) contents (<1.5 wt.%) except for 5 more altered samples that had LOI between 2.4-8.7 wt.%. Volcanic rock samples are classified based on the IUGS definition of total alkalis versus silica (TAS; Le Maitre, 1989), and are illustrated in Fig. 16a.

Table 1: Representative electron microprobe analyses of magnetite, ilmenite, and pyroxene from the TVC rock samples.

Sample	Magnetite				Ilmenite			
#	**12AR013-Mag1**	**12AR013-mag4**	**13AR003-MAG1**	**13AR006-MAG2**	**12AR013-ilm1**	**12AR013-ilm4**	**13AR003-ILM1**	**13AR006-ILM2**
Weight %								
SiO_2	0.10	0.11	0.07	0.11	0.05	0.04	0.08	0.03
TiO_2	8.38	3.27	8.21	9.45	44.86	45.82	45.81	33.55
Al_2O_3	1.33	1.89	0.97	2.86	0.13	0.15	0.17	0.47
FeO Total	81.66	86.93	81.80	80.54	46.44	47.70	45.17	60.66
MnO	0.56	0.18	0.20	0.50	1.83	1.14	0.60	0.32
MgO	1.45	0.67	0.53	1.60	3.87	1.97	1.42	1.57
CaO	0.07	0.02	0.07	0.03	0.06	0.08	0.06	0.02
Na_2O	b.d.l.	b.d.l.	b.d.l.	0.02	0.03	b.d.l.	0.03	0.02
K_2O	0.02	0.01	0.01	0.02	0.01	0.01	0.01	0.01
Cr_2O_3	0.13	0.12	0.12	0.09	0.05	0.04	0.05	0.07
F	b.d.l.	b.d.l.	b.d.l.	b.d.l.	b.d.l.	b.d.l.	b.d.l.	b.d.l.
Cl	b.d.l.	b.d.l.	b.d.l.	b.d.l	b.d.l.	b.d.l.	b.d.l.	b.d.l.
Total	93.71	93.19	92.00	95.20	97.34	96.96	93.40	96.73
	Number of cations based on 4 oxygens				Number of cations based on 3 oxygens			
Apfu								
Si	0.0038	0.0042	0.0029	0.0040	0.0012	0.0011	0.0020	0.0008
Ti	0.2393	0.0938	0.2408	0.2638	0.8410	0.8772	0.9159	0.6370
Al	0.0596	0.0848	0.0447	0.1249	0.0037	0.0044	0.0052	0.0140
Fe^{3+}	1.4497	1.7153	1.4641	1.3365	0.3096	0.2382	0.1573	0.7086
Fe^{2+}	1.1404	1.0533	1.2032	1.1620	0.6586	0.7769	0.8464	0.5715
Mn	0.0179	0.0058	0.0067	0.0156	0.0386	0.0245	0.0135	0.0067
Mg	0.0817	0.0378	0.0308	0.0887	0.1436	0.0747	0.0562	0.0590
Ca	0.0028	0.0008	0.0029	0.0012	0.0015	0.0022	0.0018	0.0005
Na	0.0000	0.0000	0.0000	0.0011	0.0016	0.0000	0.0016	0.0010
K	0.0011	0.0006	0.0004	0.0009	0.0004	0.0002	0.0003	0.0003
Cr	0.0038	0.0036	0.0038	0.0025	0.0010	0.0008	0.0009	0.0015
Total	3.0007	3.0004	3.0002	3.0013	2.0013	2.0001	2.0013	2.0009

Table 1: Continued

Sample	Orthopyroxene		Clinopyroxene	
#	**13AR018-Opx-3**	**12AR020-OPX1-1**	**12AR020-CPX1-1**	**12AR013-1-Cpx-2**
Weight %				
SiO_2	53.09	52.43	53.09	51.18
TiO_2	0.09	0.15	0.15	0.66
Al_2O_3	0.85	0.66	0.79	3.95
FeO Total	21.17	19.86	19.72	7.64
MnO	1.01	0.84	0.82	0.20
MgO	23.84	23.61	24.61	16.43
CaO	0.73	1.59	0.82	20.41
Na_2O	0.02	0.03	0.03	0.32
K_2O	0.01	0.02	0.02	0.01
Cr_2O_3	b.d.l.	b.d.l.	b.d.l.	b.d.l.
F	b.d.l.	b.d.l.	b.d.l.	0.14
Cl	b.d.l.	b.d.l.	b.d.l.	b.d.l.
Total	100.80	99.18	100.05	100.94
	Number of cations based on 4 oxygens			
Apfu				
Si	1.958	1.960	1.959	1.878
Ti	0.003	0.004	0.004	0.018
Al	0.028	0.029	0.034	0.171
Fe^{2+} all ferrous	0.654	0.621	0.609	0.234
Fe3+	0.082	0.074	0.064	0.141
Fe2+	0.572	0.547	0.544	0.094
Mn	0.033	0.027	0.026	0.006
Mg	1.315	1.316	1.354	0.898
Ca	0.031	0.064	0.032	0.802
Na	0.000	0.002	0.002	0.023
K	0.000	0.001	0.001	0.001
Cr	0.000	0.000	0.000	0.000
F	0.000	0.000	0.000	0.016
Cl	0.000	0.000	0.000	0.000
Mg#	67.10	67.94	68.99	79.30
Total	4.019	4.023	4.022	4.047

Note = Fe^{2+} and Fe^{3+} are recalculated based on the formula of Droop (1987).

Abbreviation: b.d.l. = below detection limit.

Table 2: Representative electron microprobe analyses of amphiboles from the TVC.

Sample	12AR020 AMPH 1-1	12AR020 AMPH 2-1	13AR014 AMPH 1-5-1	13AR014 AMPH 1-6-1	13AR014 AMPH 1-8-1	12AR017 AMPH 1-1-1	12AR017 AMPH 1-3-1	13AR012 AMPH 1-1-1 RIM	13AR012 AMPH 1-1-2 CORE
Rock Type	dacite	dacite	andesite	andesite	andesite	andesite	andesite	andesite	andesite
Age	Pl-P	LM	LM	LM	LM	LM	LM	Pl-P	Pl-P
SiO_2	43.84	45.03	44.98	42.65	43.45	41.18	41.39	44.06	43.00
TiO_2	1.88	1.79	1.72	2.23	2.51	3.19	3.50	2.57	2.19
Al_2O_3	9.55	9.26	8.52	7.34	11.94	13.49	13.49	10.38	13.50
Cr_2O_3	b.d.l.	b.d.l.	b.d.l.	b.d.l.	b.d.l.	b.d.l.	b.d.l.	b.d.l.	0.04
Fe_2O_3	7.29	7.54	8.14	22.13	6.22	6.26	6.18	6.40	6.17
FeO	8.08	7.82	5.68	0.00	7.85	6.45	4.10	8.53	3.44
FeO_T	14.63	14.60	13.00	19.91	13.44	12.08	9.66	14.29	9.00
MnO	0.44	0.43	0.31	0.31	0.26	0.13	0.11	0.23	0.11
MgO	12.85	13.31	14.33	13.73	13.14	13.62	15.17	13.41	15.55
CaO	11.18	11.34	11.10	9.01	11.52	11.59	11.57	11.35	11.80
Na_2O	1.81	1.64	1.69	1.25	2.15	2.41	2.51	2.46	2.35
K_2O	0.89	0.94	0.68	0.50	0.71	0.92	1.02	0.72	0.68
F	0.37	0.39	0.29	0.61	0.27	0.40	0.36	0.43	0.32
Cl	0.15	0.15	b.d.l.	b.d.l.	b.d.l.	b.d.l.	b.d.l.	b.d.l.	b.d.l.
Total	97.41	98.68	96.48	97.28	99.27	98.84	98.61	99.69	98.40
Si	6.453	6.525	6.584	6.187	6.243	5.948	5.932	6.337	6.117
Al^{iv}	1.547	1.475	1.416	1.255	1.757	2.052	2.068	1.663	1.883
Al^{vi}	0.111	0.106	0.054	0.000	0.265	0.244	0.210	0.097	0.380
Ti	0.209	0.196	0.189	0.243	0.271	0.346	0.377	0.278	0.235
Cr	b.d.l.	b.d.l.	b.d.l.	b.d.l.	b.d.l.	b.d.l.	b.d.l.	b.d.l.	0.005
Fe^{3+}	0.807	0.822	0.896	0.947	0.672	0.680	0.666	0.692	0.661
Fe^{2+}	0.994	0.947	0.696	1.550	0.943	0.779	0.491	1.026	0.410
Mn	0.055	0.053	0.039	0.038	0.032	0.016	0.013	0.028	0.013
Mg	2.820	2.876	3.126	2.970	2.814	2.933	3.241	2.876	3.298
Ca	1.763	1.761	1.740	1.401	1.772	1.794	1.777	1.749	1.798
Na	0.515	0.460	0.479	0.352	0.599	0.676	0.696	0.685	0.649
K	0.167	0.174	0.128	0.093	0.131	0.170	0.186	0.133	0.124
Ba	0.000	0.000	0.000	0.000	0.000	0.000	0.000	0.000	0.000
F	0.173	0.181	0.134	0.278	0.123	0.184	0.163	0.195	0.146
Cl	0.037	0.037	b.d.l.	b.d.l.	b.d.l.	b.d.l.	b.d.l.	b.d.l.	b.d.l.
OH*	1.790	1.782	1.866	1.722	1.877	1.816	1.837	1.805	1.855
$(Na+K)_A$	0.445	0.519	0.483	0.277	0.655	0.749	0.813	0.725	0.677
Mg#	0.739	0.752	0.818	0.657	0.749	0.790	0.868	0.737	0.890
Al^T	1.657	1.582	1.470	1.255	2.022	2.296	2.278	1.760	2.263
Total	17.442	17.394	17.348	16.957	17.505	17.642	17.660	17.570	17.571

Table 2: Continued

Sample	13AR017 AMPH 1-3-1	13AR017 AMPH 1-4-1	13AR016 AMPH 1-1-1	13AR016 AMPH 1-3-3	13AR007 AMPH 1-1-1	13AR007 AMPH 1-3-3	13AR010 AMPH 1-4-1	13AR010 AMPH 1-5-1
Rock Type	andesite	andesite	andesite	andesite	dacite	dacite	andesite	andesite
Age	Pl-P	Pl-P	Pl-P	Pl-P	Pl-P	Pl-P	Pl-P	Pl-P
SiO_2	46.05	44.88	46.44	44.37	46.68	42.17	46.69	43.23
TiO_2	1.79	1.91	1.86	1.69	1.51	2.21	1.57	2.10
Al_2O_3	8.78	9.32	8.32	10.12	7.82	12.28	8.11	12.11
Cr_2O_3	b.d.l.	b.d.l.	b.d.l.	b.d.l.	b.d.l.	b.d.l.	b.d.l.	b.d.l.
Fe_2O_3	8.54	7.88	7.38	7.16	6.55	6.39	8.59	7.71
FeO	5.24	6.02	5.55	8.50	7.86	8.17	4.65	5.51
FeO_T	12.92	13.11	12.19	14.94	13.75	13.92	12.38	12.45
MnO	0.31	0.27	0.24	0.45	0.44	0.20	0.30	0.23
MgO	14.82	14.29	15.27	12.80	14.14	12.82	15.27	14.03
CaO	11.34	11.40	11.56	11.44	11.71	11.84	11.35	11.67
Na_2O	1.60	1.64	1.58	1.77	1.35	1.93	1.47	1.95
K_2O	0.69	0.77	0.65	0.94	0.74	0.96	0.59	0.72
F	0.31	0.29	0.34	0.19	0.33	0.25	0.32	0.35
Cl	0.12	0.11	b.d.l.	0.13	b.d.l.	b.d.l.	b.d.l.	b.d.l.
Total	98.58	97.85	98.29	98.74	98.32	98.46	97.90	98.66
Si	6.585	6.497	6.647	6.441	6.744	6.143	6.685	6.201
Al^{iv}	1.415	1.503	1.353	1.559	1.256	1.857	1.315	1.799
Al^{vi}	0.064	0.087	0.051	0.174	0.075	0.250	0.053	0.248
Ti	0.192	0.208	0.200	0.185	0.164	0.242	0.169	0.226
Cr	b.d.l.	b.d.l.	b.d.l.	b.d.l.	b.d.l.	b.d.l.	b.d.l.	b.d.l.
Fe^{3+}	0.919	0.858	0.795	0.782	0.712	0.701	0.926	0.833
Fe^{2+}	0.626	0.728	0.664	1.032	0.950	0.995	0.557	0.661
Mn	0.038	0.033	0.030	0.055	0.054	0.025	0.037	0.028
Mg	3.160	3.083	3.258	2.771	3.044	2.784	3.258	3.001
Ca	1.738	1.768	1.773	1.779	1.813	1.848	1.741	1.794
Na	0.445	0.461	0.439	0.498	0.377	0.545	0.408	0.543
K	0.126	0.141	0.119	0.174	0.137	0.178	0.108	0.133
Ba	0.000	0.000	0.000	0.000	0.000	0.000	0.000	0.000
F	0.141	0.135	0.152	0.086	0.151	0.116	0.144	0.157
Cl	0.028	0.028	0.000	0.032	0.000	0.000	0.000	0.000
OH*	1.831	1.837	1.848	1.882	1.849	1.883	1.856	1.843
(Na+K)	0.445	0.492	0.449	0.568	0.424	0.651	0.391	0.577
Mg#	0.835	0.809	0.831	0.729	0.762	0.737	0.854	0.819
Al^T	1.479	1.590	1.404	1.732	1.331	2.107	1.368	2.047
Total	17.309	17.371	17.328	17.450	17.327	17.566	17.257	17.466

9.1.1. Major Elements

All volcanic rock samples collected from Taftan are intermediate to felsic in composition with SiO_2 contents ranging from from 57 wt.% to 69 wt.% (average = 61 ± 3 wt.%, n = 17). All samples are subalkaline and plot in the calc-alkaline to high-K calc-alkaline fields (Fig. 16b). Temporally, compositions shift from high-K calc-alkaline to calc-alkaline from the late Miocene to the Plio-Pleistocene. According to the aluminum saturation index (ASI = Al/(Ca+Na+K); Maniar and Piccoli, 1989; Frost et al., 2001), the Taftan samples are metaluminous with ASI ratios ranging from 0.66 to 0.94 (average = 0.84 ± 0.08, n = 17), and increase from the late Miocene to the Plio-Pleistocene (Fig. 16c). The chemical variations of major and minor elements Al_2O_3, MgO, Fe_2O_{3T}, TiO_2, Na_2O, K_2O, and P_2O_5 relative to SiO_2 are shown in Fig. 17. Most elements show fairly coherent inverse trends relative to SiO_2 as expected for fractionation of ferromagnesian minerals such as pyroxene, amphibole, and titanite, whereas, Al_2O_3, Na_2O, and K_2O tend to increase with SiO_2.

The Mg# (MgO/MgO+FeO) of the nine Taftan samples for which [FeO] was measured separately by titration is relatively low and ranges from 0.41 to 0.52 with an average of 0.47 ± 0.03.

9.1.2. Trace elements

Primitive mantle-normalized trace element and chondrite-normalized rare earth element diagrams for samples of the TVC are shown in Fig. 18 (normalization values from Sun and McDonough, 1989).

Andesitic-dacitic samples from the TVC show relative depletions of Nb, Ta, and Ti and enrichment of Pb, which are characteristic signatures of continental volcanic arc rocks (Gill, 1981; Pearce and Peate, 1995, Fig. 18a). The elevated Pb peak is likely related to subducted sediments. Furthermore, depletion of Ti and P in most of dacitic rocks can be attributed to fractionation of magnetite, amphibole and apatite. Incompatible elements such as Rb, Ba, Th,

and U are also enriched in the TVC rocks, which can reflect a combination of source enrichement and fractionation processes (see discussion).

The samples show moderate enrichments of light rare earth elements (LREE) relative to middle and heavy rare earth elements (MREE and HREE) with listric-shaped patterns (Fig. 18b). Such patterns reflect amphibole crystallization (Munterer and Ulmer, 2006). The samples from the late Miocene, however, are more enriched in LREE (La/Yb < 30) than the Plio-Pleistocene rocks (La/Yb < 20; See Table 3). All volcanic rocks present weakly negative Eu anomalies (as expressed by $Eu_n / Eu^* = Eu_n / \sqrt{Sm_n \times Gd_n}$) suggesting minor plagioclase fractionation or relatively oxidized magmas (Frey et al., 1979; Hanson, 1980), and are plotted against SiO_2 in Fig. 19.

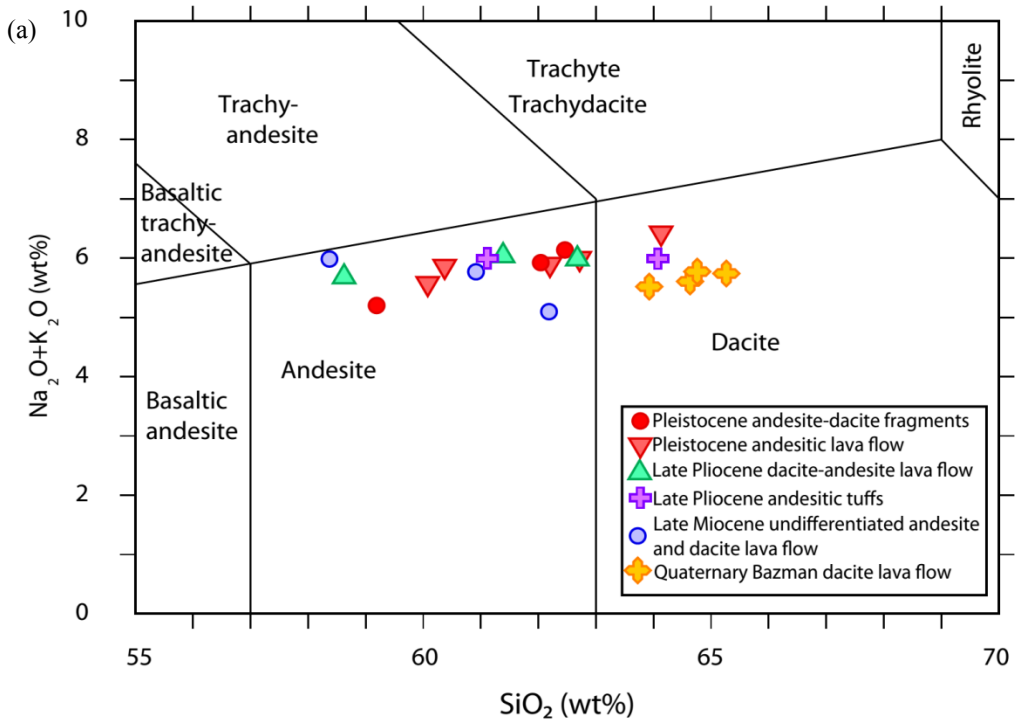

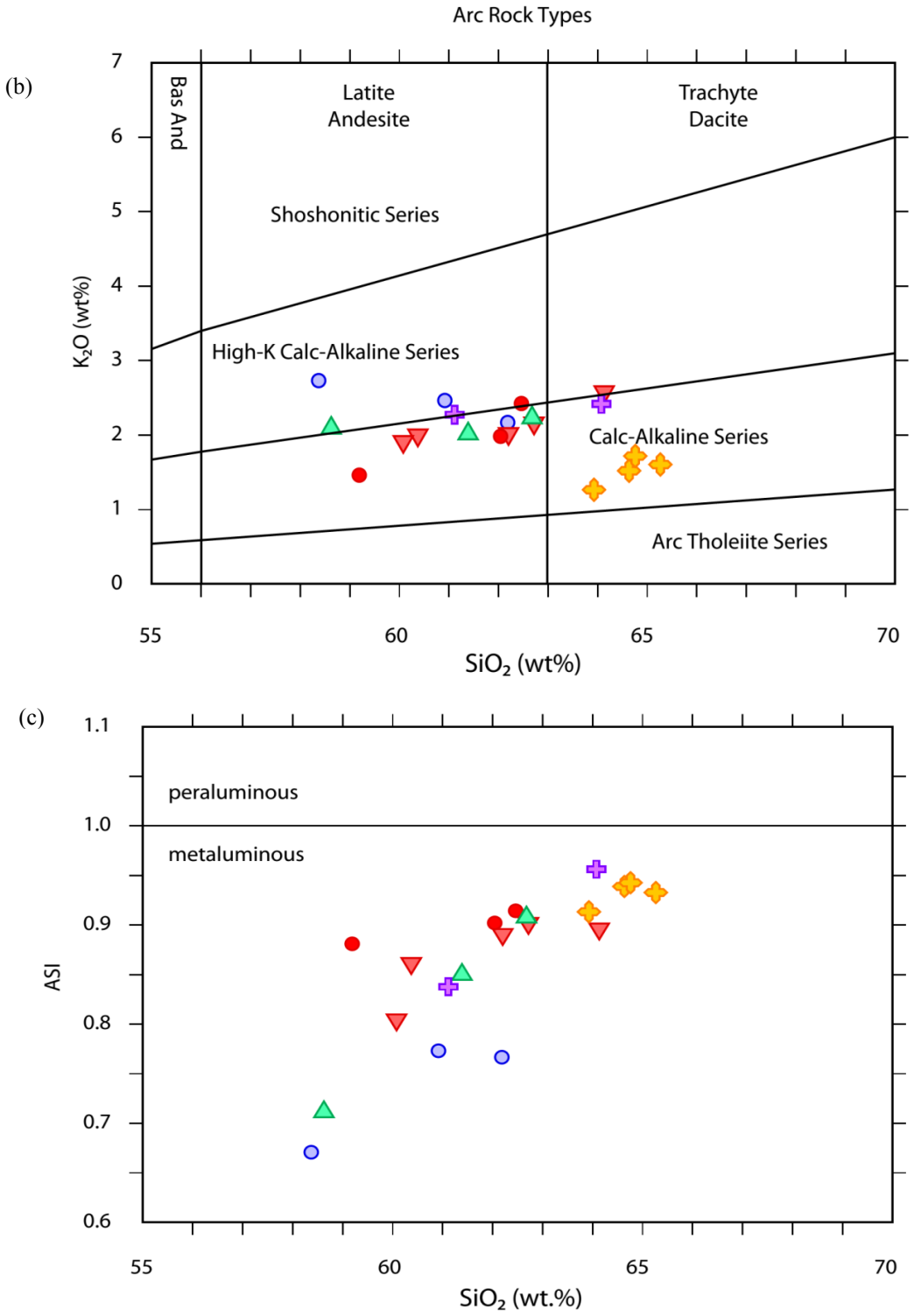

Fig. 16: Geochemical classification of the TVC: (a) Total alkali versus silica diagram (IUGS rock classification from Le Maitre, 1989); (b) K_2O vs SiO_2 (Peccerillo and Tylor, 1976); (c) ASI vs SiO_2 (Maniar and Piccoli, 1989).

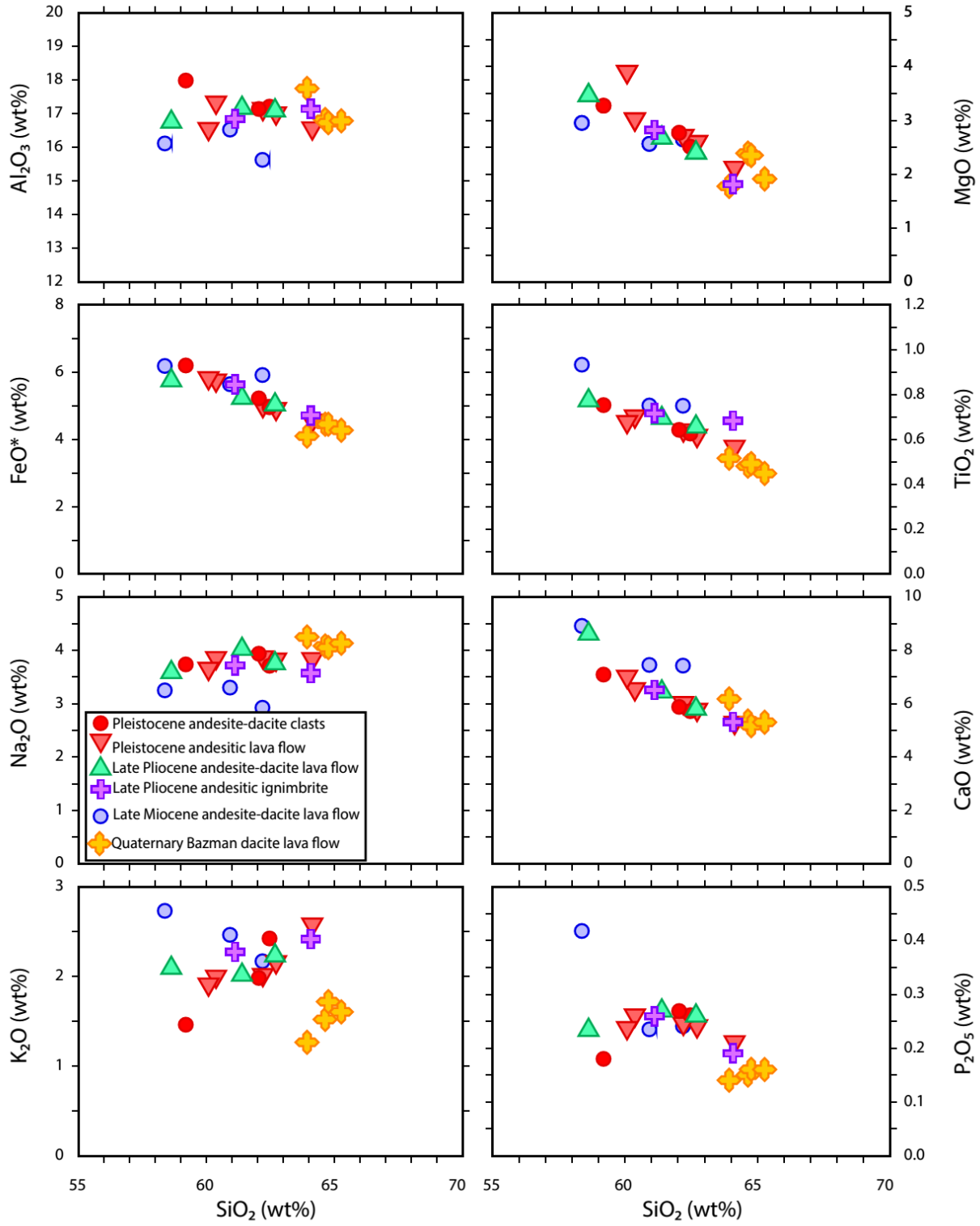

Fig. 17: Harker diagrams for major and minor element constituents of the TVC.

Table 3: Major and trace elements analyses of volcanic rocks from the TVC.

Samples	**12A011**	**12A013**	**12A014**	**12A017**	**12A018**	**12A019**	**12A020**	**13A003**	**13A005**	**13A007**	**13A010**	**13A012**	**13A018**	**13A019**	**13A021**	**13A023**	**13A024**
Rock type (TAS)	dacite	andesite	andesite	andesite	**andesite**	**andesite**	dacite	andesite	andesite	dacite	andesite	andesite	andesite	andesit	andesite	andesite	andesite
	High-K	Med.-K	High-K	Med.-K	Med.-K	Med.-K	Med.-K	Med.-K	Med.-K	Med.-K	Med.-K	Med.-K	Med.-K	Med.-K	Med.-K	Med.-K	Med.-K
Weight %																	
SiO_2	66.13	59.54	56.72	57.24	62.33	60.01	63.56	60.55	60.63	63.87	62.07	62.63	62.2	61.5	59.05	61.27	57.69
Al2O_3	14.67	16.16	14.26	15.81	16.92	17.24	16.43	16.69	16.72	17.09	17.11	17.08	17.19	17.2	17.95	16.89	16.49
Fe_2O_3*	2.9	5.52	5.4	6.07	4.89	5.73	4.53	5.88	4.88	4.7	4.93	5.03	5.24	5.24	6.19	5.65	5.66
Fe_2O_3	NA	3.29	NA	3.07	1.22	NA	1.87	NA	NA	3.7	2.7	NA	NA	1.35	2.4	NA	5.1
FeO[(1)]	NA	2.00	NA	2.70	3.30	NA	2.40	NA	NA	0.90	2.00	NA	NA	3.50	3.40	NA	0.50
MnO	0.061	0.117	0.079	0.099	0.091	0.101	0.085	0.102	0.089	0.069	0.092	0.09	0.092	0.09	0.103	0.097	0.096
MgO	1.08	2.51	2.42	2.9	2.59	3.01	2.11	3.94	2.65	1.81	2.5	2.4	2.78	2.68	3.27	2.83	3.41
CaO	3.53	7.29	6.78	8.75	5.75	6.52	5.25	7.08	5.89	5.3	5.69	5.8	5.9	6.46	7.08	6.53	8.48
Na_2O	3.18	3.23	2.67	3.19	3.81	3.84	3.81	3.69	3.78	3.56	3.69	3.75	3.95	4.03	3.73	3.73	3.53
K_2O	3.64	2.41	1.98	2.68	2.15	1.99	2.56	1.93	1.97	2.41	2.41	2.23	1.99	2.02	1.46	2.28	2.06
TiO_2	0.339	0.735	0.685	0.916	0.614	0.7	0.564	0.685	0.626	0.681	0.623	0.656	0.645	0.696	0.752	0.719	0.761
P_2O_5	0.11	0.23	0.22	0.41	0.24	0.26	0.21	0.24	0.24	0.19	0.26	0.26	0.27	0.27	0.18	0.26	0.23
S	0.024	0.029	0.04	0.043	0.02	0.041	0.025	0.026	0.027	0.022	0.026	0.024	0.032	0.028	0.031	0.029	0.046
LOI	3.88	3.11	8.71	2.46	0.94	0.39	1.57	0.12	1.46	1.28	1.44	0.32	0.58	0.5	0.37	0.25	2.43
Total	99.53	100.9	99.92	100.5	100.3	99.79	100.7	100.9	98.95	101	100.8	100.2	100.8	100.7	100.1	100.5	100.8

Table 3 Continued:

Samples	**12A011**	**12A013**	**12A014**	**12A017**	**12A018**	**12A019**	**12A020**	**13A003**	**13A005**	**13A007**	**13A010**	**13A012**	**13A018**	**13A019**	**13A021**	**13A023**	**13A024**
Rock type (TAS)	dacite	andesite	andesite	andesite	**andesite**	**andesite**	dacite	andesite	andesite	dacite	andesite	andesite	andesite	andesit	andesite	andesite	andesite
	High-K	Med.-K	High-K	Med.-K	Med.-K	Med.-K	Med.-K	Med.-K	Med.-K	Med.-K	Med.-K	Med.-K	Med.-K	Med.-K	Med.-K	Med.-K	Med.-K
ppm																	
As	2	b.d.l.	2	1	1	3	3	b.d.l.	b.d.l.	b.d.l.	b.d.l.	2	b.d.l.	b.d.l.	b.d.l.	2	b.d.l.
Ba	535	507	347	578	425	404	512	366	389	512	468	478	434	480	342	448	436
Be	2	2	2	2	2	2	2	2	2	2	2	2	2	2	2	2	2
Co	4.9	15.6	14.8	17.2	12.9	15.2	10.3	16.9	11.3	14.2	11.1	11.1	12	13.5	15.5	15.1	15.6
Cr	16.1	50.5	63.4	67.9	32.8	21.7	21.9	59.8	28	16.6	39.9	31.5	31.8	27.8	17	40.2	50.4
Cs	50.8	10.3	15.6	4.6	4.1	3.7	5.1	2.6	4	2.6	4.4	3	2	2	1.2	3.9	3.6
Cu	9	16	9	17	13	15	10	28	13	10	18	10	14	14	13	14	19
Ga	18	20	18	20	20	20	20	20	21	19	20	22	20	21	21	20	20
Ge	1.5	1.7	1.6	1.7	1.6	1.5	1.7	1.7	1.5	1.4	1.6	1.8	1.6	1.5	1.7	1.6	1.6
Hf	3.1	3.2	2.9	3.9	3.5	3.3	3.5	3.2	3	3.4	3.4	3.8	3.4	3.5	2.8	3.4	3.2
Nb	14.3	14.6	13	17.3	10.7	10.3	12.7	9.3	10.4	9.3	11.1	13.8	11	10.5	7.8	11.2	10.2
Ni	8	19	21	21	20	17	14	26	21	11	22	17	36	28	14	16	15
Pb	35	11	10	8	10	9	15	9	7	8	13	12	14	9	b.d.l.	9	10
Rb	177	97	83	81	84	74	102	70	76	68	88	84	73	68	39	85	72
Sb	1.8	0.4	b.d.l.	b.d.l.	b.d.l.	b.d.l.	0.2	b.d.l.	0.1	b.d.l.	b.d.l.	b.d.l.	b.d.l.	b.d.l.	b.d.l.	b.d.l.	b.d.l.
Sc	4.94	12.3	12.6	13.8	9.66	11.9	7.69	16	9.6	8.85	9.22	10.2	9.68	9.89	14.3	13.8	15.6
Sr	305	607	279	813	617	869	607	808	738	734	668	703	681	710	716	757	830
Ta	1.28	1.1	0.92	1.19	0.8	0.74	1.05	0.66	0.75	0.66	0.85	0.99	0.99	0.84	0.5	0.97	0.75
Th	22.6	15.1	13.2	14.8	12.5	11.1	15.1	10	10.7	9.6	12.4	12.3	10.6	10.1	5.64	12.5	11.6
U	5.18	3.55	2.93	3.27	2.82	2.61	3.27	2.37	2.42	2.11	2.77	2.62	2.56	2.27	1.17	2.97	2.85
V	45	118	105	150	91	122	78	130	95	93	91	86	99	99	123	174	140
Y	11	16	14	16	15	15	15	15	15	16	16	17	16	15	18	16	15
Zn	175	68	69	71	69	68	65	70	66	78	63	77	78	72	67	68	74
Zr	119	142	127	158	151	134	145	128	130	154	145	149	147	147	109	143	128

Table 3 Continued:

Samples	**12A011**	**12A013**	**12A014**	**12A017**	**12A018**	**12A019**	**12A020**	**13A003**	**13A005**	**13A007**	**13A010**	**13A012**	**13A018**	**13A019**	**13A021**	**13A023**	**13A024**
Rock type (TAS)	dacite	andesite	andesite	andesite	**andesite**	**andesite**	dacite	andesite	andesite	dacite	andesite	andesite	andesite	andesit	andesite	andesite	andesite
	High-K	Med.-K	High-K	Med.-K	Med.-K	Med.-K	Med.-K	Med.-K	Med.-K	Med.-K	Med.-K	Med.-K	Med.-K	Med.-K	Med.-K	Med.-K	Med.-K
ppm																	
La	33.7	36	31.8	44.6	29.9	30.1	34.8	27.2	28.5	26.9	31.1	34.2	32.3	29.9	18.6	32.6	32.4
Ce	61	65.9	58.7	85.5	56.9	59.1	64.4	53.8	54.3	51.4	59.8	65.4	59.4	57.7	39.4	62.5	62.6
Pr	6.19	7.13	6.26	9.6	6.35	6.66	7.07	6.19	6.13	5.79	6.71	7.36	6.78	6.42	4.59	7.12	6.99
Nd	20.9	25.5	22.3	34.7	23.1	24.3	25.1	23.4	22.2	21	23.9	26.8	24.7	23.7	17.7	25.9	25.7
Sm	3.4	4.48	3.89	5.88	4.21	4.34	4.33	4.2	3.98	3.92	4.14	4.75	4.34	4.43	3.76	4.7	4.46
Eu	0.701	1.07	1	1.42	1.12	1.12	1.04	1.11	1.04	1.04	1.04	1.14	1.17	1.11	1.05	1.14	1.07
Gd	2.26	3.35	2.96	4.03	3.05	3.23	3.22	3.15	3	3.07	2.97	3.6	3.24	3.3	3.25	3.37	3.34
Tb	0.33	0.51	0.46	0.57	0.5	0.52	0.48	0.49	0.48	0.45	0.47	0.54	0.5	0.5	0.54	0.52	0.5
Dy	1.88	2.89	2.64	3.11	2.8	2.75	2.73	2.78	2.57	2.54	2.72	3.05	2.69	2.7	3.33	2.89	2.84
Ho	0.37	0.54	0.49	0.57	0.53	0.53	0.53	0.55	0.5	0.5	0.52	0.59	0.52	0.49	0.65	0.56	0.53
Er	1.14	1.42	1.38	1.58	1.54	1.58	1.46	1.59	1.44	1.44	1.51	1.67	1.45	1.39	1.91	1.55	1.53
Tl	1.69	0.39	1.05	0.39	0.36	0.6	0.49	0.25	0.36	0.14	0.43	0.24	0.3	0.25	0.12	0.26	0.37
Tm	0.181	0.237	0.214	0.224	0.238	0.227	0.233	0.241	0.225	0.21	0.238	0.261	0.229	0.214	0.298	0.237	0.236
Yb	1.18	1.48	1.39	1.45	1.53	1.53	1.53	1.56	1.44	1.29	1.5	1.7	1.56	1.43	1.95	1.51	1.47
Lu	0.172	0.231	0.21	0.223	0.226	0.236	0.224	0.226	0.227	0.204	0.22	0.25	0.241	0.205	0.303	0.224	0.217
Mg#[(2)]	-	0.45	-	0.46	0.49	-	0.44	-	-	0.41	0.47	-	-	0.48	0.48	-	0.52
La/Sm	9.91	8.04	8.17	7.59	6.99	6.15	7.05	6.48	7.16	6.86	7.51	7.20	7.44	6.75	4.95	6.94	7.26
Sm/Yb	2.88	3.03	2.80	4.06	2.01	1.72	2.32	2.69	2.76	3.04	2.76	2.79	2.78	3.10	1.93	3.11	3.03
La/Yb	28.56	24.32	22.88	30.76	14.03	10.59	16.37	17.44	19.79	20.85	20.73	20.12	20.71	20.91	9.54	21.59	22.04

*Total Fe reported as Fe_2O_3.
(1) FeO content measured by titration.
(2) Mg# = (MgO/(MgO + FeO)).
Abbreviations: b.d.l. = Below detection limit; NA = not analyzed.

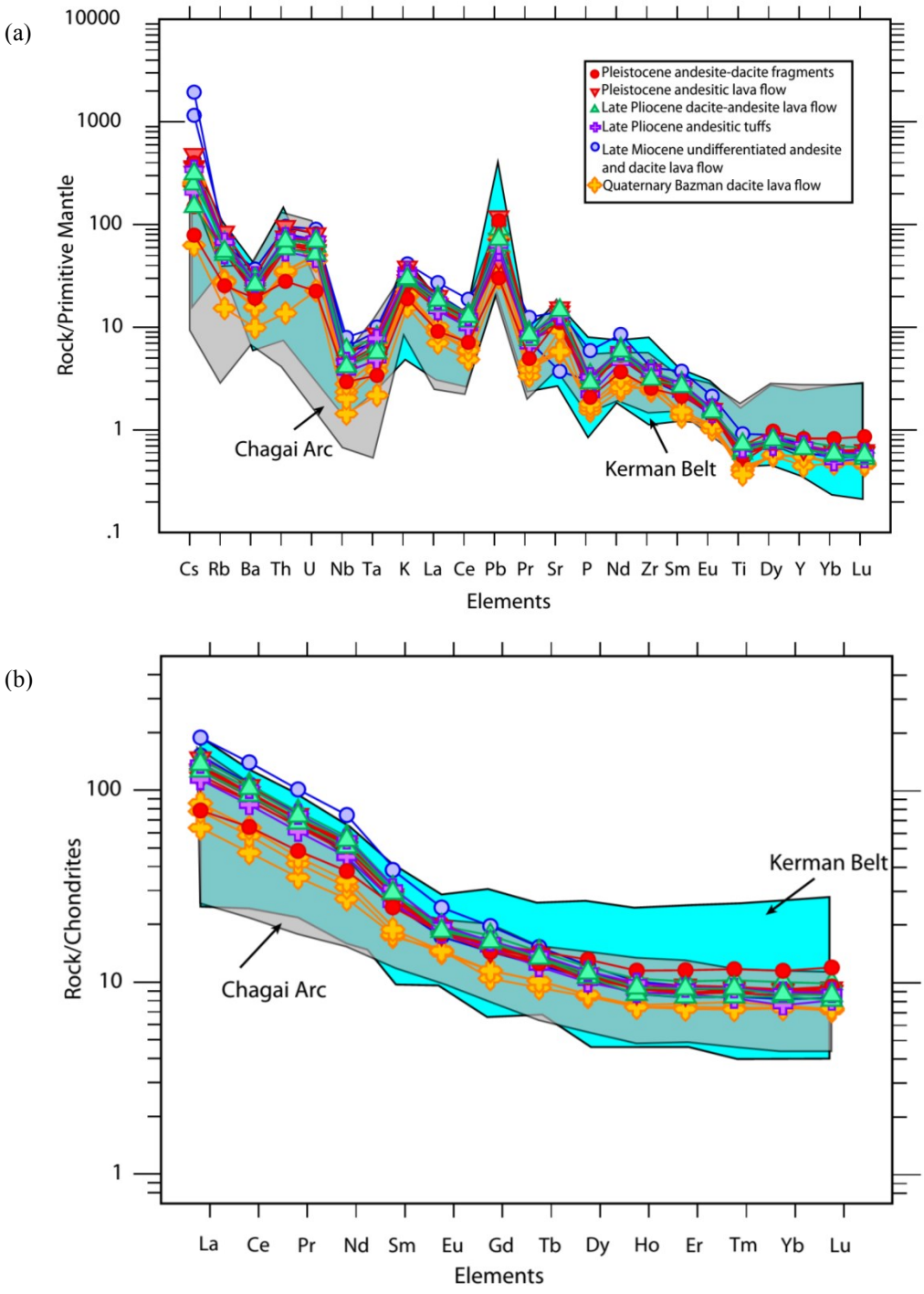

Fig. 18: Plots of trace element and REE data for the TVC: (a) plot of trace elements and REE normalized to primitive mantle composition of Sun and McDonough (1989); (b) Plot of REE normalized to C1 chondrite composition of Sun and McDonough (1989). Background data for the Chagai Arc in Pakistan from Siddiqui (2004), Nickolson et al. (2010), and Richards et al. (2012); Kerman Belt from Shafiei et al. (2009).

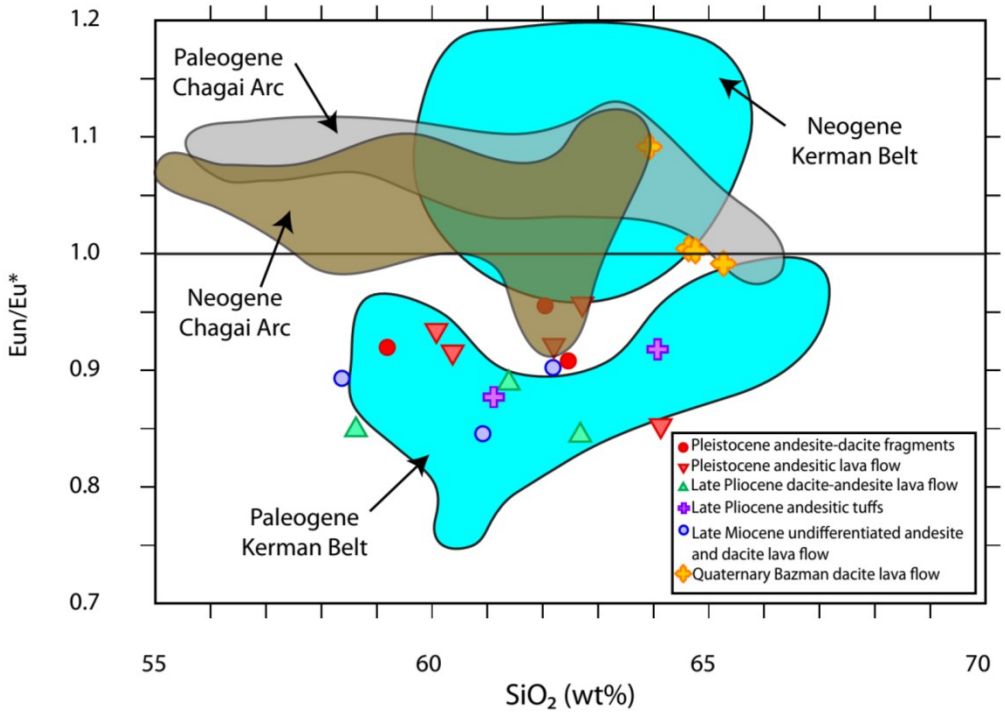

Fig. 19: Plot of Eu/Eu* versus SiO_2 for samples of the TVC. Background data for Chagai Arc from Siddiqui (2004), Nickolson et al. (2010), and Richards et al. (2012); Kerman Belt from Shafiei et al. (2009).

10. Estimates of temperature, pressure, and redox conditions

Analyses of coexisting magnetite-ilmenite mineral pairs, amphibole, and whole rock Fe^{3+}/Fe^{2+} ratios are here used to provide constraints on pressure, temperature, redox state, and primary composition of evolving magmas, based on the equilibrium equations of Andersen and Lindsley (1985), Rhodes and Vollinger (2005), Ridolfi et al. (2010), and Ridolfi and Renzulli (2012).

10.1. Magnetite-ilmenite pairs

The results of magnetite-ilmenite thermometry for four samples of andesite from the late Miocene to the Plio-Pleistocene are summarized in Table 4. The ILMAT Excel spreadsheet (Lepage, 2003) was used to estimate temperature and oxygen fugacity (fO_2). The uncertainty for temperature and fO_2 are estimated to be at best ±35°C and ±0.2 log fO_2 unit (Spencer and Lindsley, 1981). Samples were carefully studied by petrographic microscope and selected for

analysis to avoid oxidation of magnetite (to hematite) or exsolution. The grain pairs used for calculation had Mg/Mn ratios consistent with equilibrium between melt and minerals, as defined by Bacon and Hirschmann (1988). Eight representative magnetite-ilmenite pairs from three andesitic rocks yielded temperatures from ~710°C to ~950°C (average = 810°C ± 90°C, n = 10), and redox states (relative to the fayalite-magnetite-quartz buffer, ΔFMQ) ranging from +0.4 to +2.0 (average = +1.6 ± 0.6, n = 10). The results show no significant redox changes from the late Miocene to the Plio-Pleistocene. No suitable equilibrated magnetite-ilmenite pairs were found in dacitic rock samples.

10.2. Amphibole

The crystallization temperature, pressure, and oxygen fugacity (fO_2) during crystallization of amphibole phenocrysts were estimated from electron microprobe analyses of amphiboles from eight samples of andesitic and dacitic rocks using the method of Ridolfi et al. (2010; Table 4). This thermobarometer is valid for temperatures between 550°–1120°C and pressures below 1200 MPa. The uncertainty for temperature, pressure, and fO_2 are estimated to be at best ± 23°C, P ± 11.5%, and ±0.4 log fO_2 unit (Ridolfi and Renzulli, 2012).

The crystallization temperatures of amphiboles from late Miocene andesites range from ~890°C to ~1020°C ((average = 1010 ± 22°C, n = 7), and calculated pressures vary from ~460 to ~600 MPa (average = 505 ± 56 MPa, n = 7), equivalent to depths of 17–22 km (average = 19 ± 2 km). The oxidation state (ΔFMQ) for the late Miocene andesite samples range from +1.1 to +1.5 (average = +1.2 ± 0.1, n = 7).

The crystallization temperatures of amphiboles from the Plio-Pleistocene andesites range from ~830°C to ~1000°C (average = 910 ± 22°C, n = 45), whereas Plio-Pleistocene dacite samples vary from ~830°C to ~900°C (average = 860 ± 22°C, n = 17). The calculated pressures for amphiboles form the Plio-Pleistocene andesites vary from ~130 to ~620 MPa (average = 303 ± 34 MPa, n = 45), equivalent to depths of 5–23 km (average = 11 ± 2 km), whereas the pressures for amphiboles from the Plio-Pleistocene dacites vary from ~110 to ~210 MPa (average = 161 ± 18 MPa, n = 17), equivalent to depths of 4–8 km (average = 6 ± 1 km). The oxidation state (ΔFMQ) for the Plio-Pleistocene andesite samples ranges from

+1.3 to +2.3 (average = +1.8 ± 0.3, n = 17), whereas dacite samples vary from +1.5 to +2.3 (average = +1.8 ± 0.3, n = 17).

Table 4: Representative pressure, temperature, and redox conditions of the TVC from amphibole chemistry.

Sample	12AR020 AMPH 1-1	12AR020 AMPH 2-1	12AR014 AMPH 1-5-1	12AR014 AMPH 2-6-1	12AR014 AMPH 1-8-1	12AR014 AMPH 1-1-1	12AR017 AMPH 1-3-1	13AR012 AMPH 1-1-1 RIM	13AR012 AMPH 1-1-2 CORE
Rock Type	**dacite**	**dacite**	**andesite**	**andesite**	**andesite**	**andesite**	**andesite**	**andesite**	**andesite**
Age	**Pl-P**	**LM**	**LM**	**LM**	**LM**	**LM**	**LM**	**Pl-P**	**Pl-P**
T (°C)	883	869	860	985	940	1005	1019	913	993
P (MPa)	208	187	159	422	352	522	508	242	497
Upper crust depth (km)	7.9	7.1	6.0	15.9	13.3	19.7	19.2	9.1	18.8
H_2O_{melt} (wt.%)	4.8	4.6	4.4	6.1	6.3	5.8	4.9	4.7	6.6
ΔFMQ	+1.5	+1.7	+2.0	+2.1	+1.2	+1.2	+1.5	+1.3	+1.9
Sample	**13AR017 AMPH 1-3-1**	**13AR017 AMPH 1-4-1**	**13AR016 AMPH 1-1-1**	**13AR016 AMPH 1-3-3**	**13AR007 AMPH 1-1-1**	**13AR007 AMPH 1-3-3**	**13AR010 AMPH 1-4-1**	**13AR010 AMPH 1-5-1**	
Rock Type	**dacite**	**dacite**	**andesite**	**andesite**	**andesite**	**andesite**	**andesite**	**andesite**	**andesite**
Age	**Pl-P**	**LM**	**LM**	**LM**	**LM**	**LM**	**LM**	**Pl-P**	**Pl-P**
T (°C)	861	880	856	889	834	959	843	949	
P (MPa)	161	189	145	232	130	398	137	365	
continental depth (km)	6.1	7.1	5.5	8.8	4.9	15.0	5.2	13.8	
H_2O_{melt} (wt.%)	4.5	4.7	4.3	5.2	4.5	6.1	4.5	6.3	
ΔFMQ	+2.1	+1.9	+2.2	+1.5	+1.9	+1.3	+2.3	+1.7	

Notes: depths were calculated based on upper crustal density of 2.7 g/cm^3.

Abbreviations: Pl-P= Plio-Plesitocene, LM = Late Miocene

10.3. Whole rock Fe^{3+}/Fe^{2+} ratios

The whole rock ferric/ferrous ratio can be used to estimate the redox state of the original magma (Blevin, 2004; Rhodes and Vollinger, 2005). The FeO contents of of nine fresh samples of volcanic rock from the Taftan volcanic complex were analyzed by titration, and Fe^{3+}/Fe^{2+} ratios were then calculated from the $Fe_2O_{3[total]}$. Values of log (Fe_2O_3/FeO) against FeO* (total iron reported as FeO) are plotted in Figure 20. The Fe^{3+}/Fe^{2+} ratios range from 0.4 to 1.7 (average = 0.9 ± 0.5, n = 9), and show 'moderately oxidized' to 'strongly oxidized'

compositions above the FMQ buffer, consistent with results of fO_2 estimates from amphibole and magnetite-ilmenite pairs.

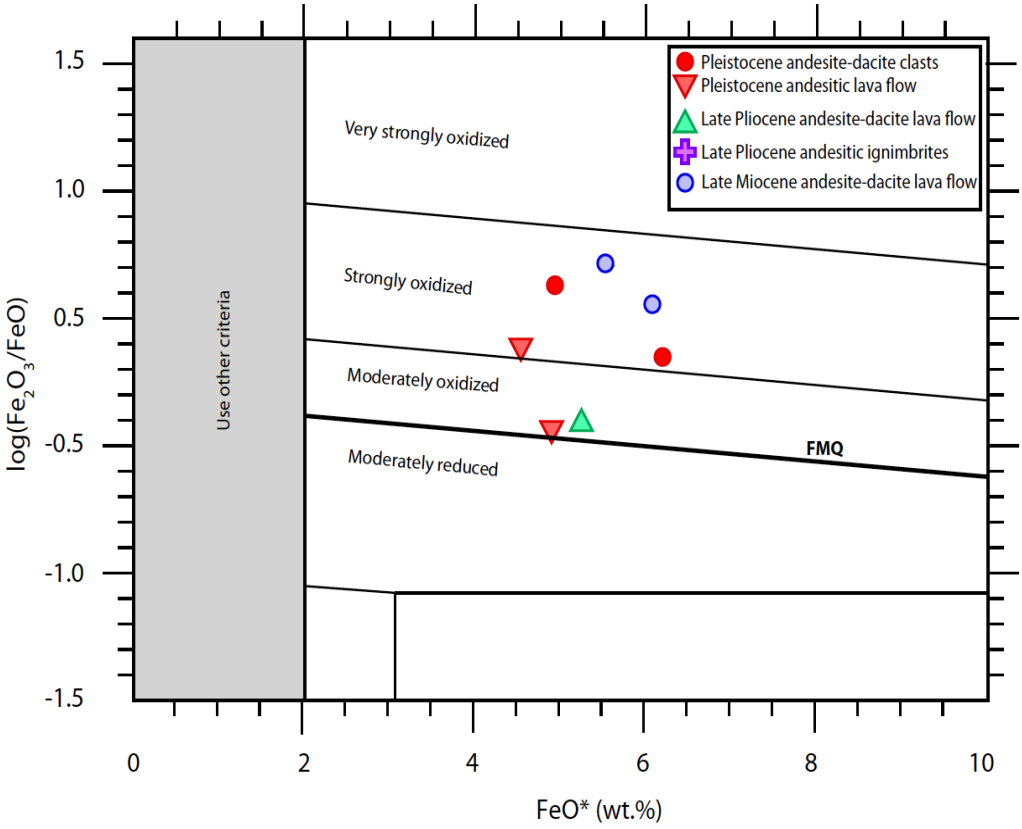

Fig. 20: Whole rock log(Fe_2O_3/FeO) versus FeO* values for selected samples of the TVC (after Blevin, 2004).

11. Discussion

11.1. TVC Magma Evolution

Magma source processes can be reconstructed from primitive mafic magmas, but they can be hard to reconstruct for intermediate to felsic magmas due to mineral fractionation and contamination process that likely occur during magma ascent through the upper crust (Davidson, 1996; Davidson et al., 2005). The TVC magmas show LILE enrichment as well as Ta, Nb, and Ti depletions, which are characteristic signatures of subduction-related arc magmas. Additionally, $^{143}Nd/^{144}Nd$ and $^{87}Sr/^{86}Sr$ isotopic ratios of the Taftan volcanic rocks (data from Pang et al., 2014) indicate evolution of the TVC from arc-related magma, with some degree of crustal involvement (see below).

Quantitative assessment of crustal magmatic processes in the TVC volcanic suites is constrained using major element trends and variations of trace element ratios such as La/Yb and Sr/Y vs. time, La/Sm vs. Sm/Yb, and Sr vs. Yb (Figs. 21 and 22).

On Harker diagrams, depletion of MgO, CaO, FeO (as total iron), and TiO_2 versus SiO_2 (Fig. 17) suggest fractionation of ferro-magnesian mineral phases such as pyroxene and amphibole, and Fe-Ti oxides such as magnetite. Al_2O_3 shows a roughly flat trend, suggesting that an expected increase due to pyroxene and amphibole fractionation is balanced by fractionation of plagioclase, as also suggested by decreasing CaO contents with SiO_2. Alkalis (Na_2O and K_2O increase slightly with SiO_2 (but with some scatter, especially for K_2O) which is consistent with late fractionation of alkali-rich minerals such as albitic plagioclase, biotite, or K-feldpar (not observed as a phenocryst phase in these rocks). Similar compositional relationships and trends are observed for all of the late Miocene to Quaternary rocks, although they do not represent a strictly comagmnatic suite.

La/Yb and Sr/Y ratios of the TVC are relatively high compared to normal island arc magmas (Fig. 21; Defant and Drummond, 1990). La/Yb ratios decrease slightly from the late Miocene to the Plio-Pleistocene, whereas Sr/Y ratios show no clear trend with time.

On a plot of Sr versus SiO_2 (Fig. 22a), Sr decreases with increasing SiO_2, which is consistent with the decrease of CaO with SiO_2 indicating plagioclase fractionation. The fractionation of plagioclase is likely delayed relative to ferromagnesian minerals due to high magmatic water contents (Frey et al., 1978; Hanson, 1980) as is evident from the hydrous nature of the TVC magmas (>5 wt.% H_2O) indicated by the compositions of amphiboles. The lack of significant Eu anomalies (Eu_n/Eu^*, average = 0.89 ± 0.05, n = 17; Fig. 18) cannot therefore indicate minimal plagioclase fractionation. Instead, it is likely due to high magmatic oxidation states that caused Eu to be in Eu^{3+} state rather than Eu^{2+} state, which is not partitioned into plagioclase (Henderson, 1984).

11.2. Comparison of TVC with the Bazman Volcano

Four samples of dacitic lavas from the Bazman volcano, 150 km to the southwest of Taftan, show broadly similar geochemical characteristics, and fall on an extension of the TVC trend to higher SiO_2 contents (up to 66 wt.%) on Harker diagrams (Figs. 16 and 17).

The only exception is K_2O, which is lower in the Bazman samples. The Bazman samples are metaluminous and calc-alkaline, similar to the TVC, but with lower K_2O. The Mg# (MgO/(MgO + FeO)) of one sample for which [FeO] was measured separately by titration is similar to the TVC (Mg# = 0.51).

Primitive mantle-normalized trace element and chondrite-normalized rare earth element patterns for samples from Bazman are very similar to the TVC and show moderate enrichments of incompatible trace elements and REEs (Fig. 18), but LREE relative to MREE and HREE is less enriched in the Bazman samples (La/Yb ratios<16). The Bazman samples lack a Eu anomaly (as expressed by $Eu_n / Eu^* = Eu_n / \sqrt{Sm_n \times Gd_n}$; Fig 19) suggesting these lavas were either more oxidized or more water-rich than the TVC magmas.

11.3. Comparison of TVC with the Kerman and Chagai Belts

Shafiei et al. (2009) reported geochemical data set for both barren pre-collisional Paleogene and fertile post-collisional Neogene Kerman Belt. Shafiei et al. (2009) described the Paleogene suites as plagioclase-quartz-K-feldspar granitoids with minor ferromagnesian minerals, whereas the Neogene granitoids are mostly plagioclase-quartz-hornblende granitoids.

The Neogene granitoids of the Kerman Belt, similar to the TVC, are distinctly more fractioned than Paleogene volcanic rocks with relative enrichment in incompatible elements and LREE and depletion in MREE-HREE (Fig. 18). These values suggest that hornblende was significant control on Neogene volcanic rocks of the Kerman Belt. The Neogene volcanic rocks of the Kerman Belt mostly display positive Eu anomalies, suggesting either hydrous and/or oxidized magma. In contrast, the Paleogene suites show mildly negative anomaly similar to the TVC (Fig. 19), which are consistent with plagioclase fractionation.

Siddiqui (2004) and Richards et al. (2012) reported geochemical data for the Paleogene and Neogene Chagai Arc. The Paleogene volcanic rocks are described as mostly pyroxene-plagioclase volcanic rocks by Richards et al. (2012), whereas the Neogene volcanic rocks are described as pyroxene-hornblende-plagioclase volcanic rocks by Siddique (2004) and Richards et al. (2012).

Like the Neogene Kerman Belt and the TVC, the Neogene Chagai Arc volcanic rocks are distinctly enriched in incompatible elements and LREE relative to Paleogene volcanic rocks (Fig. 18) and are more depleted in MREE-HREE (Fig. 18). Most of the Chagai rocks lack a Eu anomaly, suggesting magmas were either more oxidized or hydrous than the TVC.

Comparison of the TVC with Chagai Arc and Kerman Belt on the plot of La/Sm vs. Sm/Yb shows significant similarity between the TVC, Chagai Arc, and Kerman Belt (Fig. 22b). The Paleogene volcanic rocks of the Kerman Belt show significantly lower Sm/Yb and La/Sm ratios, whereas the TVC, the Neogene Kerman Belt, and Neogene Chagai Arc volcanic rocks show similar ratios to the TVC and Bazman samples. ; Haschke et al., 2006; Richards and Kerrich, 2007), The Sm/Yb ratio of the TVC, Chagai Arc, and the Kerman Belt show signature of normal thickness crust and likely fractionated pyroxene and amphibole from the magmas in the absence of residual garnet at shallow crustal depths (Kay et al., 1991; Kay and Mpodozis, 2001; Haschke et al., 2002).

Comparison of the TVC with Kerman Belt Nd and Sr isotopes (Shafiei et al., 2009) shows similar signature of mantle-derived origin. The TVC sampls appear to be more contaminated than the Kerman Belt samples, having lower $^{143}Nd/^{144}Nd$ and higher $^{87}Sr/^{86}Sr$ composition(Fig. 23).

These results and the depths estimates of amphibole crystallization suggest that mantle derived magmas likely stalled in the upper crust (at depths ~20 km) and evolved to more felsic composition through fractional crystallization and crustal assimilation. These interpretations are also supported by the lack of basalt or basaltic andesite samples within the TVC rock suite, which have evolved compositions with Mg#<0.54 and Ni<100 ppm.

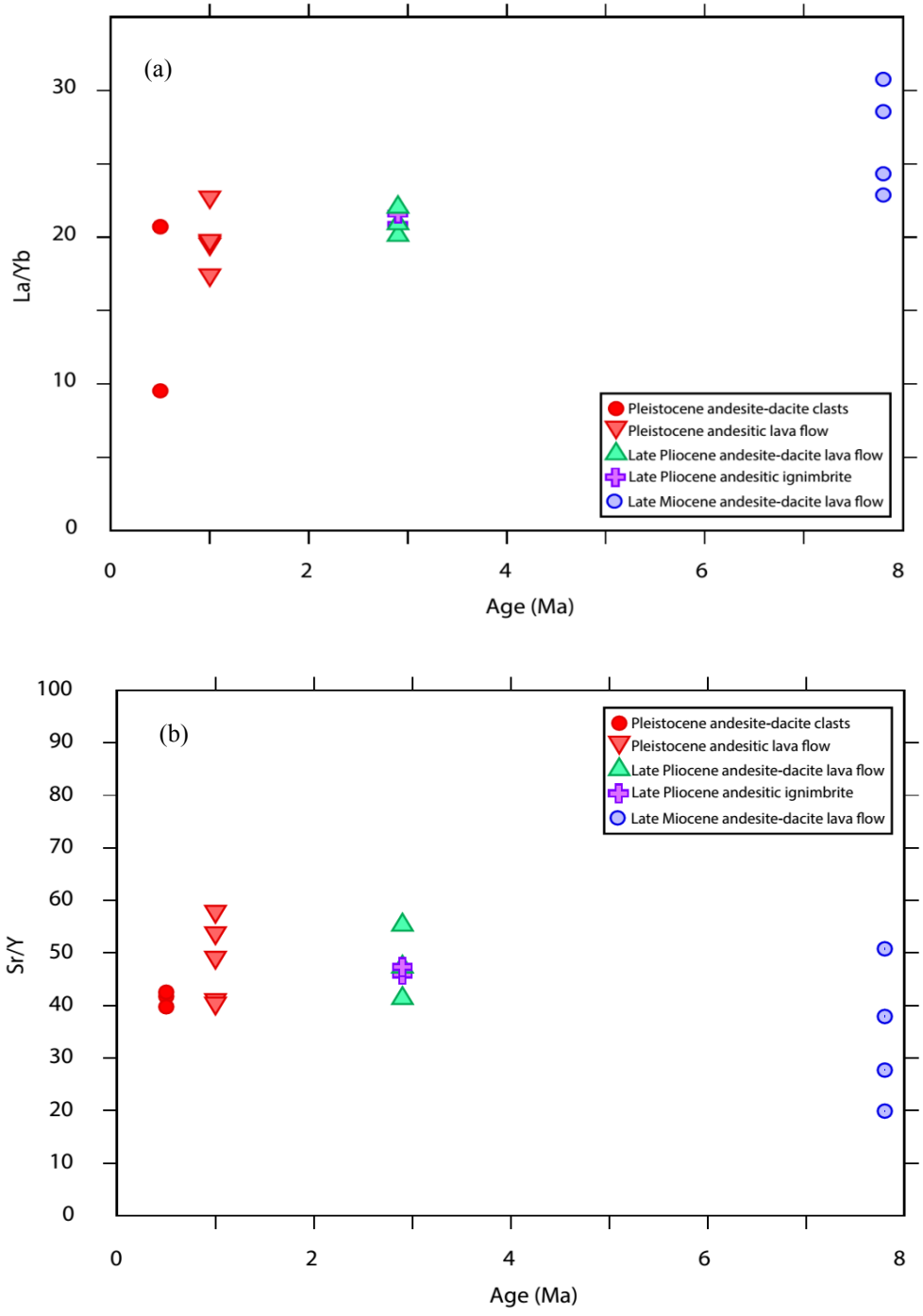

Fig. 21 Diagrams of variation of (a) La/Yb and (b) Sr/Y ratios versus time.

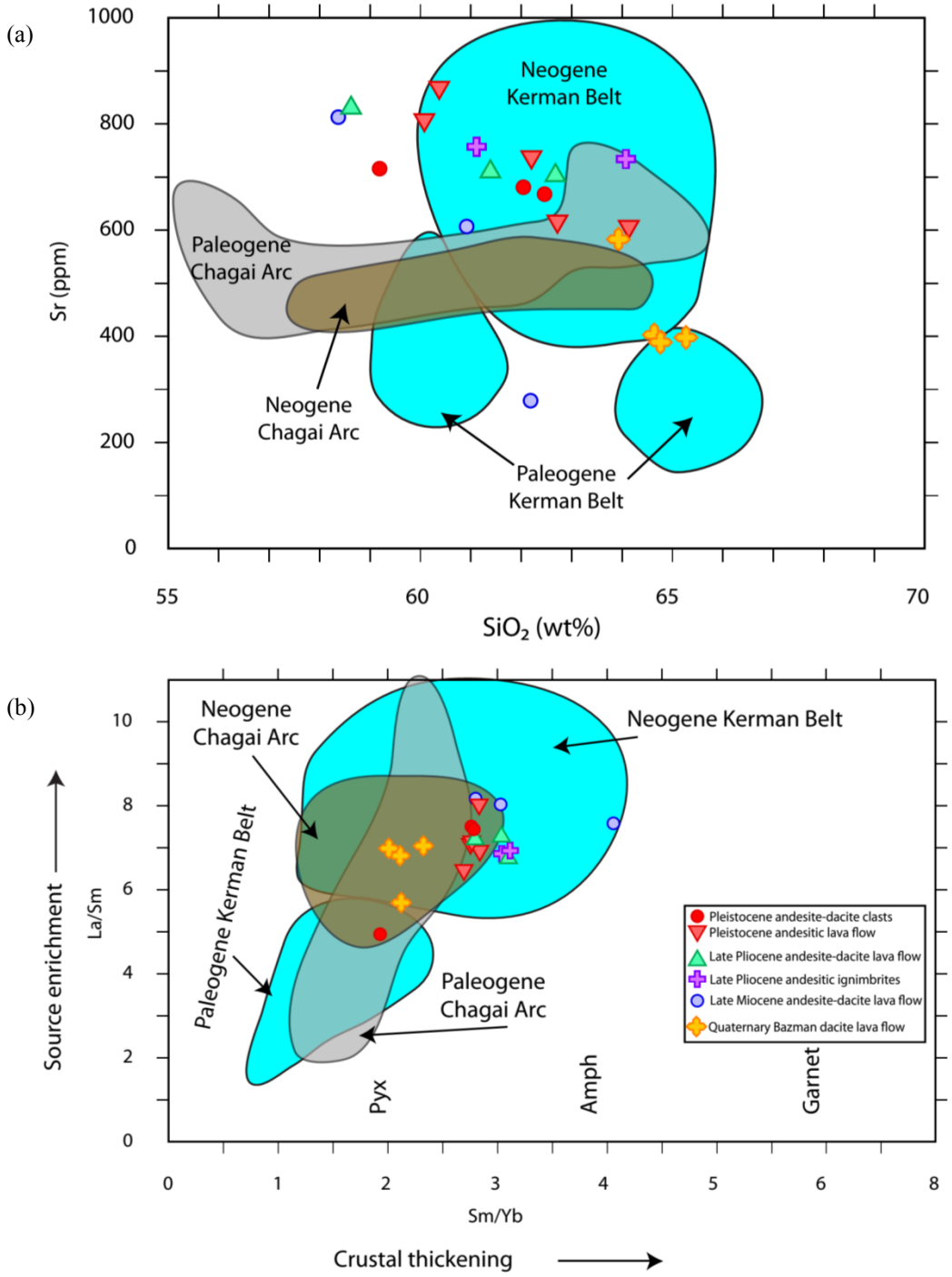

Fig. 22: Plots of (a) Sr versus SiO_2; (b) La/Sm versus Sm/Yb ratios –for the TVC and Bazman SamplesThe field for the Chagai Arc is from Siddiqui (2004); Nickolson et al. (2010); and Richards et al. (2012); the field for the Kerman Belt is from Shafiei et al. (2009). Abbreviation: Pyx = Pyroxene, Amph = Amphibole.

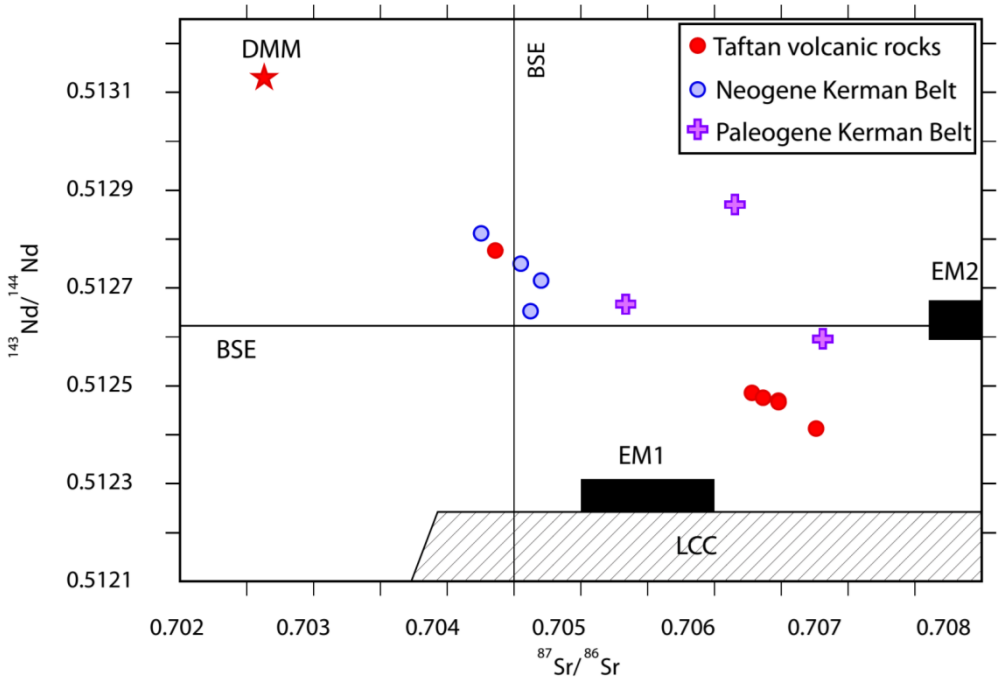

Fig 23: Isotopic ratios (measured) plot of $^{143}Nd/^{144}Nd$ versus $^{87}Sr/^{86}Sr$ for the TVC and the Kerman Belt. Data for the TVC are for Pang et al. (2014) and the Kerman Belt from Shafiei et al. (2009). Enriched mantle (EM1 and EM2) are from Faure (2001), lower continental crust (LCC) are from Dargahi et al. (2010), bulk silicate earth (BSE) and depleted MORB mantle (DMM) are from Workman and Hart (2005).

11.4. Crustal Assimilation

Variations of incompatible elements such as Ba, Rb, and Th, as well radiogenic isotopes can provide insight into fractionation and crustal rock contamination in magmas through assimilation-fractional crystallization (AFC; Depaolo, 1981).

On a plot of Ba vs. Rb (Fig. 24a), incompatibility of Ba and Rb in biotite- and K-feldspar-free mafic to intermediate magmas is demonstrated by a line with Ba/Rb ratio of ~10 (Trumbull et al., 1999). The Bazman and Chagai Arc samples fall close to this line, but the TVC and Kerman Belt rocks scatter away from this line to slightly higher Rb concentrations. Fractional crystallization of amphibole from the TVC magmas cannot explain relative enrichment of both Rb and Ba by partitioning in this mineral, because the partition coefficient of Rb is higher than Ba (Marks et al., 2004). Shafiei et al. (2009) have argued that LILE trace elements such as Ba and Rb are enriched in the Kerman Belt magmas due to continental crust assimilation as was evident from Nd-Sr isotopes (Fig. 23). Likewise, the relatively enriched

Nd and Sr isotopic ratios of the TVC are also indicative of upper crustal rock involvement in the TVC evolution.

On a plot of Th vs. SiO_2 (Fig. 24b) both late Miocene and Plio-Pleistocene volcanic rocks show an increasing trend with SiO_2, which indicates degree of contamination increases with magma evolution. A similar trend is also observed for the Bazman samples, but Th concentration is less enriched, indicating the Bazman sample are likely less contaminated by upper crustal rocks. The Neogene Kerman Belt volcanic rocks, similarly, display increase of Th concentration with SiO_2, but are less enriched in Th relative to the TVC that are consistent with Sr-Nd isotopic ratios (Fig. 23). The Paleogene Kerman Belt and and Chagai Arc volcanic rocks, in contrast, does not show clear trend.

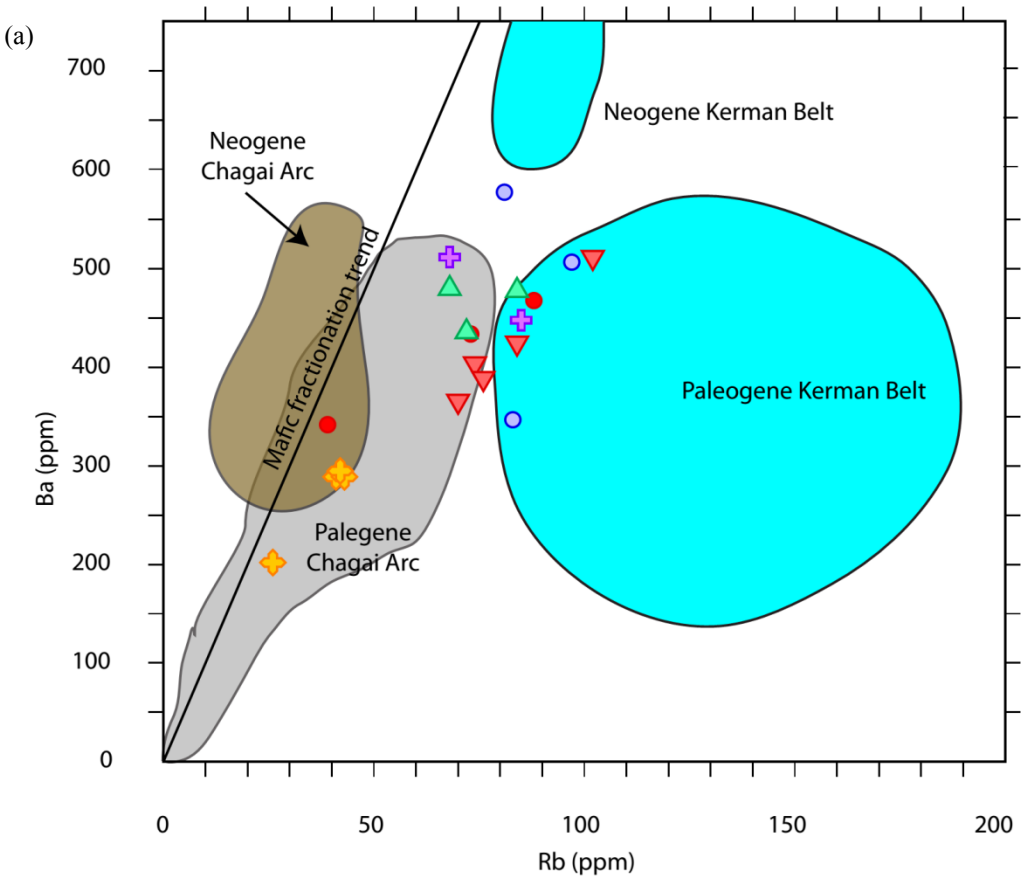

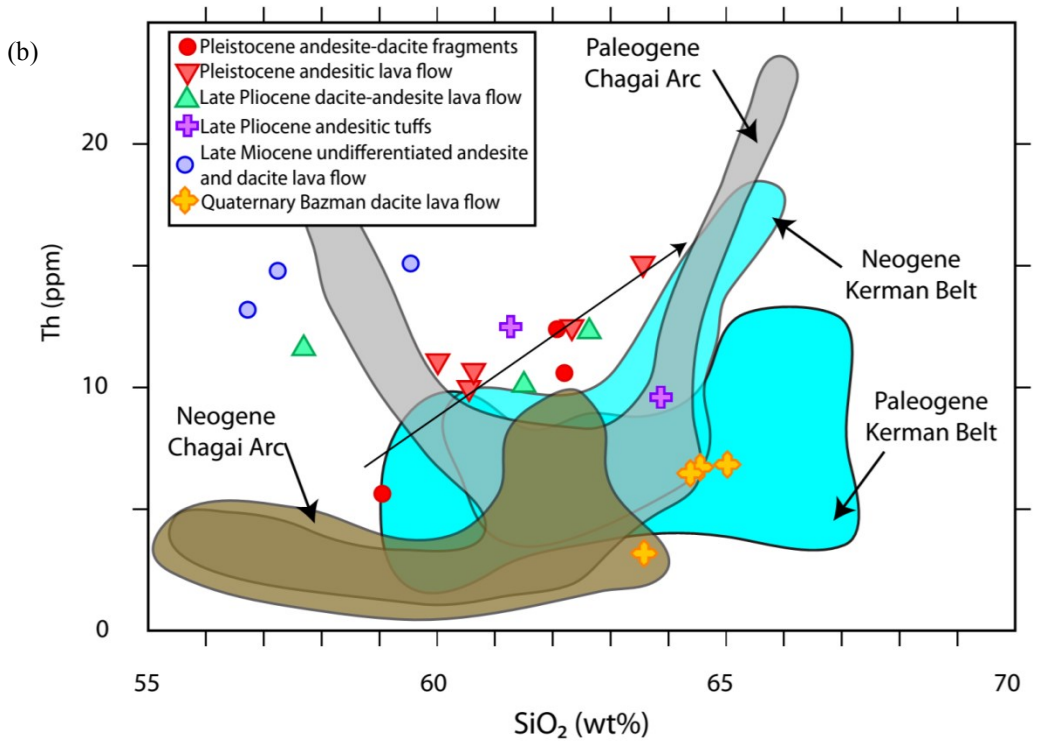

Fig. 24: Plots of (a) Ba versus Rb and (b) Th versus SiO_2 for the TVC samples as indicators of magmatic fractional crystallization or crustal contamination. Field for Chagai Arc is from Siddiqui (2004); Nickolson et al. (2010); and Richards et al. (2012); field for Kerman Belt from Shafiei et al. (2009).

11.5. Recharge processes

Plagioclase phenocrysts from the TVC show complex zonation and sieve textures. Such features could be explained by mixing of a pulse of hotter magma with crystallizing magma, resulting in partial dissolution of plagioclase phenocrysts and the formation of sieve textures (Murphy et al., 2000; Smith et al., 2013; Béguelin et al., 2015; Howe et al., 2015). Observed reverse zoning in orthopyroxene with more mafic rims than cores may also be generated by mixing of more mafic magma into an evolved shallow crustal magma chamber (Sakuyama, 1978; Nakagawa et al., 2002). Resorbed quartz phenocrysts are widely observed in the Plio-Pleistocene volcanic rocks. Two possible explanations for these resorbed quartz phenocrysts are that they have evolved through semi-adiabatic magma ascent, or that they are residual from a felsic crystal mush that has been remobilized by mafic magma recharge (Tepley et al., 1999; Müller et al., 2009; Chiaradia et al., 2014; Béguelin et al., 2015). The presence of totally opacitized amphibole phenocrysts as a result of depressurization of ascending magma supports the first interpretation. On the hand, the presence of strong resorption of quartz

crystals and mafic enclaves support the second explanation (Müller et al., 2009; Béguelin et al., 2015).

11.6. Magma ascent rates from amphibole mineralogy

Amphibole chemistry can reveal magma ascent rate and how long magma spent in the crust. Two different amphibole breakdown textures occur in the Taftan volcanic rocks: (1) resorption as a result of elevated temperature, and (2) opacitization related to water loss and depressurization (Fig. 14). The presence or absence of different reaction textures in amphiboles from TVC samples implies that the magmas variably stalled and evolved at different pressure-temperature conditions prior to eruption (Rutherford et al., 1988). Amphibole compositions in the late Miocene rocks suggest that the andesitic magmas were hydrous (~5 wt.% H_2O) and pooled at depths of 17–22 km in the mid-crust and started to crystallize at ~1000°C, prior to ascent into the upper crust. The thickness of opacite rims in amphiboles has also been suggested as a measure for the ascent rate of magma (Rutherford, 2008). The relatively thick rims, and in some cases the fully opacitized nature of the amphiboles in the late Miocene andesites is interpreted to reflect water loss during magma ascent towards the surface at a relatively slow rate. Amphiboles in the Plio-Pleistocene andesites show bimodal population (high-Al and low-Al) and mild to severely resorbed textures with variably opacitized rims. Their compositions indicate that these amphiboles began to crystallize from a hot and hydrous magma (~5.5 wt.% H_2O) at a temperature of ~910°C, and at the depths of 5–23 km, before undergoing decompressive breakdown and melting during ascent and eruption (Rutherford et al., 1998; Rutherford and Devine, 2003).

Amphibole disequilibrium textures such as amphibole reaction rims, , and broad ranges of depths of amphibole crystallization in a single volcanic rock have been observed in the Plio-Pleistocene andesitic and dacitic rocks.

Amphiboles from the Plio-Pleistocene dacites similarly show bimodal population (high-Al and low-Al), resorbed textures and variably opacitized rims, with compositions suggesting crystallization from a hydrous magma (~5.5 wt.% H_2O) at a temperature of ~860°C and depths of 4–8 km.

These observations can be interpreted in terms of crystallization of amphibole at various crustal depths, prior to incorporation of mixed phenocryst assemblages in the erupted magma (Rutherford and Hill, 1993,Weibe et al., 2004; Cao et al., 2009; Chambefort et al., 2013; Chiaradia et al., 2011, 2014; Kiss et al., 2014).

11.7. Tectonomagmatic history

11.7.1. Late Miocene

Magmatism in the TVC began during the late Miocene (~8 Ma) ~20 km west of the current Taftan volcano (Fig. 25a). Mantle derived magmas were modified during ascent through the crust by fractional crystallization and crustal contamination as shown by enrichments in incompatible element enrichments such as Cs, Th, and U (Fig. 18a) and evolved $^{87}Sr/^{86}Sr$ and εNd isotope ratios. Amphibole barometry suggests that the magmas evolved by fractional crystallization that likely started in a middle to upper crustal magma chamber at a depth of ~20 km prior to ascent to the surface. The abundance of deeply crystallized amphibole phenocrysts in the volcanic rocks supports whole-rock geochemical evidence for extensive amphibole fractionation (e.g., depletion of HREE relative to MREE), likely due to the relatively hydrous nature of magmas.

11.7.2. Plio-Pleistocene

The center of volcanic activity in the TVC migrated ~20 km eastward during the Plio-Pleistocene (Fig. 25b). Magmatism appears to have been triggered by emplacement of voluminous modified mantle derived andesitic magmas. The amphibole barometry revealed that those magmas likely evolved in a magma chamber at a depth of ~20 km prior to eruption.

Geochemically, similar to the late Miocene magmas, these magmas show enrichment of incompatible elements such as Cs, Th, and U (Fig. 18a) as a result of fractional crystallization. Similar to the late Miocene magmas, $^{87}Sr/^{86}Sr$ ratios also indicate that crustal contamination was involved in Plio-Pleistocene magmas.

11.8. Economic potential of the Taftan volcanic complex

Hydrous (>4 wt.% H_2O) and relatively oxidized (up to ΔFMQ+2) arc magmas can generate magmatic hydrothermal Cu±Mo±Au ore deposits by exsolution of hydrothermal fluids from upper crustal magma chambers (Burnham, 1979; Richards, 2003, 2011; Cooke et al., 2005; Sillitoe, 2010).

The genetic model outlined above suggests that volcanic rocks of the TVC are outcrops of arc magmas generated in the Makran Arc in response to subduction of Indian Oceanic lithosphere beneath Central Iran. The long-lived magmatic activity of the TVC, since the late Miocene to the present day, suggests that a large volume of magma has been active in the mid- to upper crust for ~8 m.y. The late Miocene magmas were hydrous (>5 wt.% H_2O) and relatively oxidized (ΔFMQ>+1.2), and therefore may have been fertile for the formation of magmatic-hydrothermal ore deposits, as suggested by the known Kharestan Cu porphyry (6.1 ± 0.4 Ma) and Siah Jangal epithermal Au prospects.

The Plio-Pleistocene magmas were similarly hydrous and oxidized magmas (>5 wt.% H_2O and ΔFMQ>+1.5), and there are clear manifestations of volatile exsolution (e.g., several argillic and fumarolic alteration zones occur at the peak and on the flanks of the Taftan volcano (Fig. 3). It is suggested that the TVC is prospective for porphyry and epithermal mineralization, and that more intensive exploration of the known alteration zones is warranted.

12. Conclusions

The large (~20 km diameter) Taftan volcanic complex was formed by multiple eruptions of volcanic materials over a period of ~8 m.y. from the late Miocene to the present time. The earliest volcanic activity started with explosive eruptions of andesitic to dacitic lava flows on the Cretaceous to Eocene volcanic and sedimentary basement. Afterwards, the Taftan magmatic center shifted 20 km to the east to the current location, and has erupted voluminous andesitic and dacitic lavas and pyroclastic materials during the Quaternary (since ~3.1 Ma).

Major and trace element compositions of the Taftan rocks show that they are typical subduction-related high-K calc-alkaline to calc-alkaline magmas, with depletions of Nb, Ta, and Ti and relative enrichments of LILE and Th and U.

Amphibole phenocryst compositions gradually change from high-Al pargasite to low-Al magnesio-amphibole from the late Miocene to the Quaternary. Both populations crystallized from water saturated magma (>4 wt.% H_2O) but the high-Al amphiboles (mostly the late Miocene samples) were formed at deeper crustal level, prior to eruption at the surface.

Temperature and redox modelling of the Taftan volcanic complex based on magnetite-ilmenite pairs, amphibole geothermobarometer, and whole rock Fe^{3+}/Fe^{2+} ratios shows that andesite and dacite resided at temperatures between 800° to 1000°C under oxidizing conditions (ΔFMQ average = +1.7 ± 0.3).

The geochemical signatures of the TVC show that volcanism at Taftan was initiated in the late Miocene by emplacement of voluminous modified mantle wedge-derived magmas at a depth of ~20 km, and evolved by fractional crystallization and crustal contamination.

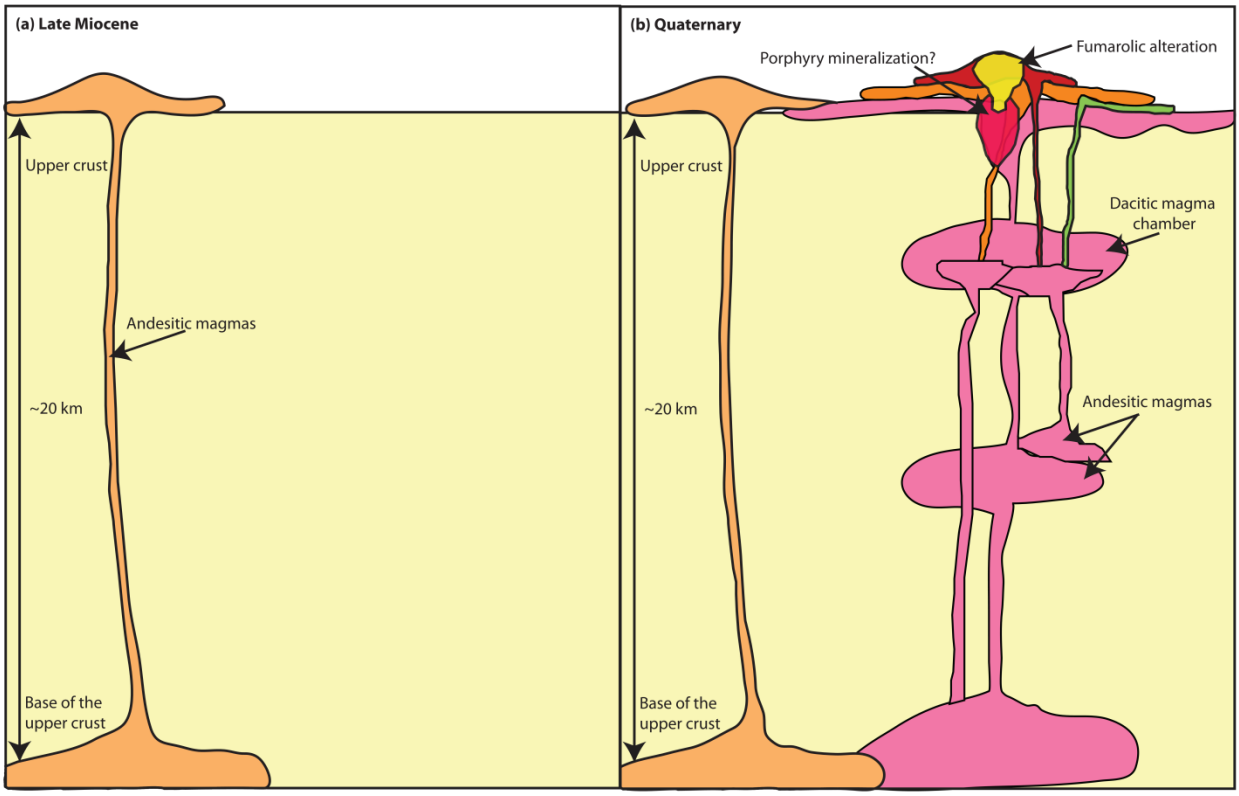

Fig. 25: Simplified schematic tectonomagmatic evolution of the TVC from the late Miocene (a) to the Quaternary (b).

The geochemical signatures of the Plio-Pleistocene volcanic rocks show that andesitic to dacitic magmas are not directly cogenetic with the late Miocene magmas as shown by a change from calc-alkaline composition than high-K calc-alkaline composition. These magmas likely originated from the mantle wedge and were modified by fractionation and crustal contamination during ascent. The range of pressures calculated from amphibole geobarometry, suggest that the magmas evolved at multiple depths in the mid- to upper crust between 5–20 km depths.

The Taftan volcanic rocks appear to be prospective for porphyry and epithermal type mineralization because of their high water content (>5 wt.% H_2O) and relatively oxidized nature (up to ΔFMQ>+1.5). This suggestion is supported by presence of the Kharestan Cu porpyry prospect and Siah Jangal epithermal Au in the late Miocene, and several argillic and fumarolic alteration zones in Plio-Pleistocene rocks on the top, east, southeast, and the west of the current Taftan volcano. The complex has been minimally explored for mineral resources to date, but the observations listed above suggest that it may warrant more detailed exploration, in particular below the large outcropping argillic alteration systems.

References:

Agard, P., Omrani, J., Jolivet, L., and Mouthereau, F., 2005, Convergence history across Zagros (Iran): constraints from collisional and earlier deformation: International Journal of Earth Sciences, 94, 401–419.

Agard, P., Monie, P., Gerber, W., Omrani, J., Molinaro, M., Meyer, B., Labrousse, L., Vrielynck, B., Jolivet, L., Yamato, P., 2006, Transient, synobduction exhumation of Zagros blueschists inferred from P–T, deformation, time, and kinematic constraints: implications for Neotethyan wedge dynamics. Journal of Geophysical Research 111, B11401 http://dx.doi.org/10.1029/2005JB004103.

Agard, P., Omrani, J., Jolivet, L., Whitechurch, H., Vrielynck, B., Spakman, W., Monié, P., Meyer, B., Wortel, R., 2011, Zagros Orogeny: A Subduction Dominated Process, Geological Magazine, 148(5-6), 692-725.

Aghazadeh, M., Hou, Z., Badrzadeh, Z., & Zhou, L., 2015, Temporal–spatial distribution and tectonic setting of porphyry copper deposits in Iran: Constraints from zircon U–Pb and molybdenite Re–Os geochronology. Ore Geology Reviews.

Aghazadeh, M., Castro, A., Badrzadeh, Z., and Vogt, K., 2011, Post-collisional polycyclic plutonism from the Zagros hinterland: the Shaivar Dagh plutonic complex, Alborz belt, Iran: Geological Magazine, 148, 980–1008.

Aghazadeh, M., Castro, A., Rashidnejad Omran, N., Emami,M. H.,Moinvaziri, H., Badrzadeh, Z. 2010, The Gabbro (Shoshonitic)–Monzonite–Granodiorite Association Of Khankandi Pluton, Alborz Mountains, Nw Iran. Journal Of Asian Earth Sciences, 38, 199–219.

Ahmadian, J., Haschke, M., McDonald, I., Regelous, M., Ghorbani, M., Emami, M., Murata, M., 2009, High magmatic flux during Alpine-Himalayan collision: Constraints from the Kal e-Kafi complex, central Iran: Geological Society of America, Bulletin, 121, 857-868.

Ahmadi Khalaji, A., 2006, Petrology of the granitoid rocks of the Boroujerd area. Ph.D Thesis, University of Tehran, Tehran, Islamic Republic of Iran.

Ahmadi Khalaji, A., Esmaeily, D., Valizadeh, M.V., Rahimpour-Bonab, H., 2007, Petrology and geochemistry of the granitoid complex of Boroujerd, Sanandaj-Sirjan Zone, Western Iran: Journal of Asian Earth Sciences, 29, 859–877.

Alavi, M., 1994, Tectonics of the Zagros orogenic belt of Iran: new data and interpretations: Tectonophysics, 229, 211–238.

Alavi M, 2004, Regional stratigraphy of the Zagros fold-thrust belt of Iran and its proforeland and evolution. American Journal of Science, 304, 1-20.

Andersen, D.J., and Lindsley, D.H., 1985, New models for the Ti-magnetite/ilmenite geothermometer and oxygen barometer: Abstract AGU 1985 Spring Meeting Eos Transactions, 46, p.416.

Armstrong, J.T., 1995, A Package Of Correction Programs For The Quantitative Electron Microbeam X-Ray Analysis Of Thick Polished Materials, Thin Films, And Particles. Microbeam Analysis, 4, 177–200.

Arshadi, S., Förster H., 1983, Geological Structure And Ophiolites Of The Iranian Makran. Geodynamic Project (Geotraverse) In Iran (Final Report), Geological Survey Of Iran, Report No. 51, 479–88.

Aubourg, C., Smith, B., Bakhtari, H., Guya, N., Eshraghi, A., S., L., Molinaro, M., Braud, X., Delaunay, S., 2004, Post-Miocene shortening pictured by magnetic fabric across the Zagros-Makran syntaxis. In "Orogenic curvature: integrating paleomagnetic and structural analyses." (A. J. Sussman, and A. B. Weil, Eds.), pp. 17-40. Geological Society of America special paper, Boulder, Colorado.

Auden, J.B., 1974, Afghanistan-West Pakistan. In: Spencer, A.M. (ed.). Mesozoic-Cenozoic Orogenic belt. Data for Orogenic studies. Special publication geological Society of London, 4, 235-253.

Ayati, F., Yavuz, F., Asadi, H.H., Richards, J.P., and Jourdan, F., 2013, Petrology and geochemistry of calc-alkaline volcanic and subvolcanic rocks, Dalli porphyry copper-gold deposit, Markazi Province, Iran: International Geology Review, 55, 158–184.

Azizi, H., and Jahangiri, A., 2008, Cretaceous subduction-related volcanism in the northern Sanandaj-Sirjan Zone, Iran: Journal of Geodynamics, 45, 178–190.

Azizi, H., Moinevaziri, H., 2009, Review of the tectonic setting of Cretaceous to Quaternary volcanism in northwestern Iran. Journal of Geodynamics 47, 167–179.

Azizi, H., Tanaka, T., Asahara, Y., Chung, S., Zarrinkoub, M., 2011, Discrimination of the age and tectonic setting for magmatic rocks along the Zagros thrust zone, northwest Iran, using the zircon U–Pb age and Sr–Nd isotopes, Journal of Geodynamics, 52, 304– 320.

Bacon, C.R., Hirschmann, M.M., 1988. Mg/Mn partitioning as a test for equilibrium between coexisting Fe–Ti oxides. American Mineralogist 73, 57–61.

Ballhaus, C., 1993, Redox states of lithospheric and asthenospheric upper mantle. Contributions to Mineralogy and Petrology, 114(3), 331-348.

Bayer, R., Chery, J., Tatar, M., Vernant, P., Abbassi, M., Masson, F., Nilforoushan, F., Doerflinger, E., Regard, V., Bellier, O., 2006, Active deformation in Zagros-Makran transition zone inferred from GPS measurements, Geophysical Journal International, 165, 373–381.

Béguelin, P., Chiaradia, M., Beate, B., & Spikings, R., 2015, The Yanaurcu volcano (Western Cordillera, Ecuador): A field, petrographic, geochemical, isotopic and geochronological study. Lithos, 218, 37-53.

Berberian F., Berberian, M., 1981, Tectono-plutonic episode in Iran. Geodynamic series, 3, WG6, American Geophysical Union, 5-32.

Berberian, M., King, G.C.P., 1981, Towards a paleogeography and tectonic evolution of Iran, Canadian Journal of Earth Science, 18, 210–265, doi:10.1139/e81-019.

Biabangard, H., And Moradian, A., 2008, Geology And Geochemical Evaluation Of Taftan Volcano, Sistan And Baluchestan Province, Southeast Of Iran: Chinese Journal Of Geochemistry, 27, 356–369.

Blevin, P.L., 2004, Redox and compositional parameters for interpreting the granitoid metallogeny of Eastern Australia: Implications for gold-rich ore system: Resource Geology, 54, 241–252.

Bröcker, M., Fotoohi Rad, G., Burgess, R., Theunissen, S., Paderin., I., Rodionov, N., Salimi, Z., 2013, New age constraints for the geodynamic evolution of the Sistan Suture Zone, eastern Iran, Lithos, 170, 17-34.

Byrne, D., Sykes, L., 1992, Great Thruste Arthquakesa Nda Seismics Lip Along The Plate Boundary Of The Makran Subduction Zone, Journal Of Geophysical Research, 97(B1), 449-478.

Candela, P., 1997, A review of Shallow, Ore-related Granites: Textures, Volatiles, and Metals. Journal of Petrology, 38(12), 1619-1633.

Cas, R.A.F., Wright, J.V., 1991, Subaquoeus Pyroclastic Flows And Ignimbrites: An Assessment: Bulletin Of Volcanology, 53, 357-380.

Castillo, P.R., 2012, Adakite Petrogenesis, Lithos, 134–135, 304–316.

Chamberfort, I, Dilles, J.H., Longo, A., 2013, Amphibole Geochemistry of the Yanacocha Volcanics, Peru: Evidence for Diverse Sources of Magmatic Volatiles Related to Gold Ores, Journal of Petrology, doi: 10.1093/petrology/egt004.

Chaussard, E., & Amelung, F., 2014, Regional controls on magma ascent and storage in volcanic arcs. Geochemistry, Geophysics, Geosystems, 15(4), 1407-1418.

Chiaradia, M., Müntener, O., Beate, B., 2011. Enriched basaltic andesites from mid-crustal fractional crystallization, recharge, and assimilation (Pilavo Volcano, Western Cordillera of Ecuador). Journal of Petrology 52 (6), 1107–1141.

Chiaradia, M., Müntener, O., Beate, B., 2014. Quaternary sanukitoid-like andesites generated by intracrustal processes (Chacana Caldera Complex, Ecuador): implications for Archean sanukitoids. Journal of Petrology 55 (4), 769–802.

Chiu, H.Y., Chung, S.L., Zarrinkoub, M.H., Mohammadi, S.S., Khatib, M.M., and Iizuka, Y., 2013, Zircon U–Pb age constraints from Iran on the magmatic evolution related to Neotethyan subduction and Zagros orogeny: Lithos, 162–163, 70–87.

Dargahi, S., Arvin, M., Pan, Y., & Babaei, A., 2010, Petrogenesis of post-collisional A-type granitoids from the Urumieh–Dokhtar magmatic assemblage, Southwestern Kerman, Iran: constraints on the Arabian–Eurasian continental collision. Lithos, 115(1), 190-204.

Davidson, J.P., 1996, Deciphering mantle and crustal signatures in subduction zone magmatism, in Bebout, G.E., Scholl, D.W., Kirby, S.H., and Platt, J.P., eds., Subduction: Top to bottom: American Geophysical Union, Geophysical Monograph 96, p. 251–262.

Davidson, J.P., Hora, J.M., Garrison, J.M., and Dungan, M.A., 2005, Crustal forensics in arc magmas: Journal of Volcanology and Geothermal Research, v. 140, p. 157–170.

Davoudzadeh, M., Lensch, G., and Weber-Diefenbach, K., 1986, Contribution to the paleogeography, stratigraphy and tectonics of the Infracambrian and Lower Paleozoic of Iran: Neues Jahrbuch für Geologie und Pala¨ontologie, Abhhandlungen, 172, 245–269.

Defant,M.J., Drummond,M.S., 1990. Derivation of somemodern arc magmas bymelting of young subducted lithosphere. Nature 347, 662–665.

DeMets, C., Gordon, R.G., Angus, D.F. and Stein, S., 1994, Effect of recent revisions to the geomagnetic reversal time scale on estimates of current plate motions. Geophysical Review Letter, 21, 2191–2194.

Depaolo, D. J., 1981, Trace element and isotopic effects of combined wallrock assimilation and fractional crystallization. Earth and planetary science letters, 53(2), 189-202.

Dilek, Y., Imamverdiyev, N., Altunkaynak, Ş., 2010, Geochemistry and tectonics of Cenozoic volcanism in the Lesser Caucasus (Azerbaijan) and the peri-Arabian region: collision-induced mantle dynamics and its magmatic fingerprint. International Geology Review, 52, 536-578.

Droop, G.T.R., 1987. A general equation for estimating Fe3+ concentrations in ferromagnesian silicates and oxides from microprobe analyses, using stoichiometric criteria. Mineralogical Magazine, 51, 431–435.

Eftekharnejad, J., 1981, Tectonic division of Iran with respect to sedimentary basins. Journal of Iranian Petroleum Society 82, 19–28 (in Farsi).

Ellouz-Zimmermann, N., Lallemant, S., Castilla, R., Mouchot, N., Leturmy, P., Battani, A., Buret, C., Cherel, L., Desaubliaux, G., Deville, E., Ferrand, J., Lügcke, A., Mahieux, G., Mascle, G., Mühr, P., Pierson-Wickmann, A., Robion, P., Schmitz, J., Danish, M., Hasany, S., Shahzad, A. and Tabreez, A., 2007, Offshore frontal part of the Makran accretionary prism: the Chamak survey (Pakistan). In: Thrust Belts and Foreland Basins (Eds O. Lacombe, J. Lave', F. Roure and J. Verges), 351–366.

Emami, M.H., 2000, Magmatism In Iran. G.S.I, Isbn: 964-6178-01-4, 608 P.

Eyuboglu, Y., Santosh, M., Dudas, F.O., Chung, S.L., and Akaryalı, E., 2011, Migrating magmatism in a continental arc: Geodynamics of the Eastern Mediterranean revisited: Journal of Geodynamics, 52, 2–15.

Eyuboglu, Y., Santosh, M., Yi, K., Bektas, O., and Kwon, S., 2012, Discovery of Miocene adakitic dacite from the Eastern Pontides Belt (NE Turkey) and a revised geodynamic model for the Late Cenozoic evolution of the Eastern Mediterranean region: Lithos, 146–147, 218–232.

Falcon, N.L., 1974, Southern Iran: Zagros Mountains. In: Spencer, A. (Ed.) Mesozoic–Cenozoic Orogenic Belts. Geological Society, London, Special Publications, 4, 199–211.

Farhoudi, G., Karig, D.E., 1977, Makran of Iran and Pakistan as an active arc system: Geology, 5, 64-68.

Faure, G., 2001, Origin of Igneous Rocks, the Isotopic Evidence. Springer-Verlag, Berlin Heidelberg. 496 pp.

Fotoohi Rad, G.R., Droop, G.T.R., Burgess, R., 2009. Early Cretaceous exhumation of highpressure metamorphic rocks of the Sistan Suture Zone, eastern Iran. Geological Journal, 44, 104–116.

Frey, F.A., Chappell, B.W., Roy, S.D., 1978, Fractionation of rare-earth elements in the

Tuolumne Intrusive Series, Sierra Nevada batholith, California. Geology 6, 239–242.

Frost, B.R., Barnes, C.G., Collins, W.J., et al., 2001, A geochemical classification for granitic rocks. Journal of Petrology, 42(11), 2033-2048.

Garrison, J.M., Davidson, J.P., 2003. Dubious case for slab melting in the Northern volcanic zone of the Andes. Geology 31 (6), 565–568.

Ghalamghash, J., Mirnejad, H., Rashid, H., 2009, Mixing and mingling of mafic and felsic magmas along the Neo-Tethys continental margin, Sanandaj-Sirjan zone, NW Iran: A case study from the Alvand pluton. Neues Jahrbuch Mineralogie – Abhandlungen, 186(1), 79-93.

Ghasemi, A., and Talbot, C.J., 2006, A new tectonic scenario for the Sanandaj-Sirjan Zone (Iran): Journal of Asian Earth Sciences, 26, 683–693.

Ghazi, M., Hassanipak, A.A., Tucker, P.J., Mobasher, K., 2001, Geochemistry and 40Ar–39Ar ages of the Mashhad Ophiolite, NE Iran. Eos Transactions. American Geophysical Union, Fall Meeting, 82 (47).

Ghazi, A.M., Pessagno, E.A., Hassanipak, A.A., Kariminia, S.M., Duncan, R.A., Babaie, H.A., 2003. Biostratigraphic zonation and 40Ar/39Ar ages for the Neotethyan Khoy ophiolite of NW Iran. Palaeogeogr. Palaeoclimatology Palaeoecology, 193, 311-323.

Ghazban, F., 2002, Geological And Geothermal Investigation Of Mount Taftan, Se, Iran, Geothermal Resources Council Transactions, 26, 22-25.

Ghorbani, M., Bezenjani, R., 2011, Slab Partial Melts From The Metasomatizing Agent to Adakite, Tafresh Eocene Volcanic Rocks, Iran, Island Arc, 20, 188–202.

Glennie, K.W., 2000, Cretaceous tectonic evolution of Arabia's eastern plate margin: A tale of two oceans, in Middle East models of Jurassic/Cretaceous carbonate systems: SEPM (Society for Sedimentary Geology) Special Publication, 69, 9–20.

Golonka, J., 2004, Plate tectonic evolution of the southern margin of Eurasia in the Mesozoic and Cenozoic, Tectonophysics 38, 235 – 273.

Grando, G. and McClay, K., 2007, Morphotectonics domains and structural styles in the Makran accretionary prism, offshore Iran. Sedimentary Geology, 196, 157–179.

Gudmundsson, A., 2000, Dynamics of volcanic systems in Iceland: example of tectonism and volcanism at juxtaposed hot spot and mid-ocean ridge systems. Annual Review of Earth and Planetary Sciences, 28(1), 107-140.

Hanson, G.N., 1980, Rare earth elements in petrogenetic studies of igneous systems.

Annual Review of Earth and Planetary Sciences 8, 371–406.

Haschke, M., Pearce, J.A., 2006, Lithochemical exploration tools revisited: MnO and REE, GSA—Backbone of the Americas Meeting, Abstract 16–8, Mendoza

Haschke, M., Scheuber, E., Günther, A., Reutter, K.J., 2002. Evolutionary cycles during the Andean orogeny: repeated slab breakoff and flat subduction? Terra Nova 14, 49–55.

Haschke, M., Ahmadian, J, Murata, M., McDonald, I., 2010, Copper Mineralization Prevented By Arc-Root Delamination During Alpine-Himalayan Collision In Central Iran, Economic Geology, 105, 855-865.

Hassanzadeh, J., Ghazi, A.M., Axen, G., Guest, B., Stockli, D.F., Tucker, P., 2002, Oligocene mafic-alkaline magmatism in north and northwest of Iran: evidence for the separation of the Alborz from the Urumieh–Dokhtar magmatic arc. Geological Society of America Abstracts with Programs, 34 (6), 331.

Hassanzadeh, J., Stockli, D.F., Horton, B.K., Axen, G.J., Stockli, L.D., Grove, M., Schmitt, A.K., Walker, J.D., 2008, U-Pb zircon geochronology of Late Neoproterozoic-Early Cambrian granitoids in Iran: Implications for paleogeography, magmatism, and exhumation history of Iranian basement, Tectonophysics, 451, 71–96, doi:10.1016/j.tecto. 2007.11.062.

Hawthorne, F., Oberti, R., Harlow, G., Maresch, W., Martin, R., Schumacher, J., Welc, M., 2012, IMA Report, Nomenclature of the amphibole supergroup, American Mineralogist, 97, 2031–2048.

Henderson, P. (Ed.)., 1985, Rare earth element geochemistry. Elsevier.

Hildreth, W., Moorbath, S., 1988. Crustal contributions to arc magmatism in the Andes of central Chile. Contributions to Mineralogy and Petrology 98, 455–489.

Hooper, R.J., Baron, I.R., Agah, S., Hatcher Jr., 1994, The Cenomanian to recent development of the southern Tethyan margin in Iran. The Middle East Petroleum Geoscience (GEO'94) 2, 505–516.

Horton, B.K., Hassanzadeh, J., Stockli, D.F., Axen, G.J., Gillis, R.J., Guest, B., Amini, A., Fakhari, M.D., Zamanzadeh, S.M., Grove, M., 2008, Detrital zircon provenance of Neoproterozoic to Cenozoic deposits in Iran: implications for chronostratigraphy and collisional tectonics. Tectonophysics 451, 97–122.

Howe, T.M., Lindsay, J.M., Shane, P., 2015, Evolution of young andesitic-dacitic magmatic systems beneath Dominica, Lesser Antilles, Journal of Volcanology and Geothermal Research, in press, doi: 10.1016/j.jvolgeores.2015.02.009

Hushmandzadeh, A., 1969, Metamorphisme et granitisation du massif Chapedony (Iran Central): MSc These, Universite Scientifique et Medicale de Grenoble, France, 242 p.

Jackson, J.A., Haines, J., Holt, W., 1995, The accommodation of Arabia-Eurasia plate convergence in Iran. J Geophysical Research, 100, 205-219.

Jamali, H., Dilek, Y., Daliran, F., Yaghubpur, A., Mehrabi, B., 2010, Metallogeny and tectonic evolution of the Cenozoic Ahar–Arasbaran volcanic belt, northern Iran, International Geology Review, 52(4-6), 608-630.

Kay, S.M., Mpodozis, C., 2001, Central Andes ore deposits linked to evolving shallow subduction systems and thickening crust. GSA Today (Geological Society of America), 11(3), 4-9.

Kavanagh, J. L., Menand, T., & Sparks, R. S. J., 2006, An experimental investigation of sill formation and propagation in layered elastic media. Earth and Planetary Science Letters, 245(3), 799-813.

Kay, S.M., Mpodozis, C., Ramos, V.A., Munizaga, F., 1991, Magma source variations for Mid-Late Tertiary magmatic rocks associated with a shallowing subduction zone and a thickening crust in the central Andes (28 to 33°S). In: Harmon, R.S., Rapela, C.W. (Eds.), Andean Magmatism and Its Tectonic Setting: Boulder, Colorado, Geological Society of America Special Paper, 265, pp. 113–137.

Kiss, B., Harangi, S., Ntaflos, T., Mason, P. R., & Pál-Molnár, E., 2014, Amphibole perspective to unravel pre-eruptive processes and conditions in volcanic plumbing systems beneath intermediate arc volcanoes: a case study from Ciomadul volcano (SE Carpathians). Contributions to Mineralogy and Petrology, 167(3), 1-27.

Kokowski, N., Schillhorn, T., Flueh, E.R., Huhn, K., 2000, A newly identified stike slip plate boundary in the north-east Arabian Sea, Geology, 28, 355-358.

Lake Source NL, (2014, May 12), Lake Resources Enters Into An Exclusivity Agreement For Chagai Hills Exploration Licenses In Balochistan, Pakistan, Retrieved October 12, 2014, From Http://Www.Lakeresources.Com.Au/

Lawrence, R.D., Nakata, S.H., Khan, T., 1992, Chaman fault, Pakistan–Afghanistan. Ann. Tectonicae, 6, 196–223.

Leake, B.E., Woolley, A.R., Arps, C.E.S. et al., 1997, Nomenclature Of Amphiboles: Report Of The Subcommittee On Amphiboles Of The International Mineralogical Association, Commission On New Minerals and mineral names. American Mineralogist 82, 1019-1037.

Le Maitre, R.W. (Ed.), 1989. A Classification of Igneous Rocks and Glossary of Terms. Blackwell Scientific Publications, Oxford.

Lepage, L.D., 2003, ILMAT: an Excel worksheet for ilmenite–magnetite geothermometry and geobarometry: Computers and Geosciences, 29, 673–678.

Locock, A.J., 2014, An Excel spreadsheet to classify chemical analyses of amphiboles following the IMA 2012 recommendations, Computer and Geosciences, 62, 1-11.

Maniar, P.O., Piccoli, P.M., 1989, Tectonic discrimination of granitoids. Bulletin Geological Society of America, 101, 635-643.

Marks, M., Halama, R., Wenzel, T., & Markl, G., 2004, Trace element variations in clinopyroxene and amphibole from alkaline to peralkaline syenites and granites: implications for mineral–melt trace-element partitioning. Chemical Geology, 211(3), 185-215.

Masoudi, F.,1997, Contact metamorphism pegmatite development in the region SW of Arak, Iran. – Ph. D. Thesis, Univ. of Leeds, UK (unpubl.).

Mazhari, S.A., Bea, F., Amini, S., Ghalamghash, J., Molina, J.F., Montero, P., Scarrow, J.H., Williams, I.S., 2009, The Eocene bimodal Piranshahr massif of the Sanandaj-Sirjan Zone, West Iran: a marker of the end of the collision in the Zagros orogen: Journal of theGeological Society of London, 166, 53–70.

McCall, G.J.H., Kidd, R.G.W., 1982, The Makran, Southeastern Iran: The Anatomy Of A Convergent Plate Margin Active From Cretaceous To Present. In Leggett J. K. (Eds.) Trench-Forearc Geology: Sedimentation And Tectonics On Modern And Anceint Active Plate Margins, Geological Society, London, Special Publication 10, 387–97.

McCall, G.J.H., 1997, The geotectonic history of the Makran and adjacent areas of southern Iran: Journal of Southeast Asian Earth Sciences, 15, 517–531.

McCall, G.J.H., 2002, A summary of the geology of the Iranian Makran. In: Clift, P.D., Kroon, F.D., Gaedecke, C., Craig, J. (Eds.), The Tectonic and Climatic Evolution of the Arabian Sea Region. Special Publication of the Geological Society of London, 95, 147 204.

McQuarrie, N., Stock, J. M., Verdel, C., Wernicke, B.P., 2003, Cenozoic evolution of Neotethys and implications for the causes of plate motions, Geophysical Research Letters, 30(20), 2036, doi:10.1029/2003gl017992.

Mirnejad, H., Lalonde, A.E., Obeid, M., Hassanzadeh, J., 2013, Geochemistry and petrogenesis of Mashhad granitoids: An insight into the geodynamic history of the Paleo-Tethys in northeast of Iran: Lithos, 170–171, 105–116.

Mohajjel, M., Fergusson, C.L., 2000, Dextral transpression in Late Cretaceous continental collision, Sanandaj–Sirjan Zone, western Iran. Journal of Structural Geology 22, 1125–1139.

Mohajjel, M., Fergusson, C.L., Sahandi, M.R., 2003, Cretaceous–Tertiary convergenc and continental collision, Sanandaj–Sirjan Zone, western Iran. Journal of Asian Earth Sciences 21, 397–412.

Molinaro, M., Leturmy, P., Guezou, J. C., Frizon De Lamotte, D., Eshraghi, S.A., 2005, The Structure And Kinematics Of The Southeastern Zagros Fold-Thrust Belt, Iran: From Thin-Skinned To Thick-Skinned Tectonics. Tectonics 24, Tc3007, Doi:10.1029/2004tc001633, 19 Pp.

Moore, G., Vennemann, R., Carmichael, I., 1998, An empirical model for the solubility of H2O in magmas to 3 kilobars. American Mineralogist, 83, 136-142.

Mountain, G.S., Prell, W.L., 1990, A Multiphase Plate Tectonic History of the Southeast Continental Margin of Oman. In A.H.F. Robertson, M.P. Searle and A.C. Ries (Eds.), The Geology and Tectonics of the Oman Region. Geological Society London Special Publication, 49, 725-743.

Müller, A., van den Kerkhof, A. M., Behr, H. J., Kronz, A., & Koch-Müller, M., 2009, The evolution of late-Hercynian granites and rhyolites documented by quartz–a review. Earth and Environmental Science Transactions of the Royal Society of Edinburgh, 100(1-2), 185-204.

Müntener, O., Ulmer, P., 2006, Experimentally derived high-pressure cumulates from hydrous arc magmas and consequences for the seismic velocity structure of lower arc crust. Geophysical Research Letters 33 (21), L21308.

Murphy, M.D., Sparks, R.S.J., Barclay, J., Carroll, M.R., Brewer, T.S., 2000, Remobilization of andesite magma by intrusion of mafic magma at the Soufriere Hills Volcano, Montserrat, West Indies. Journal of Petrology 41 (1), 21–42.

Musson, R.M.W., 2009, Subduction in the western Makran: the historian's contribution, Journal of Geological Society of London, 166, 387-391.

Nakagawa, M., Wada, K., & Wood, C. P., 2002, Mixed magmas, mush chambers and eruption triggers: evidence from zoned clinopyroxene phenocrysts in andesitic scoria from the 1995 eruptions of Ruapehu volcano, New Zealand. Journal of petrology, 43(12), 2279-2303.

Natalin, B.A., Şengör, A.M., 2005, Late Palaeozoic to Triassic evolution of the Turan and Scythian platforms: the pre-history of the Palaeo-Tethyan closure. Tectonophysics 404, 175–202.

Nezafati, N., 2006, Au-Sn-W-Cu-Mineralization in the Astaneh-Sarband Area, West Central Iran, including a comparison of the ores with ancient bronze artifacts from Western Asia. PhD thesis, University of Tb0069006e00670065n, http://tobias-lib.ub.uni-tuebingen.de/volltexte/2006/2533/.

Nicholson, K.N., Khan, M., and Mahmood, K., 2010, Geochemistry of the Chagai-Raskoh arc, Pakistan: Complex arc dynamics spanning the Cretaceous to the Quaternary: Lithos, 118, 338–348.

Omrani, J., Agard, P., Whitechurch, H., Benoit, M., Prouteau, G., Jolivet, L., 2008, Arcmagmatism and subduction history beneath the Zagros Mountains, Iran: a new report of adakites and geodynamic consequences. Lithos 106, 380–398.

Pang, K.N., Chung, S.L., Zarrinkoub, M.H., Mohammadi, S.S., Yang, H.M., Chu, C.H., Lee, H.Y., Lo, C.H., 2012, Age, geochemical characteristics and petrogenesis of Late Cenozoic intraplate alkali basalts in the Lut–Sistan region, eastern Iran. Chemical Geology, 306–307, 40–53.

Pang, K., Chung, S., Zarrinkoub, M., Chiu, H., Li, X., 2014, On the magmatic record of the Makran arc, southeastern Iran: Insights from zircon U-Pb geochronology and bulk-rock geochemistry. Geochemistry, Geophysics, Geosystems, 15, doi:10.1002/2014GC005262.

Paul, A., Hatzfeld, D., Kaviani, A., Tatar, M., Pequegnat, C., 2010, Seismic Imaging Of The Lithospheric Structure Of The Zagros Mountain Belt (Iran). In Tectonic And Stratigraphic Evolution Of Zagros And Makran During The Mesozoic–Cenozoic (Eds P. Leturmy & C. Robin), Pp. 5–18. Geological Society Of London, Special Publication No. 330.

Peccerillo A., Taylor, S.R., 1976, Geochemistry of Eocene calc-alkaline volcanic rocks of the Kastamonu area, northern Turkey. Contribution Mineralogy and Petrology, 58, 63 81.

Perello, J., Razique, A., Schloderer, J., and Asad-ur-Rehman, 2008, The Chagai Porphyry Copper Belt, Baluchistan Province, Pakistan Economic Geology, 103, 1583-1612.

Philip, H., Cisternas, A., Gvishiani, A., Gorshkov, A.,1989, The Caucasus: An Actual Example Of The Initial Stages Of Continental Collision. Tectonophysics, 161, 1–21.

Ramezani, J., Tucker, R.D., 2003, The Saghand region, central Iran: U-Pb geochronology, petrogenesis and implications for Gondwana tectonics, American Journal of Science, 303, 622–665, doi:10.2475/ajs.303.7.622.

Ravaut, P., Bayer, R., Hassani, R., Rousset, D., Al Yahya'ey, A., 1997, Structure and evolution of the northern Oman margin: gravity and seismic constraints over the Zagros-Makran-Oman collision zone, Tectonophysics, 279, 253-280.

Regard, V., Bellier, O., Thomas, J.C., Abbassi, M., Mercier, J.L., Shabanian, E., Feghhi, Kh., Soleymaani], Sh., 2004, The accommodation of the Arabia-Asia convergence in the Zagros-Makran transfer zone, SE Iran: a transition between collision and subduction through a young deforming system, Tectonics, 23, TC4007, doi:10.1029/2003TC001599.

Rhodes, J.M. and Vollinger, M.J., 2005, Ferric/ferrous ratios in 1984 Mauna Loa lavas: acontribution to understanding the oxidation state of Hawaiian magmas: Contributions to Mineralogy and Petrology, 149, 666–674.

Richards, J.P., 2003a. Tectono-magmatic precursors for porphyry Cu–(Mo–Au) deposit formation. Economic Geology 98, 1515–1533.

Richards, J.P., 2003b, Metallogeny of the Neo-Tethys arc in central Iran, in Eliopoulos et al., eds., Mineral exploration and sustainable development: 7th Biennial SGA Meeting, Athens, August 24–28, 2003, Rotterdam, Millpress, p. 1237–1239.

Richards, J.P., 2011, High Sr/Y arc magmas and porphyry Cu ± Mo ± Au deposits: just add water. Economic Geology 106, 1075–1081.

Richards, J. P., 2014, Tectonic, magmatic, and metallogenic evolution of the Tethyan orogen: From subduction to collision. Ore Geology Reviews.Richards, J.P., Ullrich, T., Kerrich, R., 2006a. The Late Miocene–Quaternary Antofalla volcanic complex, southern Puna, NW Argentina: protracted history, diverse petrology, and economic potential. Journal of Volcanology and Geothermal Research, 152, 197-239.

Richards, J.P., Wilkinson, D., and Ullrich, T., 2006b, Geology of the Sari Gunay epithermal gold deposit, northwest Iran: Economic Geology, 101, 1455–1496.

Richards, J.P., and Kerrich, R., 2007, Adakite-like rocks: Their diverse origins and questionable role in metallogenesis: Economic Geology, 102, 537–576.

Richards, J.P., Spell, T., Rameh, E., Razique, A., and Fletcher, T., 2012, High Sr/Y magmas reflect arc maturity, high magmatic water content, and porphyry Cu ± Mo ± Au potential: Examples from the Tethyan arcs of central and eastern Iran and western Pakistan: Economic Geology, 107, 295–332.

Richards, J.P., Jourdan, F., Creaser, R.A., Maldonado, G., and DuFrane, A., 2013, Geology, geochemistry, geochronology, and economic potential of Neogene volcanic rocks in the Laguna Pedernal and Salar de Aguas Calientes segments of the Archibarca lineament, northwest Argentina: Journal of Volcanology and geothermal research, 258, 47–73.

Ridolfi, F., Renzulli, A., 2012, Calcic amphiboles in calc-alkaline and alkaline magmas: thermobarometric and chemometric empirical equations valid up to 1,130°C and 2.2 GPa, Contribution Mineralogy Petrology, 163, 877–895.

Ridolfi, F., Renzulli, A., and Puerini, M., 2010, Stability and chemical equilibrium of amphibole in calc-alkaline magmas: An overview, new thermobarometric formulations and

application to subduction-related volcanoes: Contributions to Mineralogy and Petrology, 160, 45–66.

Riley, T. R., Leat, P. T., Pankhurst, R. J., & Harris, C., 2001, Origins of large volume rhyolitic volcanism in the Antarctic Peninsula and Patagonia by crustal melting. Journal of petrology, 42(6), 1043-1065.

Robertson, A.H.F., 2007, Overview of tectonic settings related to the rifting and opening of Mesozoic ocean basins in the Eastern Tethys: Oman, Himalayas and Eastern Mediterranean regions. In: Karner, G., Manatschal, G., Pinheiro, L. (Eds.), Geological Society, London Special Publication, 282, 325–389.

Rowe, M. C., Kent, A. J., & Nielsen, R. L., 2009, Subduction influence on oxygen fugacity and trace and volatile elements in basalts across the Cascade Volcanic Arc. Journal of Petrology, 50(1), 61-91.

Rutherford, M.J., 2008, Magma ascent rates. Reviews in Mineralogy and Geochemistry 69 (1), 241–271.

Rutherford, M. J., & Devine, J. D., 2003, Magmatic conditions and magma ascent as indicated by hornblende phase equilibria and reactions in the 1995–2002 Soufriere Hills magma. Journal of Petrology, 44(8), 1433-1453.

Rutherford, M.J., Hill, P.M., 1993, Magma ascent rates from amphibole breakdown.an experimental study applied to the 1980-1986 Mount St Helens eruptions. Journal of Geophysical Research Solid Earth, 98, 19667-19685.

Saccani, E., Allahyari, K., Beccaluva, L., Bianchini, G., 2012, Geochemistry and petrology of the Kermanshah ophiolites (Iran): implication for the interaction between passive rifting, oceanic accretion, and plume-components in the Southern Neo-Tethys Ocean. Gondwana Research. http://dx.doi.org/10.1016/j.gr.2012.10.009.

Sakuyama, M.,1978, Petrographic evidence of magma mixing in Shirouma-Oike volcano, Japan. Bulletin Volcanologique, 41(4), 501-512.

Schmidt, M.W., 1992, Amphibole composition in tonalite as a function of pressure: an experimental calibration of the Al-in-hornblende barometer, Contribution in mineralogy and petrology, 110, 304-310.

Sdrolias M., Müller, R., 2006, Controls on back-arc basin formation, Geochemistry, Geophysics, Geosystems, 7(4), Q04016, doi:10.1029/2005GC001090.

Sengör, A.M.C., 1987, Tectonics of the Tethysides: Orogenic Collage Development in a Collisional Setting: Annual Review of Earth and Planetary Sciences, 15, 213–244.

Sengör, A.M.C., Natalin, BA., 1996, Turkic type orogeny and its role in the making of the continental crust, Annual review of earth and planetary sciences, 24, 263-337.

Shad Manaman, N., Shomali, Z., Mirzaei, N., 2010, 3-D S-velocity structure of upper mantle and Moho depth variations in the Makran subduction zone, Earth and space physic, 37(2), 153-169 (In Farsi with Abstract in English).

Shafaii Moghadam, H., Stern, R.J., Rahgoshay M., 2010a, The Dehshir Ophiolite (Central Iran): Geochemical Constraints On The Origin And Evolution Of The Inner Zagros Ophiolitic Belt. Geological Society Of America Bulletin 122, 1516–47.

Shafaii Moghadam, H., Whitechurch, H., Rahgoshay, M., Monsef, I., 2010b, Significance of Nain-Baft ophiolitic belt (Iran): Short-lived, transtensional Cretaceous back-arc oceanic basins over the Tethyan subduction zone - Comptes Rendus Geoscience, 49, 261-270.

Shafaii Moghadam, H., Stern, R. J., Chiaradia, M., Rahgoshay, M., 2013, Geochemistry and tectonic evolution of the Late Cretaceous Gogher–Baft ophiolite, central Iran, 168, 33-47.

Shafiei, B., Haschke, M., Shahabpour, J., 2009, Recycling of orogenic arc crust triggers porphyry Cu mineralization in Kerman Cenozoic arc rocks, southeastern Iran: Mineralium Deposita, 44, 265–283.

Shahabpour, J., 2005, Tectonic evolution of the orogenic belt located between Kerman and Neyriz. Journal of Asian Earth Sciences 24, 405–417.

Shahabpour, J., 2010, Tectonic implications of the geochemical data from the Makran igneous rocks in Iran, Islan Arc, 19, 676-689.

Shakeri, A., Moore, F., Kompani-Zare, M., 2008, Geochemistry Of The Thermal Springs Of Mount Taftan, Southeastern Iran, Journal Of Volcanology And Geothermal Research, 178, 829-836.

Shaw, J. E., Baker, J. A., Menzies, M. A., Thirlwall, M. F., & Ibrahim, K. M., 2003, Petrogenesis of the largest intraplate volcanic field on the Arabian Plate (Jordan): a mixed lithosphere–asthenosphere source activated by lithospheric extension. Journal of Petrology, 44(9), 1657-1679.

Siddiqui, R.H., 2004, Crustal evolution of Chagai-Raskoh arc terrane, Balochistan, Pakistan: Unpublished Ph.D. thesis, University of Peshawar, 353 p.

Siddiqui, R.H., AsifKhan, M., and Qasim Jan, M., 2007, Geochemistry and petrogenesis of the Miocene alkaline and sub-alkaline volcanic rocks from the Chagai Arc, Baluchistan, Pakistan: Implications for porphyry Cu-Mo-Au deposits, Journal of Himalayan Earth Sciences, 40, 1-23.

Siddiqui, R.H., Khan, M.A., Brohi, I.A, 2010, Paleocene Tholeiitic volcanism and oceanic island arc affinities of the Chagai Arc, balochestan, Pakistan, Sind University research Journal, 42(2), 83-98.

Siebert, L., Simkin, T., 2002, Volcanoes Of The World: An Illustrated Catalog Of Holocene Volcanoes And Their Eruptions. Smithsonian Institution, Global Volcanism Program Digital Information Series, Gvp-3. Http://Www.Volcano.Si. Edu/World/

Sillitoe, R.H., 1972. A plate tectonic model for the origin of porphyry copper deposits Economic Geology 67, 184–197.

Sillitoe, R.H., 2010. Porphyry copper systems. Economic Geology 105, 3–41.

Stampfli, G.M., 2000, Tethyan ocean. In: Bozkurt, E., Winchester, J.A., Piper, J.D.A. (Eds.), Tectonic and magmatism in Turkey and surrounding area. Special Publication, vol. 173. Geological Society, London,1–23.

Smith, A.L., Roobol, M.J., Mattioli, G.S., Fryxell, J.E., Daly, G.E. and Fernandez, L.A., 2013. The volcanic geology of the mid-arc island of Dominica, Lesser Antilles: the surface expression of an island-arc batholith. Special Paper 496. Geological Society of America: Colorado. pp 248.

Stöcklin, J., 1968, Structural history and tectonics of Iran: a review. American Association of Petroleum Geologists Bulletin 52, 1229–1258.

Stöcklin, J., 1974, Possible Ancient Continental Margins in Iran, in Burk, C. A., and Drake, C. L., editors, The Geology of Continental Margins: New York, Springer Verlag, 873–887.

Stoneley, R., 1981, The geology of the Kuh-e Dalneshin area of southern Iran, and its bearing on the evolution of southern Tethys: Journal of the Geological Society, London, 138, p. 509–526.

Sun, S.S., McDonough, W.F., 1989, Chemical and isotopic systematics of oceanic basalts: implications for mantle composition and processes. In: Saunders, A.D., Norry, M.J. (Eds.), Magmatism in the Ocean Basins, vol. 42. Geological Society of London, Special Publication, 313–345.

Tepley, F. J., Davidson, J. P., & Clynne, M. A., 1999, Magmatic interactions as recorded in plagioclase phenocrysts of Chaos Crags, Lassen Volcanic Center, California. Journal of Petrology, 40(5), 787-806.

Tindle, A.G., Webb, P.C., 1994, PROB-AMPH- a spreadsheet program to classify microprobe-derived amphibole analyses, Computer and Geoscience, 20(7-8), 1201-1228.

Torabi, G., 2011, Middle Eocene Volcanic Shoshonites from Western Margin of Central-East Iranian Microcontinent (CEIM), a Mark of Previously Subducted CEIM-Confining Oceanic Crust, Petrology, 19(7), 675–689.

Trumbull, R.B., Wittenbrink, R., Hahne, K., Emmermann, R., Büsch, W., Gerstenberger, H., Siebel, W., 1999, Evidence for Late Miocene to Recent contamination of arc andesites by crustal melts in the Chilean Andes (25–26°S) and its geodynamic implications. Journal of South American Earth Sciences 12, 135–155.

Verdel, C., Wernicke, B.P., Hassanzadeh, J., Guest, B., 2011, A Paleogene extensional arc flare-up in Iran. Tectonics 30, TC3008 http://dx.doi.org/10.1029/2010TC002809.

Vernant, P., Nilforoushan, F., Chery, J., Bayer, R., Djamour, Y., Masson, F., Nankali, H., Ritz, J.F., Sedighi, M., Tavakoli, F., 2004, Deciphering oblique shortening of Central Alborz in Iran using geodetic data. Earth and Planet Science Letter, 223, 177-85.

Waight, T.E., Weaver,S.D., Muir, R.J., 1998, The Hohonu batholith the north Westland, New Zealand: granitoid compositions controlled by source H2O contents and generated during tectonic transition. Contribution Mineralogy Petrology, 130, 225–239.

Walker, R.T., 2003, Active faulting and tectonics of eastern Iran. Cambridge University.

Walker, R.T., Jackson, J., 2004, Active tectonics and Late Cenozoic strain distribution in central and eastern Iran. Tectonics, 23, 5010-5034.

Wellman, H.W., 1966, Active wrench faults of Iran, Afghanistan, and Pakistan, Geologische Rundschau, 55(3), 716-735.

Wiebe, R., Manon, M., Hawkins, D. and McDonough, W., 2004. Late-stage mafic injection and thermal rejuvenation of the Vinalhaven granite, Coastal Maine. J. Petrol., 45(11): 2133-2153.

Winter, J. D. ,2014, *Principles of igneous and metamorphic petrology*. Pearson.

Withmarsh, R.B., 1979, The Owen Basin off the south-east margin of Arabia and the evolution of the Owen Fracture Zone, Geophysical Journal of the Royal Astronomical Society, 58(2), 441–470.

Workman, R. K., & Hart, S. R., 2005, Major and trace element composition of the depleted MORB mantle (DMM). Earth and Planetary Science Letters,231(1), 53-72.

Yeganehfar, H., Ghorbani, M., Shinjo, R., Ghaderi., M., 2013, Magmatic and geodynamic evolution of Urumieh–Dokhtar basic volcanism, Central Iran: major, trace element, isotopic, and geochronologic implications, International Geology Review, 55(6), 767-786.

Yilmaz, Y., 1993, New evidence and model on the evolution of the southeast Anatolian orogen, GSA Bulletin, 105, 251–271.

Zen, E.A., 1989, Aluminum enrichment in silicate melts by fractional crystallization: some mineralogical and petrographical constraints. Journal of Petrology, 27, 1095–1118.

Appendices

Appendix A: Samples locations.

Sample Name	Coordinate		Elevation
	Easting	Northing	m
12AR011	299034	3176349	2192
12AR013	298947	3173637	2374
12AR014	298952	3173581	2395
12AR017	298952	3173581	2395
13AR003	319906	3174058	2086
13AR004	319626	3173645	2088
13AR005	319626	3173645	2291
13AR006	317140	3174993	2182
13AR007	312332	3172523	2294
13AR008	310624	3170173	2709
13AR010	327622	3160746	1920
13AR011	322249	3161730	2294
13AR012	322111	3161698	2302
13AR013	323321	3161213	2215
13AR014	323433	3162654	2256
13AR015	323184	3162897	2346
13AR016	331667	3164814	1783
13AR017	328108	3164668	1935
13AR018	327322	3165145	1974
13AR019	324592	3165390	2146
13AR021	316049	3156033	2117
13AR023	314668	3156773	2193
13AR024	314697	3156855	2194

Appendix B: Nevada Isotope Geochronology Laboratory - Description and Procedures

Samples analyzed by the $^{40}Ar/^{39}Ar$ method at the University of Nevada Las Vegas were wrapped in Al foil and stacked in 6 mm inside diameter sealed fused silica tubes. Individual packets averaged 3 mm thick and neutron fluence monitors (FC-2, Fish Canyon Tuff sanidine) were placed every 5-10 mm along the tube. Synthetic K-glass and optical grade CaF_2 were included in the irradiation packages to monitor neutron induced argon interferences from K and Ca. Loaded tubes were packed in an Al container for irradiation. Samples irradiated at the U. S. Geological Survey TRIGA Reactor, Denver, CO were in-core for 7 hours in the In-Core Irradiation Tube (ICIT) of the 1 MW TRIGA type reactor. Correction factors for interfering neutron reactions on K and Ca were determined by repeated analysis of K-glass and CaF_2 fragments. Measured $(^{40}Ar/^{39}Ar)_K$ values were 1.31 (± 89.31%) x 10^{-2}. Ca correction factors were $(^{36}Ar/^{37}Ar)_{Ca}$ = 2.47 (± 4.93%) x 10^{-4} and $(^{39}Ar/^{37}Ar)_{Ca}$ = 7.13 (± 9.64%) x 10^{-4}. J factors were determined by fusion of 4-8 individual crystals of neutron fluence monitors which gave reproducibility's of 0.30% to 0.96% at each standard position. Variation in neutron fluence along the 100 mm length of the irradiation tubes was <4%. Matlab curve fit was used to determine J and uncertainty in J at each standard position. No significant neutron fluence gradients were present within individual packets of crystals as indicated by the excellent reproducibility of the single crystal fluence monitor fusions.

Irradiated FC-2 sanidine standards together with CaF_2 and K-glass fragments were placed in a Cu sample tray in a high vacuum extraction line and were fused using a 20 W CO_2 laser. Sample viewing during laser fusion was by a video camera system and positioning was via a motorized sample stage. Samples analyzed by the furnace step heating method utilized a double vacuum resistance furnace similar to the Staudacher et al. (1978) design. Reactive gases were removed by three GP-50 SAES getters prior to being admitted to a MAP 215-50 mass spectrometer by expansion. The relative volumes of the extraction line and mass spectrometer allow 80% of the gas to be admitted to the mass spectrometer for laser fusion analyses and 76% for furnace heating analyses. Peak intensities were measured using a Balzers electron multiplier by peak hopping through 7 cycles; initial peak heights were determined by linear regression to the time of gas admission. Mass spectrometer discrimination and sensitivity was monitored by repeated analysis of atmospheric argon aliquots from an on-line pipette system. Measured $^{40}Ar/^{36}Ar$ ratios were 275.62 ± 0.26 % during this work, thus a discrimination correction of 1.0721 (4 AMU) was applied to measured isotope ratios. The sensitivity of the mass spectrometer was ~6 x 10^{-17} mol mV^{-1} with the multiplier operated at a gain of 36 over the Faraday. Line blanks averaged 2.96 mV for mass 40 and 0.02 mV for mass 36 for laser fusion analyses and 18.38 mV for mass 40 and 0.07 mV for mass 36 for furnace heating analyses. Discrimination, sensitivity, and blanks were relatively constant over the period of data collection. Computer automated operation of the sample stage, laser, extraction line and mass spectrometer as well as final data reduction and age calculations were done using LabSPEC software written by B. Idleman (Lehigh University). An age of 28.02 Ma (Renne et al., 1998) was used for the Fish Canyon Tuff sanidine fluence monitor in calculating ages for samples.

For $^{40}Ar/^{39}Ar$ analyses a plateau segment consists of 3 or more contiguous gas fractions having analytically indistinguishable ages (i.e. all plateau steps overlap in age at ±

2σ analytical error) and comprising a significant portion of the total gas released (typically >50%). Total gas (integrated) ages are calculated by weighting by the amount of ^{39}Ar released, whereas plateau ages are weighted by the inverse of the variance. For each sample inverse isochron diagrams are examined to check for the effects of excess argon. Reliable isochrons are based on the MSWD criteria of Wendt and Carl (1991) and, as for plateaus, must comprise contiguous steps and a significant fraction of the total gas released. All analytical data are reported at the confidence level of 1σ (standard deviation).

References:

Renne, P.R., Swisher, C.C, Deino, A.L., Karner, D.B., Owens, T.L., DePaolo, D.J., 1998, Intercalibration of standards, absolute ages and uncertainties in $^{40}Ar/^{39}Ar$ dating, *Chemical Geology*, v. 145, p. 117-152.

Staudacher, T.H., Jessberger, E.K., Dorflinger, D., and Kiko, J., A refined ultrahigh-vacuum furnace for rare gas analysis, *J. Phys. E: Sci. Instrum*., *11*, 781-784, 1978.

Wendt, I., and Carl, C., 1991, The statistical distribution of the mean squared weighted deviation, *Chemical Geology*, v. 86, p. 275-285.

Appendix C: $^{40}Ar/^{39}Ar$ analyses:

12AR10, Alunite, 9.18 mg, J = 0.001744 ± 0.007%														
step	T (C)	t (min.)	^{36}Ar	^{37}Ar	^{38}Ar	^{39}Ar	^{40}Ar	$\%^{40}Ar$ *	$\%^{39}Ar$ rlsd	Ca/K	$^{40}Ar^*/^{39}Ar$ K	Age (Ma)	1s.d.
1	350	12	4.143	0.079	0.982	14.805	1131.57	1.5	1.3	0.052237129	1.159671	3.65	5.68
2	375	12	1.897	0.072	0.609	18.932	569.493	10.6	1.6	0.037230147	3.181718	9.98	2.27
3	400	12	3.654	0.192	1.322	48.693	1089.63	9.9	4.1	0.038600561	2.241275	7.04	1.67
4	425	12	2.390	0.210	1.934	112.305	772.682	16.9	9.5	0.018305289	1.176232	3.70	0.52
5	450	12	0.498	0.070	0.502	31.804	173.340	24.4	2.7	0.021546319	1.241843	3.90	0.38
6	475	12	0.828	0.090	0.519	26.997	272.938	19.2	2.3	0.032635118	1.880195	5.91	0.73
7	500	12	2.518	0.248	1.648	93.987	872.844	22.7	8.0	0.025831	2.128652	6.69	0.70
8	525	12	3.755	0.553	4.187	263.533	1514.69	33.5	22.3	0.020542193	1.962152	6.16	0.44
9	560	12	3.461	1.115	7.374	510.645	1872.33	50.4	43.2	0.021375317	1.889443	5.94	0.29
10	600	12	0.773	0.664	0.706	42.037	290.187	29.7	3.6	0.15463569	1.993726	6.26	0.50
11	650	12	0.230	1.130	0.089	3.193	71.701	17.0	0.3	3.467889721	3.031207	9.51	1.35
12	1000	12	0.536	0.794	0.182	13.935	154.845	7.2	1.2	0.55787527	0.741665	2.33	0.75

	Cumulative $\%^{39}Ar$ rlsd =100.0	Total gas age = 5.84	0.32
note: isotope beams in mV, rlsd = released, error in age includes J error, all errors 1 sigma		Plateau age = 6.10	0.40
(^{36}Ar through ^{40}Ar are measured beam intensities, corrected for decay for the age calculations)		(steps 6-10)	
		Isochron age = 5.50 (steps 6-11)	0.29

12AR017, Biotite, 38.80 mg, J = 0.001658 ± 0.67%													
step	**T (C)**	**t (min.)**	**^{36}Ar**	**^{37}Ar**	**^{38}Ar**	**^{39}Ar**	**^{40}Ar**	**%^{40}Ar***	**% ^{39}Ar rlsd**	**Ca/K**	**^{40}Ar*/^{39}Ar K**	**Age (Ma)**	**1s.d.**
1	860	12	3.829	17.154	2.635	78.322	1278.18	18.7	2.6	6.206734602	3.083922	9.20	0.15
2	940	12	1.208	9.651	8.913	197.438	852.980	62.2	6.6	1.383166529	2.710374	8.09	0.08
3	990	12	0.426	1.061	14.973	315.338	942.368	88.1	10.6	0.09516968	2.650265	7.91	0.07
4	1040	12	0.463	1.046	19.406	410.525	1197.95	89.7	13.8	0.072069	2.640191	7.88	0.08
5	1090	12	0.567	1.023	15.809	333.159	1017.83	85.1	11.2	0.086852535	2.619373	7.82	0.07
6	1130	12	0.633	1.209	13.497	282.100	901.816	81.7	9.5	0.121223343	2.611986	7.80	0.07
7	1170	12	0.908	2.150	19.682	393.577	1284.99	81.2	13.2	0.154517002	2.664368	7.95	0.07
8	1200	12	0.796	3.192	25.158	465.863	1415.90	85.2	15.6	0.193810578	2.603592	7.77	0.07
9	1230	12	0.363	2.500	17.970	316.946	911.093	90.3	10.6	0.223116399	2.595534	7.75	0.07
10	1260	12	0.161	0.630	5.433	101.820	303.052	89.5	3.4	0.175015994	2.577739	7.69	0.07
11	1290	12	0.116	0.218	2.195	41.805	137.192	85.8	1.4	0.147500959	2.558266	7.64	0.07
12	1320	12	0.127	0.157	2.098	40.711	137.865	83.4	1.4	0.109081045	2.566995	7.66	0.07
13	1400	12	0.100	0.040	0.250	4.361	40.310	50.7	0.1	0.259451123	3.053680	9.11	0.32
								Cumulative %^{39}Ar rlsd=100.0			Total gas age =7.88		0.03
note: isotope beams in mV, rlsd = released, error in age includes J error, all errors 1 sigma											Plateau age =7.87		0.07
(^{36}Ar through ^{40}Ar are measured beam intensities, corrected for decay for the age calculations)											(steps 3-7)		

13AR006, Biotite, 32.48 mg, J = 0.001711 ± 0.06%													
step	**T (C)**	**t (min.)**	**^{36}Ar**	**^{37}Ar**	**^{38}Ar**	**^{39}Ar**	**^{40}Ar**	**%^{40}Ar***	**% ^{39}Ar rlsd**	**Ca/K**	**^{40}Ar*/^{39}Ar K**	**Age (Ma)**	**1s.d.**
1	650	12	0.633	0.050	0.246	3.217	184.016	6.0	0.1	0.414647372	3.394907	10.45	0.47
2	725	12	2.807	0.156	1.451	20.359	857.799	10.0	0.8	0.204408913	4.249566	13.07	0.39
3	790	12	1.212	0.225	1.546	29.156	369.971	10.0	1.1	0.205866862	1.259626	3.88	0.11
4	850	12	0.865	0.284	2.135	42.201	279.479	15.1	1.6	0.17952458	0.991518	3.06	0.09
5	905	12	0.976	0.361	6.836	137.852	407.783	34.4	5.1	0.069856639	1.015208	3.13	0.04
6	960	12	1.176	0.533	20.776	422.898	764.285	57.7	15.8	0.033620197	1.047012	3.23	0.04
7	1015	12	1.371	0.607	28.463	581.278	967.318	60.8	21.7	0.027855612	1.019102	3.14	0.04
8	1055	12	0.968	0.687	20.376	416.757	687.954	61.4	15.5	0.043972778	1.016506	3.14	0.04
9	1095	12	0.528	1.478	11.246	217.449	356.664	60.5	8.1	0.181319947	0.982107	3.03	0.04
10	1125	12	0.350	2.880	7.976	136.850	230.153	61.0	5.1	0.561471122	1.002227	3.09	0.04
11	1155	12	0.323	1.874	8.074	148.896	234.567	66.1	5.5	0.335765377	0.993465	3.06	0.04
12	1200	12	0.471	2.826	17.753	322.039	452.813	73.4	12.0	0.234098891	1.014559	3.13	0.04
13	1400	12	0.343	3.520	12.071	205.110	299.693	83.0	7.6	0.457848313	1.010015	3.12	0.04
								Cumulative %39Ar rlsd =100.0			Total gas age =3.23		0.03
			note: isotope beams in mV, rlsd = released, error in age includes J error, all errors 1 sigma								Plateau age =3.10		0.03
			(36Ar through 40Ar are measured beam intensities, corrected for decay for the age calculations)								(steps 7-13)		
											No isochron		

13AR008, Biotite, 11.58 mg, J = 0.001735 ± 0.06%													
step	**T (C)**	**t (min.)**	**^{36}Ar**	**^{37}Ar**	**^{38}Ar**	**^{39}Ar**	**^{40}Ar**	**%^{40}Ar***	**% ^{39}Ar rlsd**	**Ca/K**	**^{40}Ar*/^{39}Ar K**	**Age (Ma)**	**1s.d.**
1	900	12	0.992	0.322	0.625	17.659	285.73	5.2	1.9	0.611562362	0.830290	2.60	0.39
2	970	12	0.115	0.107	0.670	13.327	45.743	40.7	1.4	0.269250355	1.153202	3.61	0.11
3	1040	12	0.129	0.149	1.547	28.799	58.660	48.0	3.1	0.173500558	0.848527	2.65	0.07
4	1090	12	0.178	0.163	2.636	53.529	96.075	54.5	5.7	0.102112963	0.905801	2.83	0.06
5	1130	12	0.301	0.176	4.673	99.397	167.997	53.5	10.5	0.059376698	0.872204	2.73	0.06
6	1160	12	0.386	0.221	5.673	119.024	205.618	51.1	12.6	0.062263678	0.848847	2.66	0.06
7	1180	12	0.311	0.238	4.663	95.347	166.524	52.3	10.1	0.083704701	0.865805	2.71	0.06
8	1200	12	0.238	0.317	5.117	104.311	154.106	62.2	11.1	0.101908763	0.865485	2.71	0.05
9	1220	12	0.327	0.414	11.652	246.631	293.616	71.6	26.2	0.056289697	0.833490	2.61	0.05
10	1240	12	0.242	0.133	6.989	151.917	193.840	69.4	16.1	0.029357419	0.847567	2.65	0.05
11	1260	12	0.075	0.031	0.477	9.855	29.162	53.3	1.0	0.105484324	0.981963	3.07	0.11
12	1280	12	0.049	0.010	0.060	0.912	15.780	75.3	0.1	0.367725141	3.766799	11.75	1.26
13	1400	12	0.105	0.013	0.097	1.712	29.639	3.6	0.2	0.254649326	0.254044	0.80	0.79
								Cumulative %39Ar rlsd =100.0			Total gas age =2.69		0.04
			note: isotope beams in mV, rlsd = released, error in age includes J error, all errors 1 sigma								Plateau age =2.67		0.04
			(36Ar through 40Ar are measured beam intensities, corrected for decay for the age calculations)								(steps 5-10)		

13AR016, Biotite, 42.98 mg, J = 0.001645 ± 0.75%													
step	**T (C)**	**t (min.)**	**^{36}Ar**	**^{37}Ar**	**^{38}Ar**	**^{39}Ar**	**^{40}Ar**	**%^{40}Ar***	**% ^{39}Ar rlsd**	**Ca/K**	**^{40}Ar*/^{39}Ar K**	**Age (Ma)**	**1s.d.**
1	860	12	4.868	1.230	2.719	54.771	1423.03	5.8	1.5	0.622619232	1.520579	4.51	0.22
2	940	12	1.707	0.506	7.037	138.266	533.381	11.8	3.7	0.101445561	0.456416	1.35	0.05
3	990	12	0.819	0.422	12.914	243.801	310.113	27.3	6.5	0.047980824	0.342448	1.02	0.04
4	1040	12	0.693	0.433	15.740	297.119	285.007	33.0	7.9	0.04039682	0.311768	0.93	0.04
5	1090	12	0.989	0.564	22.955	432.477	419.125	34.6	11.5	0.036149744	0.333682	0.99	0.04
6	1130	12	1.129	1.598	21.904	393.718	427.910	27.1	10.4	0.112509948	0.293226	0.87	0.04
7	1170	12	1.717	2.816	31.934	568.495	680.57	30.4	15.1	0.137312085	0.362340	1.08	0.04
8	1200	12	1.678	1.595	42.327	769.189	718.79	35.2	20.4	0.057480381	0.327614	0.97	0.04
9	1230	12	1.009	2.072	39.590	710.018	516.03	46.0	18.8	0.08089386	0.330311	0.98	0.04
10	1260	12	0.208	0.515	8.119	144.903	104.99	51.5	3.8	0.098520678	0.326602	0.97	0.04
11	1290	12	0.097	0.083	0.827	14.119	30.038	22.9	0.4	0.162959757	0.255470	0.76	0.09
12	1320	12	0.088	0.021	0.185	3.031	23.737	-2.0	0.1	0.192062903	-0.060650	-0.18	-0.40
13	1400	12	0.129	0.031	0.362	6.318	37.771	10.8	0.2	0.136014327	0.405499	1.20	0.11
								Cumulative %39Ar rlsd =100.0			Total gas age =1.04		0.03
			note: isotope beams in mV, rlsd = released, error in age includes J error, all errors 1 sigma								Plateau age =1.00		0.04
			(36Ar through 40Ar are measured beam intensities, corrected for decay for the age calculations)								(steps 7-10)		
											No isochron		

13AR017, Amphibole, 43.50 mg, J = 0.001727 ± 0.05%													
step	**T (C)**	**t (min.)**	**^{36}Ar**	**^{37}Ar**	**^{38}Ar**	**^{39}Ar**	**^{40}Ar**	**%^{40}Ar***	**% ^{39}Ar rlsd**	**Ca/K**	**^{40}Ar*/^{39}Ar K**	**Age (Ma)**	**1s.d.**
1	950	12	6.883	1.512	3.199	44.821	2007.11	4.3	14.4	1.423525897	16543.35526	6110.00	1259.00
2	1090	12	1.758	2.116	2.361	6.800	502.990	3.1	2.2	13.17895423	30698.84628	7197.00	2216.00
3	1130	12	0.479	8.783	7.368	21.305	128.725	5.9	6.8	17.48285042	454.364681	1045.00	184.00
4	1140	12	0.260	9.290	7.471	21.588	61.196	2.6	6.9	18.25397484	59.690406	177.00	118.00
5	1150	12	0.349	19.547	15.798	47.328	82.702	16.1	15.2	17.51528472	294.109823	741.00	113.00
6	1160	12	0.275	18.310	14.970	46.727	57.353	11.0	15.0	16.61326086	113.530556	323.00	104.00
7	1170	12	0.109	5.671	4.843	15.004	24.385	18.5	4.8	16.0216701	144.130809	401.00	94.00
8	1180	12	0.084	2.313	1.829	5.195	19.954	2.5	1.7	18.88988646	29.281886	89.00	143.00
9	1190	12	0.095	3.183	2.710	6.946	22.990	13.9	2.2	19.44533661	212.951374	565.00	169.00
10	1230	12	0.465	34.799	31.660	81.571	100.600	18.9	26.1	18.09521998	243.829106	634.00	100.00
11	1400	12	0.166	6.600	5.378	15.007	38.625	5.1	4.8	18.65770584	59.336456	176.00	122.00
								Cumulative %^{39}Ar rlsd=100.0			Total gas age =1485.17		79.23
	note: isotope beams in mV, rlsd = released, error in age includes J error, all errors 1 sigma										No plateau		
	(36Ar through 40Ar are measured beam intensities, corrected for decay for the age calculations)										No isochron		